Purdue University
Purdue e-Pubs

Open Access Dissertations | Theses and Dissertations

4-2016

Improving the mechanistic study of neuromuscular diseases through the development of a fully wireless and implantable recording device

Rebecca A. Bercich
Purdue University

Follow this and additional works at: https://docs.lib.purdue.edu/open_access_dissertations

 Part of the Biomedical Engineering and Bioengineering Commons

Recommended Citation

Bercich, Rebecca A., "Improving the mechanistic study of neuromuscular diseases through the development of a fully wireless and implantable recording device" (2016). *Open Access Dissertations*. 621.
https://docs.lib.purdue.edu/open_access_dissertations/621

This document has been made available through Purdue e-Pubs, a service of the Purdue University Libraries. Please contact epubs@purdue.edu for additional information.

PURDUE UNIVERSITY
GRADUATE SCHOOL
Thesis/Dissertation Acceptance

This is to certify that the thesis/dissertation prepared

By Rebecca A. Bercich

Entitled

IMPROVING THE MECHANISTIC STUDY OF NEUROMUSCULAR DISEASES THROUGH THE DEVELOPMENT OF A FULLY WIRELESS AND IMPLANTABLE RECORDING DEVICE

For the degree of Doctor of Philosophy

Is approved by the final examining committee:

Pedro P. Irazoqui
Chair

Kevin L. Seburn

Bradley S. Duerstock

Eugenio Culurciello

To the best of my knowledge and as understood by the student in the Thesis/Dissertation Agreement, Publication Delay, and Certification Disclaimer (Graduate School Form 32), this thesis/dissertation adheres to the provisions of Purdue University's "Policy of Integrity in Research" and the use of copyright material.

Approved by Major Professor(s): Pedro P. Irazoqui

Approved by: George R. Wodicka 4/18/2016

Head of the Departmental Graduate Program Date

IMPROVING THE MECHANISTIC STUDY OF NEUROMUSCULAR DISEASES THROUGH THE DEVELOPMENT OF A FULLY WIRELESS AND IMPLANTABLE RECORDING DEVICE

A Dissertation

Submitted to the Faculty

of

Purdue University

by

Rebecca A. Bercich

In Partial Fulfillment of the

Requirements for the Degree

of

Doctor of Philosophy

May 2016

Purdue University

West Lafayette, Indiana

This work is dedicated to my family, whose love and support are given in unwavering abundance. Thank you to my grandmother, Barbara, and grandfather, Allen—the first engineer I ever met. Thank you to my father, Brian, and my siblings, Jesse and Carly. Finally, thank you to my mother, Anne, whose wisdom and kindness have guided me, shaped me, and challenged me.

Aussi, à Grégory: chaque jour tu m'étonnes à bien des égards. Je t'aime, mon cheri.

ACKNOWLEDGEMENTS

I owe a debt of gratitude to my mentors and teammates whose influences are interwoven into this work. Thank you to my research adviser, Dr. Pedro Irazoqui, for encouraging me to explore, question, and grow within the many enriching research and teaching opportunities you granted me. Thank you to Dr. Kevin Seburn for your insights into electrophysiology and animal research models, which were invaluable in steering the direction of this project. Also thank you to Dr. Bradley Duerstock and Dr. Eugenio Culurciello for lending your expertise and offering feedback to this body of work while serving on my committee.

I would also like to acknowledge the members of The Center for Bionic Medicine within the Rehabilitation Institute of Chicago, particularly Dr. Todd Kuiken, Dr. Levi Hargrove, and Dr. Lauren Hammer for their contributions to the development of the Myonode device for upper-limb prosthesis control. Thank you also to Dr. Robert Burgess, who not only fostered the collaboration with the Jackson Laboratory, but also took the time to help me understand the role of genomics in personalized medicine.

Finally, I must say thank you to my colleagues in the Center for Implantable Devices at Purdue University; it's been a privilege to work with these extraordinary people who have been profoundly instrumental in my training and professional

development. Thank you especially to Dr. Henry Mei, whose contributions in the area of wireless power transfer over the course of his doctoral work produced incredible and enabling technology that allowed me take my work further than it would have otherwise gone. Thank you to Dan Pederson and Zhi Wang for their efforts in firmware development and to Muhammad Arafat for his help developing circuit topologies. I would also like to recognize Dr. Matt Ward, Dr. Steven Lee, Hansraj Bhamra, Young Kim, Yu-Wen Huang, Jack Williams, Chris Quinkert, Kyle Thackston, Jesse Somann, Henry Zhang, Suzette Miller, Teegan Eckes, Yumin Gao, and Curtis Slaubaugh for their assistance and for the countless ways in which they've helped me grow. Lastly, a heartfelt thank you to my friend and colleague Gabriel Albors, who kept things grounded with his enviable pragmatism, and whom I always felt was looking out for me.

TABLE OF CONTENTS

Page

Page

LIST OF TABLES

Table Page

LIST OF FIGURES

Figure Page

Figure Page

Figure Page

Figure Page

Figure Page

Figure Page

Figure Page

Figure Page

Figure Page

Figure Page

LIST OF ABBREVIATIONS

ADC	Analog-to-digital converter
AFE	Analog front-end
ALS	Amyotrophic lateral sclerosis
ASIC	Application-specific integrated circuit
BER	Bit error rate
CMOS	Complementary metal-oxide-semiconductor
ECRL	Extensor carpi radialis longus
EEG	Electroencephalogram
EKG	Electrocardiogram
EMG	Electromyography
EMI	Electromagnetic interference
FCC	Federal Communications Commission
FEM	Finite element method
GUI	Graphical user interface
HFSS	High frequency structure simulator
IC	Integrated circuit
imEMG	Intramuscular electromyography

IPN	Inherited peripheral neuropathy
LDA	Linear discriminant analysis
MAC	Mean absolute value
MD	Muscular dystrophy
MPE	Maximum permissible exposure
MRC	Magnetic resonance coupling
NCV	Nerve conduction velocity
OTA	Operational transconductance amplifier
PCB	Printed circuit board
PFA	Perfluoroalkoxy alkane
PTE	Power transfer efficiency
RF	Radio Frequency
RFID	Radio frequency identification
RNS	Repetitive nerve stimulation
SAR	Specific absorption rate
sEMG	Surface electromyography
WPT	Wireless power transfer

ABSTRACT

Bercich, Rebecca A. Ph.D., Purdue University, May 2016. Improving the Mechanistic Study of Neuromuscular Diseases through the Development of a Fully Wireless and Implantable Recording Device. Major Professor: Pedro Irazoqui.

Neuromuscular diseases manifest by a handful of known phenotypes affecting the peripheral nerves, skeletal muscle fibers, and neuromuscular junction. Common signs of these diseases include demyelination, myasthenia, atrophy, and aberrant muscle activity—all of which may be tracked over time using one or more electrophysiological markers. Mice, which are the predominant mammalian model for most human diseases, have been used to study congenital neuromuscular diseases for decades. However, our understanding of the mechanisms underlying these pathologies is still incomplete. This is in part due to the lack of instrumentation available to easily collect longitudinal, *in vivo* electrophysiological activity from mice. There remains a need for a fully wireless, batteryless, and implantable recording system that can be adapted for a variety of electrophysiological measurements and also enable long-term, continuous data collection in very small animals.

To meet this need a miniature, chronically implantable device has been developed that is capable of wirelessly coupling energy from electromagnetic fields while implanted within a body. This device can both record and trigger bioelectric

events and may be chronically implanted in rodents as small as mice. This grants investigators the ability to continuously observe electrophysiological changes corresponding to disease progression in a single, freely behaving, untethered animal. The fully wireless closed-loop system is an adaptable solution for a range of long-term mechanistic and diagnostic studies in rodent disease models. Its high level of functionality, adjustable parameters, accessible building blocks, reprogrammable firmware, and modular electrode interface offer flexibility that is distinctive among fully implantable recording or stimulating devices.

The key significance of this work is that it has generated novel instrumentation in the form of a fully implantable bioelectric recording device having a much higher level of functionality than any other fully wireless system available for mouse work. This has incidentally led to contributions in the areas of wireless power transfer and neural interfaces for upper-limb prosthesis control. Herein the solution space for wireless power transfer is examined including a close inspection of far-field power transfer to implanted bioelectric sensors. Methods of design and characterization for the iterative development of the device are detailed. Furthermore, its performance and utility in remote bioelectric sensing applications is demonstrated with humans, rats, healthy mice, and mouse models for degenerative neuromuscular and motoneuron diseases.

CHAPTER 1. INTRODUCTION

1.1 Neuromuscular Diseases

Inherited pathologies of the muscles, peripheral nerves, or neuromuscular junctions fall under the broad classification of neuromuscular diseases. Some prominent examples include inherited peripheral neuropathies (IPNs), muscular dystrophies, myasthenic syndromes, and myasthenia gravis. It is estimated that one in 3,500 people worldwide suffers from one of these diseases [1]. In some cases the disease symptoms are barely noticeable and patients live normal, unimpaired lives [2]. For others, though, these diseases lead to muscle weakness and atrophy; numbness or pain in extremities, scoliosis, wheelchair reliance, and cardiovascular or pulmonary complications [3-5]. The ability to improve the compromised quality of life for these individuals hinges on a thorough understanding of neuromuscular disease mechanisms, from which effective therapies can be developed.

IPNs represent a large subset of neuromuscular diseases which will be used throughout this work as an illustrative example, allowing for more specific discussions on the study of disease pathologies and mechanisms. IPNs can lead to premature muscle weakness, dysfunction, and atrophy. They are distinguished from other neurodegenerative disorders such as amyotrophic lateral sclerosis (ALS) or myopathies

like muscular dystrophy (MD) by the fact that their primary pathophysiology occurs in the peripheral axons rather than the motor neuron cell body, neuromuscular junction, or within the muscle fibers themselves. Changes in muscle behavior, strength, and mass in patients afflicted with an IPN are attributed to the impairment of efferent nerves. However, hereditary neuropathies can also affect afferent and autonomic nerves, causing sensory deficits [6] or impairment of the sympathetic and parasympathetic nervous systems [5].

IPNs affect millions of people worldwide with symptoms often manifesting early in life—typically adolescence or early adulthood [7]. This can lead to functional deficits, diminished quality of life, and decreased mobility in patients with severe afflictions of the disease [8]. The most common IPN is demyelinating Charcot-Marie-Tooth (CMT) Type 1 disease [9]. CMT is referred to as a Mendelian disease, meaning it is linked to (and defined by) the mutation of a single gene [10, 11]. CMT types are broadly classified by their primary pathophysiological phenotype: either demyelinating (CMT1 and its subclass, CMT4), axonal (CMT2), or both (DI-CMT and CMTX) [5].

Age of onset and symptom severity vary greatly among patients diagnosed with CMT, even within a particular classification [12]. This is likely due, in part, to environmental factors that either exacerbate or moderate the effects of the main gene mutation. Another possible explanation is the influence of modifier genes on the presentation of main gene mutation phenotypes. Previous work examining a variety of degenerative disease such as retinal dystrophy [13], Parkinson's disease [14], and CMT [15, 16] have suggest that epistatic states can occur in which the phenotypic

presentation of a particular gene mutation depends on the expression of genes from modifier loci occurring within the genetic background. In this way the effects of multiple mutations can synergize to alter disease presentation and progression. This can, in turn, blur the boundaries between disease subclasses and make precise diagnoses difficult [12].

One of the ways in which our understanding of these often complex disease mechanisms can be improved is by creating more advanced tools that allow new or higher quality data to be collected from animal disease models. Sections 1.1.1 and 1.1.2 identify a range of metrics used to characterize neuromuscular disease mechanisms and the experimental protocols used to collect those metrics. These protocols are most often carried out in mice, which serve as the premier mammalian model for most inherited human diseases. *In vivo* electrophysiology is often utilized for direct observation and quantification of disease markers over time. Section 1.2 offers an overview of established methods for long-term electrophysiology in mice. This overview exposes a gap in available instrumentation for untethered, freely behaving mice. Finally, the common need for improved bioelectric sensors in both the study of animal neuromuscular disease models and human clinical applications is addressed in Section 1.3.

1.1.1 Metrics of Neuromuscular Disease Progression

Many difference methods and metrics are used to characterize neuromuscular diseases. In addition to genetic strategies such as DNA sequencing, there are

histopathological and electrophysiological means of discerning disease origins and progression. Amongst these are nerve biopsies, imaging techniques such as magnetic resonance neurography, nerve conduction velocity (NCV), electromyography (EMG), and nerve action potentials (NAPs) [17, 18]. In some instances spontaneous, aberrant activity may also be measured. For example, uncontrolled fasciculation and fibrillations are well-documented in human patients having ALS [19, 20] and MD.

Some metrics such as NCV and compound motor action potential (CMAP) are triggered by applied stimuli. While useful, stimulus evoked potentials only reveal a subset of the functional characteristics of the peripheral nervous system. In some situations, particularly those involving the analysis of disease states, it may be necessary to also observe voluntary evoked potentials in the nerves or muscles.

Animal models—particularly transgenic and knockout mice—play a crucial role in understanding the genetic and molecular factors that contribute to neuromuscular diseases like IPNs [21, 22]. Information can be extracted from these animal models and used to improve understanding disease mechanism, evaluate new therapies, and improve the quality of genetic counseling. This work will focus on the electrophysiological metrics that can be measured in mouse disease models over time to create signatures for disease progression. What follows is a discussion of the different experimental methods that may be used to record bioelectric data from the affected targets of neuromuscular disease, particularly the peripheral nerves and muscles.

1.1.2 Experimental Design

The first decision that must be made in a long-term electrophysiological examination of a disease model is which signal or metric is going to be obtained This will depend on the study hypothesis and what is already known about the model's phenotypes. Once the experimental objective is set, it must be decided whether the data are to be collected from *ex vivo* preparations or *in vivo*. The study of the neuromuscular system and its associated disorders requires functional readouts of muscle and nerve function that can be—and often are—obtained in reduced preparations at fixed time points. Such preparations limit mechanistic interpretations and *in vivo* relevance as well as the ability to track disease progression.

If *in* vivo data collection is part of the experimental protocol, then the benefits of using a single animal over time should be weighed against the use of acute animal cohorts at fixed time points. The benefits of using a single animal over time include expending fewer animals, enabling higher temporal resolution in measured parameters, and allowing data to be normalized internally to each animal for ease of comparison. The relative benefit of using animal cohorts is that it avoids repeated surgical procedures in the same animal and ensuing post-operative care. It is possible for longitudinal single animal studies to enjoy the same benefits as acute animal group studies by using tethered or wireless headstages, which only require a single surgical procedure. These solutions are examined in more detail within the discussion on instrumentation for chronic electrophysiology in Section 1.2.

Finally, the decision should be made whether or not the target signal can and should be measured under anesthesia. Stimulus evoked behaviors will likely be easier to measure if the animal is subdued. However, voluntary evoked and spontaneous aberrant bioelectric activities are suppressed under anesthesia, and will need to be recorded from awake and freely behaving animals.

1.2 Instrumentation for Longitudinal Electrophysiology in Mice

Voluntary evoked nerve and muscle activity carry important information about neuromuscular disease mechanisms. The various instrumentation options for collecting these bioelectric signals in mice over time are covered in this section. The use of tethered apparatuses for longitudinal stimulation and recording of neuromuscular activity in mice is observed only a handful of times within the literature [23, 24]. Tethered setups involve the connection of an animal subject to a data processor through a cable that connects to a headstage, which is typically fixed on top of the animal's head or on the back of the neck. This practice is far more prevalent in experiments that use larger rodent models such as rats: an observation that points to the technical difficulty of installing and anchoring bulky hardware in animals as small as mice. Tethered systems do offer some advantages such as large bandwidth and DC power supplies. However, they can be impractical for collecting longitudinal neuromuscular information. Headstage unseating and lead wire breakage are common culprits in premature termination of animal experiments. Moreover, the physical connection between the animal and the bench top instrumentation impose limitations

on the animal's testing environment. For example, a tethered animal cannot be placed in water or made to move in and around obstacles. In fact, most tethering apparatuses offer very little leeway and confine the animal to a small testing space. This raises additional concerns about the potential for behavioral constructs resulting from the unnatural influence confining and burdening the animal.

Wireless headstages serve as an alternative to tethered headstages, but tend to be bulky and cumbersome. This can cause them be dislodged or damaged during behavioral tests or normal animal activity. Moreover, wireless headstages are typically intended and configured for neural recording in the cortex. In order to measure signals from the peripheral nerves and muscles, these devices would have to be fitted with longer leads that can be routed to remote targets.

Table 1.1 compiles the performance specifications for a series of fully wireless and commercially available devices that may be used for chronic biopotential measurements in mice. Four crucial observations should be made about the information in Table 1.1. First, there is no fully wireless recording device which enables both biopotential acquisition and stimulation, which would be an incredibly powerful tool for closed-loop control of bioelectric systems. Some fully wireless standalone stimulators have been developed for mice [25-27], but they do not have biopotential recording capabilities. Second, none of these sensors gives the user the ability to adapt the functional protocol for different experimental needs, making them one-size-fits-all solutions. Third, the bandwidths and associated sampling rates of these fully wireless systems are, in almost all cases, too low for a majority of useful nerve and muscle measurements, which can

have frequency content up to a few kHz. Lastly, almost all of these systems rely on batteries and therefore have finite lifespans (typically one to two months). It should be noted that the recording device from Triangle BioSystems, which does offer a large enough bandwidth for EMG and NAP is a battery powered headstage with a battery lifespan of up to 4.2 hours [28].

Table 1.1 Summary of available fully wireless bioelectric sensors for mice. Devices that are not wirelessly powered utilize a battery power supply.

Product	*Wireless Power (Yes/No)*	*Integrated Stimulator (Yes/No)*	*Adapt. Program*[1] *(Yes/No)*	*Device Volume (cm^3)*	*Min. Animal Mass (g)*	*Number of Biopotential Channels*	*Channel Bandwidth (Hz)*
HD-X11 (Data Sciences International [29])	No	No	No	1.4	19	1	0.1-200
F20-EET (Data Sciences International [29])	No	No	No	1.9	20	2	1-50
EPOCH-MSE-SYS (BIOPAC Systems, Inc. [30])	No	No	No	0.76	10	2	0.1-100
MT10B (Millar [31])	Yes	No	No	1.4	22	1	2-440
W-Series[2] (Triangle BioSystems International [28])	No	No	No	4.54	--	5	0.8-7,000

[1]Adaptable programming refers to the ability to change the sensor's functional protocol in firmware.
[2]This product is a battery powered headstage and is not fully implantable.

1.2.1 Battery Powered Implants

Battery powered devices have the advantage of storing energy chemically, which reduces energy waste and makes it more efficient than any other wireless powering

solution [32]. An onboard battery is an appealing powering solution for fully wireless recording device. The best evidence for this might be the ubiquitous use of batteries in commercial hardware as shown in Table 1.1. Batteries are highly portable and proximate energy reservoirs that evade the losses from free space energy dissipation and tissue attenuation, which are significant concerns in wireless power coupling [33-35]. However, the energy storage capacity of a battery is directly related to battery volume, which has implications for the implant size. The most significant disadvantage of single-charge (primary) batteries is the repeated, invasive surgery required to replace them. It is worth noting that in some cases a hybrid system consisting of a rechargeable (secondary) battery or capacitor in combination with remote powering for cyclical charging and discharging can be an effective powering strategy [36, 37]. However, continuous data collection at high sampling rates precludes the use of any battery power source for long-term, fully implantable solutions.

1.2.2 Potential for Energy Harvesting Implants

Energy harvesting or scavenging is a broad term for the collection, storage, and use of energy (thermal, mechanical, metabolic, photonic, etc.) from a system's environment [32]. Energy harvesting might be used to collect trace amounts of energy from proximate sources, convert it to electrical energy, then use that energy to power an integrated circuit (IC) that can measure or modulate some biological activity. Since the sources of energy come from the environment it may be thought of as "free" energy and, if sufficient levels of energy can be collected, might negate the need for a battery

or tethered connection to a power source. However, many harvesting strategies either exhibit low conversion efficiencies or face significant practical limitations that limit their usefulness in active implantable devices. The efficiency of a mechanical piezoelectric system, which depends on its material and resonance of the mechanical stimulation, is in one case reported to be 0.46%. When one considers that the existing energy in this source is already extremely low, it seems this strategy may only be sufficient for extremely low power systems. The lack of solar energy available within the body prevents the use of more efficient photovoltaic cells and inadequate temperature gradients make effective thermal energy conversion within the body difficult [38].

1.2.3 Wireless Power Transfer Strategies for Implants

Wireless power transfer (WPT) is a method of converting incident electromagnetic fields generated in the radio frequency (RF) band into an electrical current [39]. This current can then be used to power an IC that can perform the desired tasks of recording, filtering, transmitting, and stimulating biological signals. This idea of remote powering is an extremely powerful one for implantable systems as it offers a continuous supply of energy constrained only by the efficiency of the wireless link and the limits for exposure of tissue to RF electromagnetic fields—a concern which will be explored thoroughly in Section 2.2.

Remote powering has been employed in a variety of implantable device applications because it circumvents many of the previously discussed detriments of battery powered implants or tethered apparatuses for chronic collection of bioelectric

information. Different WPT strategies can be categorized by the type of link between the source of the electromagnetic field and the receiving structure. These links may be inductive, radiative, or a combination of inductive and radiative. Inductive links couple energy in the near-field region whereas radiative links collect energy from the far-field region of an electromagnetic field source. The transition from near-field to far-field is gradual, but a typical heuristic used to define the upper bound of the near-field is $2D^2/\lambda$ where D is the largest dimension of the radiating body and λ is the wavelength of the RF source [40].

Near field (inductive) coupling is the most prevalent form of WPT used for implantable devices. This is, in part, a result of over a century of work devoted to characterizing and optimizing the behavior of inductive links [41]. Inductive energy coupling is the same phenomenon used in a transformer; a current applied to a primary conductive coil generates a magnetic field which induces current in a separate (secondary) conductive coil. Crucially, the amount of energy transferred in this arrangement is strongly affected by the alignment, proximity, and matching of both coils' physical properties [39, 42]. This knowledge dates back to the work of Nikola Tesla, who revealed the significance of coil turning and resonance to energy coupling efficiency, which he used to wirelessly illuminate vacuum tubes [43]. The other reason that inductive power coupling is frequently used for WPT to implants is the fact that biological tissue has an extremely low magnetic susceptibility, making it is essentially invisible to magnetic fields [39, 44].

One of the early successes for inductive power coupling in active biomedical implants was its use to charge a cardiac pacemaker battery in 1960 [45]. Today, this form of WPT is used for a variety of biomedical applications such as cochlear implants [46, 47], blood pressure monitors [37], electrocardiogram (EKG) sensors [48], EEG electrodes [49], and human EMG acquisition [50]. The broad application of near-field inductive power coupling for biomedical and other commercial applications stems from many years of experimentation with different parameters (coil diameter, number of turns per coil, coil alignment, operating frequency, etc.) to improve PTE [51-53]. It is well known that the PTE of an inductive link is strongly affected by the mutual inductance of the primary and secondary coils. This mutual inductance is derived from the physical properties and spatial relationship of the primary and secondary coils and can decrease rapidly as a result of increased separation or angular misalignment of the two coils relative to one another [34, 39, 42, 54]. A study conducted by William Heetderks in 1988 evaluated five inductive coil arrangements for powering relatively small implants within various parts of the body. The results of this study indicate that there are inherent inefficiencies in inductive systems when there is a large discrepancy between powering and receiving coil size [51], which would invariably be the case for a miniature system suitable for implantation within a mouse.

The relationship between PTE and coil size in inductive links is one that is disadvantageous to WPT in very small animals. Solenoid coils are bulky and, with an increasing number of turns, comes additional mass and volume--both of which are at a premium. The use of pancake coils is one strategy that exists to sidestep this problem.

Printed spiral coils are one implementation of the pancake coil and are fabricated by printing the desired coil shape with a conductive material on an insulating substrate. This may be done using a strategy like photolithography or milling from a copper-clad sheet. Uei-Ming and Ghovanloo demonstrated a PTE between pancake coils as high as 86% at a separation distance of 1 cm in free space [54]. These sorts of flat coils have the potential to be integrated with clothing on account of their thin profiles and flexibility when fabricated on very thin substrates. This could be useful for powering implantable systems for collecting neural information for directing a prosthesis or monitoring physiological parameters [55]. Sections 3.3.3 and 4.2.2 detail the fabrication of printed spiral coils designed specifically for implantation in small animal monitoring. When paired with a purely inductive power coupling scheme, however, these pancake coils present the same limitation as solenoid coils. That is, mutual inductance (and thereby, PTE) can vary drastically—and unpredictably in the case of a freely behaving animal—as a result of even minor misalignments and separations of more than a few centimeters between the primary and secondary coils [34, 53]. For these reasons a purely inductive WPT link is deemed unsuitable for an implantable system in freely behaving animals.

Far-field RF powering distinguishes itself from near-field RF powering in that it extracts energy from the radiating region of an electromagnetic field rather than the nearby inductive region. Traditional applications of far-field wireless links include radar, wireless communication, and radio frequency identification (RFID) tags [41].The transmission and collection of far-field power transfer took off in the 1960s when it was first demonstrated that radiative fields could be focused in space rather than spreading

isotropically. This vastly improved the transmission efficiency of far-field links, making it a more attractive solution for those interested in coupling energy from radiating fields [56, 57].

The improvements in far-field efficiency that came with the development of waveguide transmission were accompanied by improvements to RF rectifiers, which can be used to generate stable DC currents from oscillating electromagnetic fields. This progress was aided greatly by advances in semiconductor diodes [58]. There have since been a number of efforts in the way of increasing RF rectifier efficiency [59, 60]. Soon after the development of the RF rectifier came the conception of the rectenna: a rectifier circuit plus a receiving antenna in one portable assembly. One of the first applications of the rectenna was a remotely powered helicopter, which was an effort headed by William Brown in the 1960s. Brown pointed out that the changing orientation of the target device (in this case a helicopter) necessitated a powering strategy with some immunity to the constantly shifting physical arrangement of the receiver relative to the source [61]. This idea carries over into the field of chronically implanted sensors as there is, likewise, a good deal of inherent unpredictability in defining the spatial relationship between the device within the animal and the external powering unit.

One prevalent and related use for far-field powering and telemetry is RFID tags. The rapid growth of the technology came as a result of miniaturization and expanded capabilities of complementary metal-oxide semiconductor (CMOS) technology. RFID tags are used for applications such as highway tolling and merchandise tracking. Occasionally these devices perform the desired tasks using only incident RF energy as a

power source. Each tag has an integrated transponder or IC that allows it to emit either a fixed identification or recorded signal of interest when interrogated [60, 62].

The ubiquitous nature of far-field links in today's world and the robustness of these links to changes in receive antenna orientation might lead one to expect that far-field power transfer for implantable sensors is common practice. However, application of far-field WPT in implantable devices is limited. This might be partially attributed to the added complexity of antenna design when its functional properties can be altered by the properties of proximate dielectric mediums such as biological tissue [63, 64]. The more likely impediment, though, is the fact that operating frequency and signal attenuation of radiative electromagnetic fields in lossy dielectric mediums such as biological tissue are positively correlated [33, 35]. Additionally, smaller antennas (which are needed for very small implants) resonate at higher frequencies. The resonant frequency of the receiving antenna has a bearing on the antenna gain, so energy loss occurs when the incident electromagnetic field frequency does not match the resonant frequency of the antenna. Thus, it is prudent to assign antenna dimensions based on the intended operating frequency. There is the additional point that far-field RF links have traditionally operated at higher frequencies to take advantage of increased bandwidth and reduced interference with other wireless transmissions [65]. Combining this information results in the following crucial point: the interplay between antenna size, electromagnetic field (operating) frequency, and energy attenuation in tissue must be well understood in order to create an effective WPT link and may render far-field WPT unsuitable for some applications.

This might serve to illustrate why far-field WPT has been largely dismissed as a viable solution for continuous power transfer to microelectronics implanted in a body. Some exceptions include the work of Le *et al* [59] and Radiom *et al.*[66]. Their results suggest that perhaps in the right environment, with a carefully configured electromagnetic field source, and an implantable device with appropriately low power consumption, far-field power coupling may be sufficient for continuous device operation within a freely behaving animal. Chapter 2 explores the feasibility of a far-field RF power coupling strategy for this application. It also contains a detailed analysis of the complete power link budget for a far-field RF link, a summary of findings from a model using finite element method (FEM) analysis, and a discussion of the broader implications of those findings for the utility of far-field WPT for implantable sensors.

The final wireless powering strategy that will be considered here is magnetic resonance coupling (MRC), which uses series resonators to optimally impedance match both the primary and secondary coils. This is a way of tuning the system and thereby increasing the quality factor, Q, for a particular set of non-optimal conditions for inductive links (poor angular alignment, large coil-to-coil separation, etc.). The quality factor is a numerical representation of the strength of coil coupling which depends on the previously discussed mutual inductance, operating frequency, and series resistance of the coils [67]. In this way MRC has the potential to greatly exceed the PTE observed in inductive links under conditions in which the primary and secondary coils are poorly coupled [68, 69]. Since this was the key impediment to using purely inductive power coupling to run devices implanted in freely behaving animals, MRC presents an exciting

alternative that ultimately proves to be the most efficacious wireless powering solution for this application.

The development of an implantable, single-channel recording device that is compatible with MRC power transfer between two poorly coupled inductive coils is the subject of Chapter 3. Recently, the same theory governing MRC between two conductive coils was used to create a resonant cavity structure which offers the largest available WPT environment for freely behaving animals [70, 71]. The subject of Chapter 4 is the design and implementation of a multifunctional device capable of functioning while implanted in freely behaving animals housed within the resonant cavity.

1.3 Wirelessly Powered Sensors for Upper-Limb Prosthesis Control

In addition to the multitude of potential animal research applications, fully wireless bioelectric sensors also have utility in the human clinical sphere. An exciting frontier in rehabilitation of upper-limb amputees is how myoelectric control systems can be made to work synergistically with chronic intramuscular electromyography (imEMG) to improve the performance of sophisticated electric-powered prostheses [50, 72].

For many upper-limb amputees the devastation of limb loss is often coupled with disappointment in the performance of commercially available prostheses. When a replacement limb falls short of a patient's expectations—that is, the control is unintuitive, the response to a mental command is excessively delayed, or the prosthetic itself is heavy and uncomfortable—the frustration can lead the patient to abandon the prosthesis entirely [73, 74]. The human arm has 28 degrees of freedom [75]; it is a highly

dexterous and complex system, which makes it difficult to replicate and command. There is a need to address these frustrations, which are so common amongst upper-limb amputees. There is an especially critical need for improved neural interfaces for transhumeral, shoulder disarticulation, and bilaterial amputees. These individuals have lost significant ability, may be highly dependent on others, and present unique challenges to prosthetic design and control.

It comes as a surprise to some that the main adversity to meeting the expectations of upper-limb amputees is not a lack of sufficiently advanced prostheses. In fact, a robotic (powered) upper-limb prosthesis capable of over twenty degrees of freedom has been developed [76]. Additionally, there is a well-developed solution space for prosthesis control algorithms that work with various neural interfaces [77-83]. However, the use of sophisticated prostheses and control algorithms are both limited by the lack of sufficient motor control information. In both cases there is a need for a greater number of independent channels of neural information in order to decipher and manage the dynamics of so many degrees of freedom simultaneously [73, 84].

Most upper-limb amputees who are fit with an electric-powered prosthesis use surface electromyography (sEMG) to control their artificial limb [85]. The selection of recording locations on the residual limb depends on the level of amputation (transradial, transhumeral, shoulder disarticulation, etc.), whether or not the patient is willing to undergo additional surgery such as targeted muscle reinnervation (TMR) [84], and whether conventional amplitude-based [77] or pattern recognition control methods [84, 86] are used.

Regardless of electrode location, sEMG is often limited in its use by signal cross-talk as well as variability in electrode impedance and position from sweating, shifting of the socket, and donning/doffing of the prosthetic; all of which can necessitate recalibration of the system [78] or reduce the functional performance of the control system [72, 80]. While more invasive, imEMG offers significant advantages when it comes to signal reliability and specificity, which could enable the use of more advanced and efficacious control algorithms not just in the controlled environments of labs and clinics, but in-home as patients take on diverse daily tasks.

The last five years have seen some advances in chronic, wirelessly powered intramuscular recording systems for upper-limb amputees [87-89], including the first human trials [50]. However, due to the purely inductive method of power coupling employed by these systems, the efficacy of their WPT links can vary drastically as a result of minor misalignments or separations of the primary and secondary coils [53, 90].These systems of are useful in applications where all target muscles are relatively close together and/or positioning of the on-board coil(s) are fixed relative (and in close proximity) to the external coil. Their use may be limited in other configurations where the external coil is prone to shifting or when an external coil cannot be wrapped around all target muscles. A compelling example of this might be an array of devices embedded in muscles within the chest and shoulder of an amputee following TMR surgery, which has been established as a pragmatic method for enhancing the performance of myoelectric prosthesis control, particularly in proximal upper-limb amputees [84, 91].

The surgical procedure for TMR in upper-limb amputees was pioneered by Dr. Todd A. Kuiken and Dr. Greg Dumanian. The surgery itself involves rerouting various branches of the residual brachial plexus nerve bundle to denervated muscles in the shoulder or chest of an amputee. Over the course of three to six months these muscles become reinnervated by the nerves that used to be responsible for directing movements in the hand and arm. So these reinnervated muscles will contract in unique ways in response to motor commands intended for the missing limb. The ultimate advantage of this procedure is that is provides easier access to electrical activity that can be correlated with the intent of the patient, enabling intuitive control mechanisms in which the patient does not have to re-train their motor cortex. All of the learning is done by a processor equipped with a control algorithm.

TMR surgery takes advantage of a process called hyper-reinnervation, which refers to the regrowth of axons when a nerve containing a greater number of fibers is affixed to a smaller, previously incised nerve containing fewer fibers. The smaller nerve is distal to the larger nerve and usually innervates either a single muscle or a small group of muscles. Hyper-reinnervation increases the odds that a fiber in the smaller nerve will form a connection with a fiber in the larger nerve and eventually lead to muscular reinnervation [92]. The process of muscular reinnervation takes place as a result of axonal regrowth guided by residual Schwann cells from old nerve sheaths. This process reestablishes the link from the brain's motor cortex to a muscle's neuromuscular junctions so that muscle contracts are once again evoked as a result of motor commands [93]. There are a number of interesting phenomena that occur as a result of

hyper-reinnervation, some of which have proven to be highly advantageous to the rehabilitation of transhumeral and shoulder disarticulation amputees [94, 95].

Hyper-reinnervated muscle exhibits some unique characteristics compared to self-reinnervated muscle (resulting from re-appending the two ends of the same nerve following an incision) or native muscle. First, hyper-reinnervated muscle recovers more mass and strength due to the increased probability of any give muscle fiber being reinnervated and the increased chance for polyneuronally innervated fibers. The most important artifact of hyper-reinnervation, though, is the spatial segmentation of motor units. Hyper-reinnervated muscles tend to have smaller motor units that cluster together instead of being distributed homogenously among other motor units, which is the case in native muscle [92, 96]. This behavior would improve signal selectivity of an implanted bioelectric sensor by granting the ability to place that sensor within clustered muscle fibers belonging to the same motor unit. Since a single motor unit encodes information about a very specific motor command, this would address the previously declared need for a greater number of independent channels of neural information in order to realize the full potential of sophisticated robotic prostheses and control algorithms.

Furthermore, muscle has been demonstrated to be a viable environment for chronic implants. Long-term acceptance of an implanted device by proximate muscle can be expected provided the implant packaging is biocompatible and hermetically sealed [97]. Following implantation the encapsulation and anchoring of implants has been observed, which may initially change the amplitude and spectrum of the recorded

potentials. However, the tissue environment surrounding the implant will eventually stabilize, leading to output signals which have consistent qualities over time [98, 99].

In summary, the TMR procedure offers a number of advantages that could work synergistically with fully wireless and implantable imEMG sensors to greatly improve upper-limb prosthesis control for upper-limb amputees [79, 100]. However, due to the abnormal arrangement of motor units at reinnervated muscle sites [101], a viable companion system for chronic imEMG acquisition would need to be able to accommodate variable and scattered device positions. Even upper-limb amputees using EMG from native muscle to control their prosthesis would benefit from a more versatile wireless powering strategy that can accommodate imperfect or non-stationary alignment inherent in real-world use. The desired level of flexibility in orienting remote sensors to an electromagnetic field source for this application presents a similar challenge to the one faced in freely behaving animal monitoring. In short, they both require a flexible, robust WPT strategy and an implantable recording device that is compatible with that WPT strategy, so it is possible that both instrumentation needs might be addressed at the same time. Chapter 3 includes a demonstration and discussion of how the wireless recording devices developed in this work might contribute to the clinical field of upper-limb prosthesis control.

1.4 Conclusion

The ongoing study of neuromuscular disease pathogenesis could be aided by tools which enable long-term electrophysiology in mice under conditions that do not involve

tethering or anesthesia. There is no fully wireless system either on the market or within the literature that can both record from and stimulate excitable tissues in awake, freely behaving mice. Existing wireless systems for biopotential acquisition are limited by at least one of the following points: finite lifespan from battery power supply, low quality of data resulting from low (200 Hz or less) bandwidth, limited information output from by a single recording channel, and unsuitability for implantation owing to large dimensions.

This leads to the principle objective of this work, which is to create novel instrumentation that will augment the study of neuromuscular disease mechanisms by significantly improving the ability track relevant electrophysiological metrics in a single mouse over time. A fully wireless and implantable device with the ability to both measure and evoke bioelectric activity would, in many ways, represent a significant improvement over current devices intended for electrophysiology in untethered, freely behaving mice (see Table 1.1). This implant would also be uniquely advantageous for studying certain other diseases. For example, cortical activity in rodent epilepsy models could be measured continuously to predict and then possibly curtail spontaneous seizure events through stimulation. The breadth of potential uses for an implantable closed-loop device are exciting but outside the scope of this work. However, hereditary motoneuron diseases like ALS manifest through phenotypes which are often similar to those observed in neuromuscular diseases and will be considered herein.

The challenge of making an active, fully implantable sensor that is suitable for long-term implementation in very small animals requires careful consideration and balancing

of key system characteristics such size, performance, adaptability, reusability, and biocompatibility. This engineering design problem tenders the following criteria for success: 1) the device must be small enough to be fully implanted in a mouse; 2) the device must have sufficient functionality to be useful for a variety of electrophysiological experiments; 3) once implanted, the device must be able to function longitudinally in the living environment; 4) the device as well as its paired environment for WPTmust enable the continuous, long-term collection of bioelectric activity from freely behaving mice.

CHAPTER 2. FEASABILITY OF FAR-FIELD WIRELESS POWER TRANSFER FOR IMPLANTABLE ELECTRONICS

2.1 Introduction

The material presented in this Chapter incorporates content from the journal article “Far Field RF Powering of Implantable Devices: Safety Considerations” by R. Bercich, D. Duffy, and P.P. Irazoqui, which is published in IEEE Transactions on Biomedical Engineering [35]. © 2013 IEEE.

Wireless energy coupling offers clear advantages over wired, battery powered, and energy scavenging strategies for chronically implanted sensors and stimulators (see Sections 1.2 and 1.3 for discussion on these strategies). Wireless powering negates the need for recurrent surgeries to replace batteries and sidesteps the issues with lead wires that risk infection by breaching the skin barrier and are prone to break or dislodge as a result of fatigue and micromotion.

It is useful here to reexamine the criteria for success for this work, which are summarized in Section 1.4. Briefly, a miniature, multifunctional device that supports continuous WPT while enabling long-term data acquisition is needed for chronic animal and clinical applications. It is important to note early on in the design process that these objectives are interdependent and oftentimes destructive to one another. For example, it may be desirable to implement sixteen channels of recording so that large quantities

of neural information may be collected. However, this would add complexity to the device's functional protocol, increase power consumption, and likely add volume to the implant. This could result in a finished product that is too large to be implanted or one which requires more power than can be reliably and continuously coupled from the source.

Much of the work that goes into developing WPT solutions seeks to improve some form of power transfer efficiency (PTE). In the case of WPT to an implanted device, PTE is defined as the percentage of energy from a source that is received by the target device and may be expended for some useful purpose such as lighting an LED for optogenetics [102, 103] or driving an IC that samples and transmits bioelectric data. It is crucial that the range of a wireless link's PTE is well characterized when devising a strategy for WPT to a device having an unpredictable location and orientation—as would be the case within a freely behaving animal. This is important because the minimum PTE must be sufficient to meet the power requirements of the device and the maximum (peak) PTE must not be so large that damage might be done to the circuit components, which have voltage and power dissipation limits. The limitations of a purely inductive WPT strategy have been detailed in Section 1.3.2.

Far-field RF powering is an attractive solution to the challenge of coupling energy to non-stationary remote devices because its PTE is less dependent on proximity of the electromagnetic field source and the receiving device than that of near-field RF powering. This is due to the fact that the energy density in the radiative field decreases inversely with the square of the distance(proportional to $1/r^2$) as compared to the

inductive field in which energy density decreases with $1/r^3$ where r is the distance between the field source and the receiver in free space [104, 105]. However, far-field powering in the application of implantable devices introduces the obstacle of power density attenuation as the electromagnetic waves pass through tissue and tissue boundaries. Absorption and reflection of radiated energy in addition to the free space path loss all diminish the power return at the receiving antenna and decrease the PTE of the WPT link.

The obvious solution to high energy losses from energy spreading and attenuation in tissue might be to increase the power output at the source. However, there are exposure limits set by the Federal Communications Commission (FCC) that restrict how much power may be incident on the surface or absorbed in a given volume of tissue [106] as excitation from oscillating electromagnetic fields can have adverse effects on tissue by way of both thermal and non-thermal mechanisms [107-110]. Thus, a careful consideration of the safety thresholds is necessary and will set the constraints for an analysis of the power link budget. Understanding the receive power capabilities of a far-field WPT link will be assistive in determining the value of this solution compared to other wireless powering strategies.

The viability of safely coupling energy from the far-field of a radiating body to power an implantable recording device is explored in Sections 2.2 through 2.4. It will also be important to demonstrate that local temperature spikes resulting from thermal discharge of the implanted microelectronics will not cause damage to proximate biological cells and tissues. It is important that the temperature of the tissue

surrounding the device does not increase by more than a few degrees as various studies have shown that temperature increases greater than 2 °C can have adverse effects on living cells [111-114]. An experiment that tests the thermal safety of active implantable is the focus of Section 2.5.

2.2 Safety Constraints for Far-Field RF Power Transfer

The first point that should be noted in building a power transfer link in tissue is that the PTE will be affected significantly by the chosen operating frequency, f. This is because the efficiency of the receiving structure—an antenna in this case—is strongly impacted by the wavelength, λ, of the incident electromagnetic field which is related to f by the relationship $f = c/\lambda$ where c is the speed of light. In order to maximize the efficiency of energy transfer, the receiving antenna should be tuned by precise selection of its dimensions for the chosen operating frequency. For example, dipole antennas are often used as receivers of far-field RF waves and will resonate with the oscillating field when their length is $\lambda/2$ or $\lambda/4$. Resonant conditions are desirable as they minimize losses and improve overall PTE, however the antenna length needed to achieve resonance is inversely proportional to the operating frequency. Resultantly, there is a lower limit for the RF field frequency when working with very small receiving devices (such as those that are suitable for implantation in mice) where the antenna length may be limited to a few centimeters. For this reason the proceeding far-field WPT analysis will examine the effects of f in the range of hundreds of MHz to GHz.

The extent of RF energy absorption in tissue will also be affected by *f* since the dielectric properties of tissues are frequency dependent [115]. Furthermore, it is known that RF attenuation is positively correlated with *f [116]*. This would encourage a lower operating frequency, which stands in opposition to the incentive to use higher frequencies for the sake of smaller receiving antennas. As a result *f* must be chosen such that antenna losses are balanced with losses from tissue attenuation. In practice, it is best to use an operating frequency which lies within an industrial, scientific, and medical (ISM) radio band since these are approved and reserved for purposes such as implantable devices. For this reason, the following ISM band frequencies will be considered in this analysis: 915 MHz, 2.4 GHz, and 5.8 GHz.

The first safety consideration for the use of a radiating source is the time averaged surface exposure of tissue. The standards for maximum permissible exposure (MPE) are outlined in Table 1 of Section 1.131 in Title 47 of the Code of Federal Regulations, which outlines permissible use of telecommunication systems. The FCC standard for uncontrolled exposure to an intentional radiator depends on the operating frequency. The MPE limit for exposure to an electromagnetic field is given as an average over 30 minutes and is 2 W/m^2 in the range of 30—300 MHz; *f/1.5e8* W/m^2 in the range of 300—1,500 MHz, where *f* is the operating frequency in Hz; and 10 W/m^2 in the range of 1,500—100,000 MHz. This translates into an average MPE limit of 6.1 W/m^2 at 915 MHz and 10 W/m^2 at 2.4 GHz and 5.8 GHz [106]. These particular limits will be used in the subsequent theoretical and numerical link budget analyses as their corresponding ISM

frequencies (915 MHz, 2.4 GHz, and 5.8 GHz) are considered suitable for the scale of the receive antenna needed for this work.

The second safety standard established by the FCC for an antenna operating at RF frequencies is a set of restrictions for power absorption in tissue. This includes a whole-body average specific absorption rate (SAR) limit, which is 0.8 W/kg, as well as a peak spatial SAR limit evaluated over any 1 g cube of tissue, which is 1.6 W/kg [106]. The surface exposure and the SAR experienced by any nearby human or animal tissue must remain below these established safety limits while power transfer is taking place to an implanted device.

The efficiency of energy transfer between an electromagnetic field source in free space and a receive device embedded in tissue will depend on many factors. These include characteristics of the source such as output power, efficiency (which takes into account dielectric and parasitic losses), directivity, and operating frequency. It will also depend on free space dispersion, tissue attenuation, and reflections at boundaries between materials with different dielectric properties such as air, skin, adipose, muscle, bone, etc. After all of these losses have been accounted for there will be some power flux density incident on the receiving antenna which can be converted into usable energy. The conversion between this power flux density at the surface of the device and the power budget available to run the device's embedded microelectronics will depend on the directivity and efficiency of the receiving antenna as well as the efficiency of the rectification circuit used to convert the incoming AC current to a stable DC supply voltage. This evaluation of power transfer which accounts for all potential losses in a

wireless link is referred to as a link budget analysis. What follows is the complete link budget analysis for far-field RF power transfer between an external radiating source and a device implanted in mammalian tissue.

The amount of energy that exists at some distance from an electromagnetic field is often given per unit area in the form of power flux density. In free space the power flux density at some distance, *x*, from the radiating source can be found using the following relationship [40]:

$$S(x) = \frac{EIRP}{4\pi x^2} \tag{2.1}$$

where EIRP is the equivalent isotropically radiated power from the antenna (equal to the product of antenna input power, P_t; antenna gain, G_t; and the efficiency of the antenna's matching network, e_{mn}). By setting *S(x)* equal to the MPE limit (for example, 10 W/m^2 at a frequency of 2.4 GHz), a relationship emerges between antenna-tissue separation and the transmitting antenna characteristics that must be satisfied in order to guarantee safe exposure levels:

$$x = \sqrt{\frac{P_t G_t e_{mn}}{40\pi}} \tag{2.2}$$

For example, if the radiating antenna is isotropic (gain of 0 dB in all directions), has a matching network efficiency of 100%, and is given an average input power of 1 W (30 dBm), then the minimum separation distance between that antenna and any part of the body must be 8.92 cm. This is one constraint to consider when constructing a model for the WPT link and in practice if this wireless powering strategy is used.

The second safety constraint established by the FCC pertains to energy absorbed in a volume of tissue. Assuming a one-dimensional power flux though a volume of tissue having a cubic form factor, the peak spatial SAR can be expressed as:

$$P_{abs} = a^2(S_0 - S_a) \tag{2.3}$$

where S_0 is the power flux density transverse to one face of the cube, S_a is the power flux density transverse to the opposite face of the cube, and a is the side length of the cube. Using the average density of human tissue, ρ = 1.04 g/cm^3 [115], the side length, a, corresponding to a tissue mass of 1 g is calculated to be 9.87 mm. It is also known that the power flux density will decreases exponentially over the distance, a, in accordance with the following relationship:

$$S_a = S_0 e^{\frac{-2a}{\lambda_d}} \tag{2.4}$$

$$\lambda_d = \sqrt{\frac{1}{\pi f \mu_0 \sigma}} \tag{2.5}$$

where f is the powering frequency, μ_0 is the permeability of free space (1.257e^{-6} N/A^2), and σ is the conductivity of the tissue at a given frequency. The term λ_d refers to the skin depth—the depth at which the amplitude of the electromagnetic field is reduced by a factor of e^{-1} [116]. So if the powering frequency is set to 2.4 GHz (at which point the conductivity of human tissue is 1.81 S/m [115]), the skin depth will be 7.64 mm. Substituting (2.4) into (2.3) yields an expression for the power absorbed by a cube of tissue depending on the power flux density at the surface of the cube:

$$P_{abs} = a^2 S_0 (1 - e^{\frac{-2a}{\lambda_d}}) \tag{2.6}$$

Rearranging (2.6) gives an equation for the absolute maximum power flux density that may occur in tissue:

$$S_0 = \frac{P_{abs}}{a^2 (1 - e^{\frac{-2a}{\lambda_d}})} \tag{2.7}$$

Using the known values of a and λ_d while substituting the peak spatial SAR limit (1.6 W/kg) for P_{abs} in (2.7) yields an absolute power flux density limit of 17.76 W/m^2. This results in the following guidelines for RF field exposure at 2.4 GHz: the average power

flux density averaged over 30 minutes cannot exceed 10 W/m^2 because of the MPE limit and the average flux density cannot for any length of time exceed 17.76 W/m^2 because of the local SAR limits. Equation (2.6) may be used to estimate the peak local SAR under the condition that the MPE limit has been reached by substituting 10 W/m^2 for S_0. This yields a peak local SAR of 0.90 W/kg. This number will serve as a point of comparison and validation for the FEM analysis described in Section 2.4.

The antenna-tissue separation needed to meet peak local SAR limits can be found using the peak power flux density and the relationship in (2.1). Given the same powering conditions as the previous example (isotropic antenna with 100% efficiency and 30 dBm input power), the calculated minimum separation is 6.69 cm. This is less than the antenna-body separation required to meet the MPE limits (8.92 cm), so it can be said that these powering conditions are within the safe limitations for RF electromagnetic field exposure so long as the antenna-body separation is >8.92 cm. This series of calculations can be performed on any set of powering conditions in order to establish the minimum antenna-body separation and corresponding maximum input power that will satisfy the FCC safety guidelines. For example, imagine that the desired antenna-body separation for a particular application is 1 cm. The average input power to an isotropic antenna would need to be reduced from 30 dBm to 11 dBm in order to satisfy the MPE limit and the free-space loss would, likewise, decrease by 19 dB. In the case of an isotropic source antenna this might be a good power saving strategy since the power flux density incident on the tissue surface remains at MPE limit yet the power input to the source has been reduced by a factor of almost 80. However, when an

antenna with directive gain is used, moving that antenna closer to the body may significantly restrict the space in which a device can receive adequate power. This would not be an optimal scenario in the case of a freely behaving animal which may be placed in a variety of environments for data collection. It would be necessary that the entire volume of the selected testing environment be within an area of the radiating electromagnetic field where the power flux density is larger enough to sustain the implant's power budget. For this reason the radiation pattern, antenna-tissue separation, input power, and exposure limits must all be taken in to consideration when designing a practical far-field RF powering system for implantable devices.

2.3 Power Link Budget for Far-Field RF Energy Coupling

The power link budget is a calculation of the amount of power received from a wireless link once all losses and inefficiencies have been accounted for. The powering conditions calculated in Section 2.2 are used here to approximate the link budget for a far-field RF WPT link to a receive device embedded in tissue. This will be used to draw conclusions about the receivable power limits and, as a result, the feasibility of far-field power transfer for this particular application.

The theoretical power link budget analysis begins with the assumption that all power incident on the tissue surface is absorbed. In this way a boundary condition for the power flux density may be imposed at the tissue surface and will be set to the MPE limit, which is a function of the electromagnetic field frequency. Equation (2.4) may then be used—with the MPE boundary condition substituted for S_0—to calculate the average

power flux density at the depth of the implant, S_d. The amount of useable power received by the device after voltage rectification, P_r, will depend on the incident power flux density, S_d, as well as the efficiency of the rectification circuit, e_{rec}; the efficiency of the matching network, e_{mn}; the receiving antenna power gain, G_r; and the field wavelength, λ, according to the following relationship [40]:

$$P_r = S_d \frac{e_{rec} e_{mn} G_r \lambda^2}{4\pi} \tag{2.8}$$

The power gain of the receive antenna (G_r) is the product of the antenna's directivity (measured in dBi) and efficiency. Equation (2.8) illustrates how the level of power received by an implanted device can be influenced by the RF-to-DC conversion circuit efficiency as well as the gain of the receive antenna. It is worth noting that the efficiency of an RF-to-DC conversion circuit tends to increase as the amplitude of the input RF power increases. This behavior has been observed in previously developed rectenna assemblies designed to operate at 2.45 GHz, which have conversion efficiencies that range from 48% at -5 dBm [117] to 15.7% at -20 dBm [118]. Receive antenna gain can also vary significantly with the antenna's size, geometry, and construction [117]. The size constraints imposed by small implantable devices – specifically those appropriate for implantation in mice—make efficient antenna design difficult. This is especially true at lower operating frequencies where longer wavelengths

necessitate larger antenna dimensions in order to achieve resonance and higher power gain.

In one example constructed by Chow et al. [119], a quarter wavelength antenna is designed for implantation in the anterior chamber of the eye in order to measure intraocular pressure. The operating frequency in this example is 2.4 GHz, which means the implanted antenna is approximately 3.1 cm in length. The simulated gain of this antenna, which is looped into a semicircle, is -6 dBi. This antenna is intended for implantation in the eye of a rabbit or human and is too large for very small animal studies. A receive antenna that is suitably small for implantation in mice or for devices arrayed in a muscle for clinical applications such as prosthetic control would have to be much smaller than this and would likely fall into the range of what is described as electrically small antennas. An electrically small antenna is one in which the largest dimension (such as the length of a monopole antenna or the diameter of a loop antenna) is less than $\lambda/10$. This leads to a crucial point, which is that any antenna small enough to suit the application of chronic data acquisition in mice will likely be an electrically small antenna. This might be avoided by increasing the operating frequency to tens or hundreds of GHz (the wavelength being only 3 mm at 100 GHz). However, it is expected that power loss from tissue attenuation will be even more dramatic at these higher frequencies and will negate the benefits of using a half wavelength or quarter wavelength antenna.

The narrowing of the antenna solution space to electrically small antennas is a practical and realistic constraint. It also allows for a more concrete discussion of

expected antenna gain and matching network efficiency, which will be assistive in developing a realistic power link budget analysis and drawing conclusions about the suitability of this WPT strategy. The critical inefficiency of using an electrically small antenna is not the gain of the antenna itself. In fact, a standard half-wave dipole has a known gain of 2.15 dBi while a short dipole with a length of λ/10 can have a gain of 1.77 dBi [120]. This gain assumes that the input impedance is well matched to the RF source impedance (typically 50 Ω). However, implementing this matching network in electrically small antennas comes at a price. What makes the electrically small antenna less efficient in practice is the high reactance component of its input impedance, which necessitates large-value reactive components (inductors and capacitors) in the matching network. These components—especially inductors—are accompanied by significant resistive losses, which can drastically decrease the efficiency of the matching network (e_{mn}) [120, 121]. An approximation of power loss through a matching network for electrically small antennas which accounts for practical and finite quality factors of inductors is derived in [120] with a result of around -20 dB. This number will serve as a sufficient approximation for e_{mn} in the link budget analysis.

It is possible that the overall PTE through an electrically small antenna might be improved by designing it to have a higher directivity, which is a measure of the power density in the direction of strongest radiation. However this reduces the antenna's effective area by focusing the emitted energy into a smaller range of space. Recall from Section 1.3.2 that the dependence on precise source and receiver alignment is one of the key issues with inductive power coupling, making it an impractical solution for

power transfer to freely behaving animals. For the same reason it is not desirable to give the receiving antenna high directivity because changes in the animal's posture and facing would dramatically change the PTE and lead to frequent shutdown of the implanted device. For the purposes of the link budget analysis, it is assumed that the receive antenna is isotropic; that is its gain is uniform and 0 dB in all directions. It should be noted that an isotropic antenna is a hypothetical antenna. It is modeled as a point source for electromagnetic waves and has no physical equivalent [116]. However, it can be used in this link budget analysis for a best case scenario calculation since a receive antenna with no directionality would be optimal for this application.

The assumption that the receive antenna gain is equal to 0 dB and has a matching network loss of 20dB may be combined with (2.4) and (2.8) to calculate a realistic approximation of the power link budget for a device embedded in tissue. The result will depend on the type of tissue and depth at which the receive antenna is implanted. It is expected that the implant will be placed subcutaneously in rodents as their skin is loose, which can provide plenty of space that is also far from the vital organs. Even mice weighing 15 g can accommodate a device as long as 12 mm when placed subcutaneously [122]. For clinical applications it is possible that the device may be placed either subcutaneously or intramuscularly. For comparison a subcutaneous implantation is assumed, so the thickness of human versus rodent skin must be considered. The average skin thickness for humans is 2.58 ± 0.07 mm whereas the average thickness of rat skin (hairless) is 0.86 ± 0.06 mm and the average thickness of mouse skin (hairless) is 0.41 ± 0.02 mm [123]. The conductance of skin, which is needed

to calculate the skin depth used in (2.4), is acquired from [115]. In the absence of data for rodent skin conductance, the measured human skin conductance as a function of frequency is used for all calculations. The resulting power link budget for a device with a rectifier efficiency of 20%, 40%, and 60% is given in Figure 2.1.

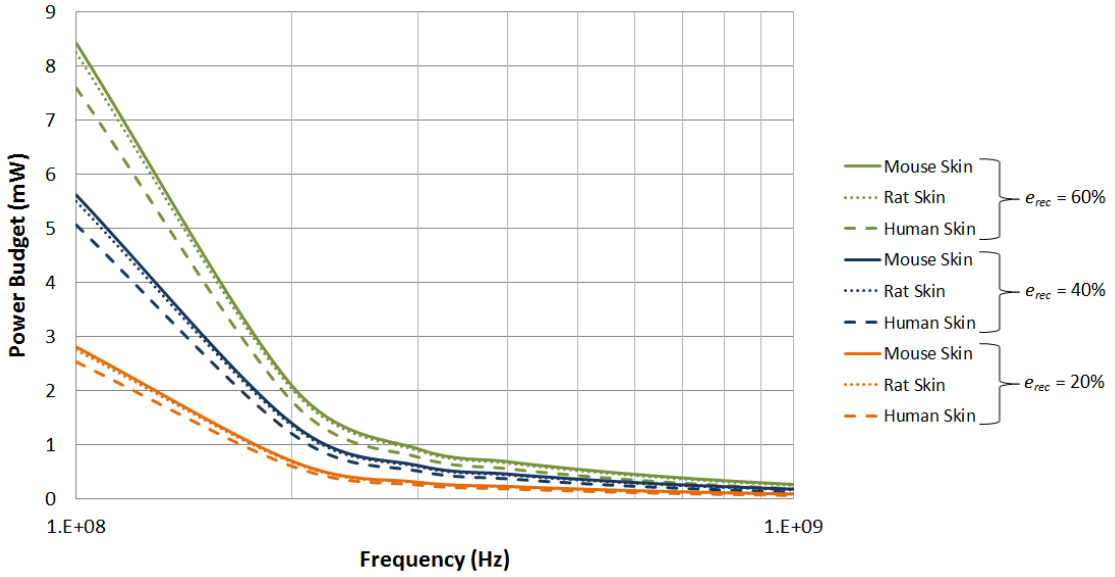

Figure 2.1 Calculated maximum power coupled through far-field RF link to a device implanted subcutaneously as a function of the electromagnetic field source frequency. Power budget given for human skin (thickness = 2.58 mm), rat skin (thickness = 0.86 mm), and mouse skin (thickness = 0.41 mm) at rectifier efficiencies of 20% (green), 40% (blue), and 60% (orange). The frequency dependent maximum permissible exposure (MPE) limit is imposed on the skin surface boundary. Receive antenna is treated as an electrically small isotropic antenna with a matching network loss of 20 dB.

Recall that the boundary condition used for this theoretical link budget analysis is the MPE limit at each operating frequency. This limit is calculated as an average over 30 minutes, which means that the RF field exposure may exceed this limit for short periods of time. That isn't to say that the power flux density at the surface of the skin can be

increased unboundedly with shorter and shorter periods of exposure. There is still an absolute maximum power flux density limit as a result of the SAR safety threshold given by (2.7). Figure 2.2 shows the absolute maximum power flux density limit for skin resulting from the SAR safety threshold as a function of field frequency.

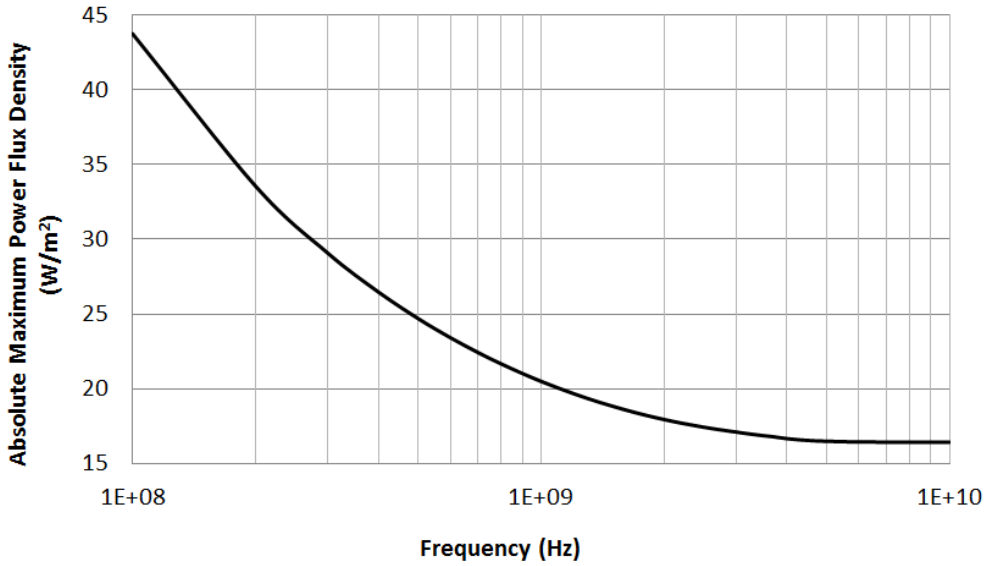

Figure 2.2 Absolute maximum power flux density that may be present in mammalian skin tissue based on peak spatial SAR constraint for energy absorption from electromagnetic fields. Tissue mass is assumed to be 1.04 g/cm^3 and the dielectric properties of the absorbing medium are based on data from human skin tissue.

Figure 2.1 illustrates the severe power losses that may be sustained in the far-field link budget at higher and higher frequencies. Regardless of the species, receive power drops to below 0.25 mW at a frequency of 1 GHz through skin. The power budget is further reduced in all cases to below 0.1 mW at 2.4 GHz and below 0.01 mW at 5.8 GHz. At the 915 MHz ISM band, the wavelength is still long enough (32.8 cm) that only an

electrically small antenna would be feasible in an implant suitable for mice. It is worth nothing that as the frequency continues to increase, resonant antenna design becomes more realistic and matching network losses might decrease. However, the exponential decrease in RF field power through tissue with the increasing frequency means that even a quarter-wavelength antenna at 5.8 GHz (which would have a length of approximately 13 mm) with no matching network losses would only yield a power budget of up to 1 mW. This estimate is calculated under the condition of subcutaneous implantation in a mouse and assumes a rectifier efficiency of 60%.

At this point it is reasonable to take the theoretically derived power link budget and compare it to the power demands of existing wireless biomedical sensors. Table 2.1 offers a list of active devices that have been created for the purpose of wireless biopotential acquisition. These devices are designed for a variety of purposes and each has been developed under a unique set of constraints, which can make fair comparisons difficult. However, there are some fundamental building blocks of a bioelectric sensor, including an amplifier stage for signal conditioning, analog to digital converter (ADC), microprocessor or other digital logic circuit to mediate device tasks, and a transmitter for data telemetry.

The type of bioelectric signal targeted by each system is listed along with the number of channels and sampling rate per channel that each solution offers. Total sampling rate (the product of the number of channels and the sampling rate per channel) is included since higher data rates increase the power consumption of RF transmitters, which typically draw more current than any other functional block of active wireless

sensors. The list shown in Table 2.1 is not exhaustive, but it does give a sense for the range of power requirements needed to run electronics that can perform the essential tasks of conditioning, sampling, and transmitting bioelectric data.

Table 2.1 Comparison of power consumption for active biomedical sensors configured for wireless data telemetry. Number of channels and sampling rate per channel are reported as these strongly affect the power consumption.

Publication	***Target Signal***	***Number of Channels***	***Sampling Rate Per Channel (kHz)***	***Total Power Consumption (mW)***
Chow et al. [65]	Neural (general)	32	30	8.8*
Chestek et al. [124]	Neural (general)	1	0.625	30
Harrison et al. [125]	EEG	1**	15	13.5
Szuts et al. [126]	EEG	64	20	645
Fan et al. [127]	EEG	16	30	27.8
Zhang et al. [128]	EEG	1†	0.1	>77.2
Chang et al.[129]	ECoG	16	12.5	27.6
Charvet et al. [130]	ECoG	32	1	100
Parramon et al. [131]	EMG	2	14.6	22.5
Prabhav et al. [132]	EMG	1	1	33
Russell et al. [133]	EKG	1	2	16
Hsieh et al. [134]	Bioelectric (general)	7	0.22††	12

*This system is solely a transmitter for biomedical sensors and does not include the additional power consumption contribution of signal amplifiers or ADC
**Can select from one of an array of 100 electrodes
† This device also includes three stimulating channels. Reported power consumption reflects transceiver and microcontroller contributions only.
††Average sampling rate per channel is given, however each channel's sampling rate is configured for a different signal.

An evaluation of the range of reported power requirements for existing wireless bioelectric sensors shown in Table 2.1 suggests that these would not be compatible with a far-field WPT link. The theoretical link budget analysis summarized in Figure 2.1 indicates that the only way to couple adequate levels of power (at least 8 mW) would be

reducing the frequency to below 100 MHz. It seems possible based on the positive correlation between power consumption and number of recording channels that a system having only one recording channel would have a lower power consumption and might be amenable to WPT in the frequency range shown in Figure 2.1. However, the theoretical link budget is calculated under the assumption that the receive antenna is electrically small with a characteristic length of $\lambda/10$. Even at 434 MHz—the lowest ISM band considered—a $\lambda/10$ characteristic length equates to 7 cm. Considering that the body length (from nose to base of tail) of a normal, healthy mouse is 7.5—10 cm [135], this would still be too large for implantation.

This analysis covers far-field power transfer to subcutaneous implants in rodents and humans. One can imagine that the low PTEs observed under these conditions will only get worse with deeper implantations, such as those envisioned for the clinical application for upper-limb amputees discussed in Section 1.3. In order to quantify the expected far-field RF power transfer through multiple tissue layers, a more complex model will need to be constructed. The evaluation of energy absorption and reflection between disparate tissues can rapidly become a computationally intensive endeavor, so a numerical solver is employed in proceeding section in order to model and simulate the electromagnetic fields in a more complex model—a human chest wall. The numerical results will also serve to validate the prior theoretical approximation and allow for a decision to be made as to whether or not far-field RF power transfer is a feasible WPT strategy for either of the desired applications of this work.

2.4 FEM Analysis of RF Electromagnetic Fields in Biological Tissue

The link budget analysis performed in Section 2.3 is a good theoretical approximation but is limited in its application by some of the assumptions imposed. For instances of subcutaneous power transfer where the tissue boundary may be approximated by a single homogenous medium, the theoretical link budget is sufficient. However, the human clinical application of this wireless recording device, which is discussed in Section 1.3, is more complex owing to the variable depth of implantation and multiple tissue mediums through which the electromagnetic energy will pass. As a result the analysis of the WPT link for this application requires a more sophisticated model that accounts for the disparate dielectric properties of different types of tissues as well as the energy reflections which take place at the boundaries between the different tissues. A 3-dimensional tissue model for the human chest and an electromagnetic field source are simulated in this section using finite element method (FEM) software. The simulation is performed in ANSYS High Frequency Structure Simulator (HFSS®) 13.0 and will serve to corroborate the conclusions from the theoretical analysis and illustrate the power dispersion in a more complex tissue model.

A field frequency of 2.4 GHz is used to illustrate one construction of the model and iteration of the simulation. The simulation environment is set up using a half-wave (6.25 cm for an operating frequency of 2.4 GHz), center-fed dipole antenna placed parallel to the z-axis and a three-layered body model. The three layers of the model are skin, adipose, and muscle; each is assigned a thickness and dielectric properties based on known characteristics of tissue in the human chest wall [115, 136, 137]. The tissue

model is placed one wavelength along the y-axis from the center of the antenna so that the model resided in the far-field region of the electromagnetic field. A cross-sectional view of the model in the simulation environment is shown in Figure 2.3.

.The first simulation performed serves to check that the model has been set up correctly. In Section 2.3 the minimum antenna-tissue separation for an EIRP of 1 W (resulting from an input power of 1 W to an isotropic antenna with a matching network efficiency of 100%) is calculated using (2.2) to be 8.92 cm. Since the antenna-tissue separation in the 2.4 GHz field simulation is 12.5 cm, it is expected that the power flux density in the tissue model will fall below the MPE limit. In order to check that this is true, the 1 W EIRP powering condition will be replicated in the simulation environment and the resulting peak power flux density at the surface of the tissue model will be measured and compared to the MPE limit.

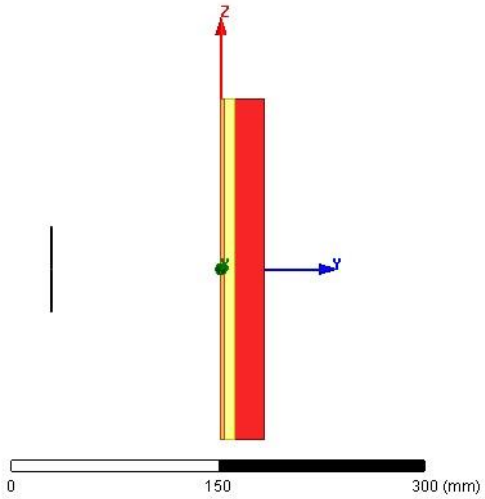

Figure 2.3 Simulation environment for a three-layer tissue model of the human chest in the far-field of a radiating antenna. Tissue model cross section is shown here from the perspective of the positive x-axis. Dipole-tissue separation is one wavelength, λ (12.5 cm at 2.4GHz). Skin layer thickness is 0.2 cm, adipose layer thickness is 0.84 cm, and muscle layer thickness is 2.16 cm. © 2013 IEEE.

The antenna depicted in Figure 2.3 radiates uniformly in the xy-plane in free space. However, its radiation pattern changes when objects are introduced into its electromagnetic field. In order to ensure a 1 W EIRP in the direction of the tissue (along the y-axis), the radiation pattern of the antenna must be known. This is measured in HFSS® and is shown in Figure 2.4. The tissue model is constructed such that its length in the z- and x-directions are both twice the antenna-tissue separation. This places the tissue model between -45° and 45° on the antenna's radiation plot. The peak gain in the direction of the tissue is -2.3029 dB and lies at $\varphi = 90°$ and $\theta = 90°$ (in the direction of the y-axis). Continuing with the assumption that the matching network efficiency for the

radiating antenna is 100%, the power input to the antenna can be set to 1.7 W to compensate for its less-than-unity gain, which leads to a peak EIRP of 1 W.

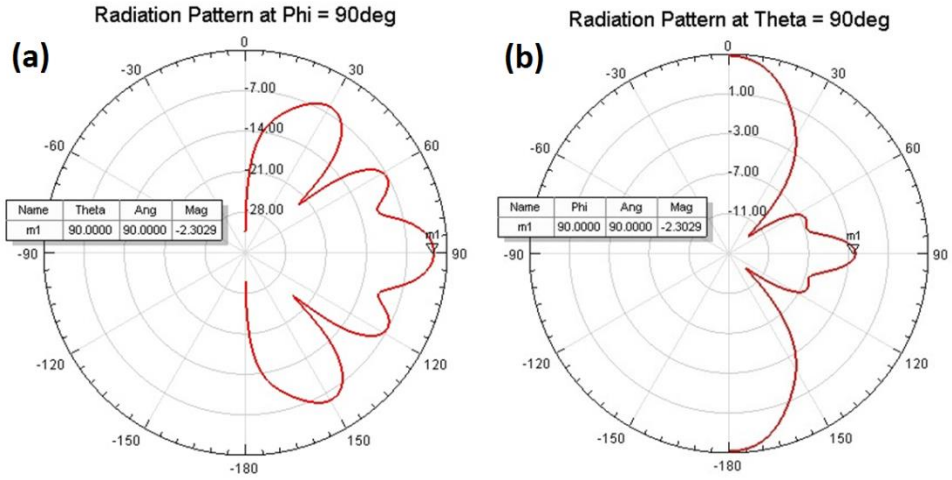

Figure 2.4 Radiation pattern of a half-wave dipole in the HFSS® simulation environment with a 3-layer tissue model at 2.4 GHz when (a) $\phi = 90°$ and θ is swept from 0° to 180° and (b) $\theta = 90°$ and ϕ is swept from 0° to 180°. Due to its dimensions and separation from the antenna, the tissue lies within the region defined by $45° \leq \phi \leq 135°$ and $45° \leq \theta \leq 135°$. The local maximum gain within this angular region is -2.3029 dB. © 2013 IEEE.

Oftentimes the resonance of an antenna will shift when objects are introduced to or moved within its electromagnetic field. For this reason the S11 reflection coefficient of the dipole antenna was measured in HFSS®, yielding a bandwidth of 2.06—2.48 GHz. This means the dipole antenna is still an effective radiator for a 2.4 GHz RF source in the simulation environment even with the effects of the tissue model in the electromagnetic field.

The distribution of the power flux density incident on the tissue can be imaged by plotting the real part of the Poynting vector at the air-tissue boundary plane. It is

expected that the peak incident power flux density will be less than the FCC limit (10 W/m^2). The actual simulated maximum is 8.11 W/m^2, which is (as expected) within the safe operating space for RF exposure. One of the benefits of using a high frequency field simulator is that is can easily and accurately model the reflection of energy at a boundary between two materials having unique dielectric properties. The power flux density at the air-tissue boundary in the skin (after reflection on the skin surface) is shown in Figure 2.5. The maximum power flux density that passes through the skin is 6.56 W/m^2.

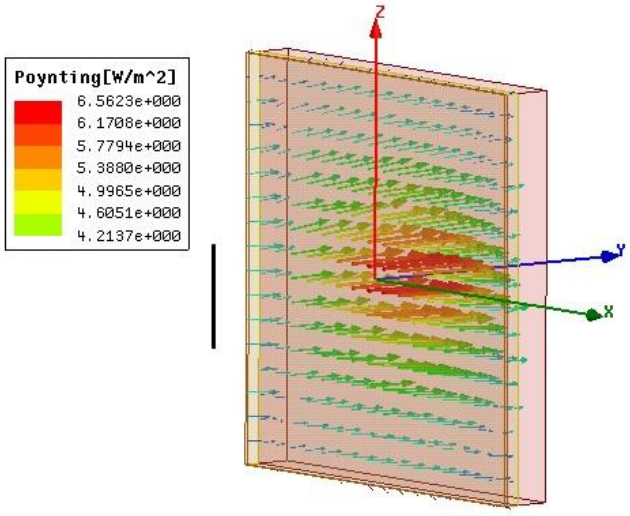

Figure 2.5 Poynting vector field (directional power flux density) in tissue at the air-tissue boundary with 1 W EIRP output from a half-wave dipole radiating at a frequency of 2.4 GHz. The maximum power flux density is 6.56 W/m^2, which occurs at the surface of the skin on the y-axis. This is expected since the maximum EIRP condition is imposed along the y-axis. © 2013 IEEE.

Further validation of the virtual model may be done by examining the maximum power absorbed by 1 g of tissue and demonstrating that the SAR limits are not exceeded. This would corroborate the safe power guidelines established by the theoretical analysis. The maximum SAR evaluated over 1 g of tissue is evaluated using the HFSS® field calculator. This is done by first identifying the magnitude and coordinates of the peak local SAR. Unsurprising, this maximum is found to occur at the origin of the axes on the surface of the skin where the directional gain of the antenna is largest. The following equation is used to calculate the total energy absorbed by a 1 g cube of tissue per FCC specifications:

$$SAR_{peak} = \frac{P_{in} - P_{out}}{m} \tag{2.9}$$

where P_{in} is the total power entering a 1 g cube of tissue having mass, m, and P_{out} is the total powering leaving the same cube. The net power through a single face of the cube, P_{net}, can be found by taking the dot product of the Poynting vector, S, and the unit vector normal to the face and integrating over the area of the cube face, F:

$$P_{net} = \iint_F (S \cdot \hat{n})\, dF \tag{2.10}$$

A 1 g cube of tissue with a side length of a is defined in the simulation environment using six square plane. Each face of the cube is assigned a number as follows: face 1 (F_1) lies on the xz-plane and transects the y-axis at the origin, face 2 (F_2) transects the x-axis at x = $a/2$, face 3 (F_3) transects the y-axis at y = a, face 4 (F_4) transects the x-axis at x = $a/2$, face 5 (F_5) transects the z-axis at z = $a/2$, and face 6 (F_6) transects the z-axis at z = -$a/2$. The total power absorbed by the tissue in this cube, P_{tot}, would then equate to the following:

$$P_{tot} = P_{net,F_1} + P_{net,F_4} + P_{net,F_6} - P_{net,F_2} - P_{net,F_3} - P_{net,F_5} \quad (2.11)$$

The field calculator in HFSS® can be used to calculate each of the net power flux terms in (2.11). The total amount of power absorbed by this cube can then be determined by substituting the numerator of (2.9) with the sum of the net power flux terms, P_{tot}. This is evaluated in the simulation environment with a field frequency of 2.4 GHz, resulting in a peak absorbed power of 0.36 W/kg in 1 g of tissue. This is much less than the peak spatial SAR limit (1.6 W/kg over 1g of tissue), which further supports the compatibility of the tissue behavior in the simulated environment with expected theoretical results. However, the power flux density in skin at the air-tissue boundary necessary to reach the FCC's peak spatial SAR limit in the simulated tissue model calculated is 29.14 W/m^2, which is greater than the 17.76 W/m^2 predicted by the theoretical analysis. This discrepancy between the analytic and numerical peak local SAR calculations can be

attributed to the observance of the reflection phenomenon as well as the different tissue dielectric properties in the HFSS® environment.

A comparison can now be made between the power attenuation within the chest wall at different electromagnetic field frequencies using the validated tissue model in HFSS®. The model is adapted for operation at 915 MHz and, subsequently, 5.8 GHz. The powering conditions for the simulation at each frequency are made uniform by equating the power flux density at the surface of the skin to the time-averaged MPE safety limit at each operating frequency. The simulated power flux density incident on the implanted device at various implant depths are shown in Table 2.2. Also contained in Table 2.2 are estimates of the receiving device's power budget for each implant depth and field frequency. These estimates are calculated using (2.9) under the assumption that the receive antenna radiates isotropically and has a matching network loss of 20 dB. The results are given for three RF-to-DC conversion circuit (rectifier) efficiencies so that the likely power budgets for different scenarios can be easily compared.

Table 2.2 Power flux density and estimated implant power budget at four implant depths within an HFSS® model of a human chest at three ISM bands: 915MHz, 2.4GHz, and 5.8GHz. In all cases the time-averaged MPE safety limit is imposed on the surface of the skin to create conditions for maximum allowable power transfer. Usable power is estimated under the assumptions that there are no losses from the receive antenna (gain of 0 dB) and matching network loss is -20 dB. © 2013 IEEE.

Powering Frequency	***Implant Location***	***Average Power Flux Density at Implant (W/m^2)***	***Average Usable Power (μW) Given e_{rec} =***		
			20%	***40%***	***60%***
915 MHz	Between skin and adipose	4.93	84.4	169	253
	Between adipose and muscle	4.64	79.4	159	238
	1 cm into muscle	2.37	40.6	81.2	123
	2 cm into muscle	1.21	20.7	41.4	62.1
2.4 GHz	Between skin and adipose	4.38	10.9	21.8	32.7
	Between adipose and muscle	3.16	7.86	15.7	23.6
	1 cm into muscle	1.57	3.90	7.80	11.70
	2 cm into muscle	0.561	1.40	2.80	4.20
5.8 GHz	Between skin and adipose	4.88	2.08	4.16	6.24
	Between adipose and muscle	2.20	0.936	1.872	2.81
	1 cm into muscle	0.129	0.0549	0.110	0.165
	2 cm into muscle	0.0150	6.38e-3	1.28e-2	1.91e-2

The trend in power loss observed in Table 2.2 is closely correlated with the results of the theoretical analysis in Section 2.3. The relatively low quantities of power that may be expected from a far-field WPT link compared to the range of power requirements for wireless bioelectric sensors reported in Table 2.1 suggest that sourcing power solely from radiative electromagnetic fields would be insufficient to continuously operate an active implantable sensor. It is possible that a sensor having a lower average

power consumption than those given in Table 2.1 could be powered using a far-field RF WPT link. This might be achieved by implementing power cycling of the entire device or just the transmitter, which typically consumes the most power. For example, a single channel recording device with a desired sampling rate of 5 kHz could be turned on once every 200 µs to sample and transmit the desired signal and then turned off for the rest of the time. During the off-phase, energy could be accumulated and stored in a capacitor for use during the next on-phase. If the sampling and transmission of each data point could be achieved in less than 2µs, then the duty cycle of the on-phase could be reduced to 1%--conceivably reducing the average power consumption of the device by a factor of 100. Even more strategic solutions might be implemented such as utilizing a low power mode to sample and store multiple data points in a buffer and then transmitting them all at the same time. This would reduce the frequency of transmitter startup and shutdown, which comes with some power consumption overhead. The ability to utilize far-field WPT for a wireless implantable sensor would, resultantly, be contingent upon the design of a system that can implement sufficiently small duty cycles to reduce average power consumption into the range shown in Table 2.2

2.5 Thermal Safety of Active Implantable Systems

Active implantable devices dissipate heat into surrounding tissue. Sustained temperature increases can permanently damage or otherwise affect tissue proximate to the device. The relationship between temperature, time-at-temperature, and extent of cell death/tissue damage is complex and will depend on the type of biological matter

surrounding the heat source [138, 139]. The intended location for implantation of the wirelessly powered recording device is either subcutaneous or intramuscular, so safe thresholds for thermal exposure of skin, muscle, and adipose are considered here. Empirical data for these thresholds exist but are difficult to generalize. However, the following heuristics might be used: tissue temperature should not exceed 43 °C for greater than 10 min. and a tissue temperature of less than 39 °C is considered safe for any length of time [140].

Evaluation of local temperature spikes due to heat diffusion from an active implantable device is performed by dispersing various quantities of energy in 16.4 mm^3 samples of bovine muscle. This is achieved by supplying a range of voltages across a 1 kΩ resistor. Given Ohm's Law and power dissipation through a resistive load being the product of current and differential voltage, the voltage drop across a resistance, *R*, necessary to consume a known power level, *P,* can be equated to $\sqrt{PR}$. For example, a desired power dissipation of 10 mW is achieved by applying 3.16 V across the 1 kΩ resistor. The resistor is sealed within a medical epoxy package having dimensions of 11.85 mm x 5.50 mm x 3.95 mm. These dimensions were selected such that they would resemble the form factors of previously developed implantable myoelectric sensors [141, 142], which have been implanted into muscles at depths up to 1 cm. All muscle samples are maintained at body temperature (37 °C) throughout the experiment using an incubator. The device is continuously powered for approximately 15 min. until the temperature adjacent to the device reaches a steady state. This experiment is repeated

three times (n = 3) at four different power levels: 10, 20, 30, and 40 mW. Tissue temperature adjacent to the device within the muscle is recorded in each trial using a thermocouple paired with LabVIEW for data acquisition. The increase in local tissue temperature due device heating can be seen in Figure 2.6.

This experiment is intended to estimate the temperature change in tissue proximate to a device which is drawing current and expelling heat, but a moment should be taken to acknowledge the limitations of *in vitro* thermal measurements. Bioheat transfer is a complex phenomenon—the complete characterization of which includes irregular boundary conditions, varying thermal characteristics of tissues (density, specific heat, thermal conductivity, etc.), and complex geometries of the environment. Additional mechanisms that play a role in thermal regulation include blood perfusion and metabolic heat production: neither of which is present during *in vitro* analysis [143]. However, the local temperature measurements in bovine muscle samples give a first order approximation of temperature changes that may be expected as a result of thermal diffusion. The results of this experiment indicate that it would take a power consumption of 40 mW in order to elevate the local temperature in muscle by more than 1 °C. Since 40 mW far exceeds the amount of power than can be safely coupled through a far-field wireless link—regardless of the depth of implantation—these results suggest that unsafe temperature elevation in tissues from thermal diffusion would not be the primary safety concern in devices that employ far-field RF power transfer.

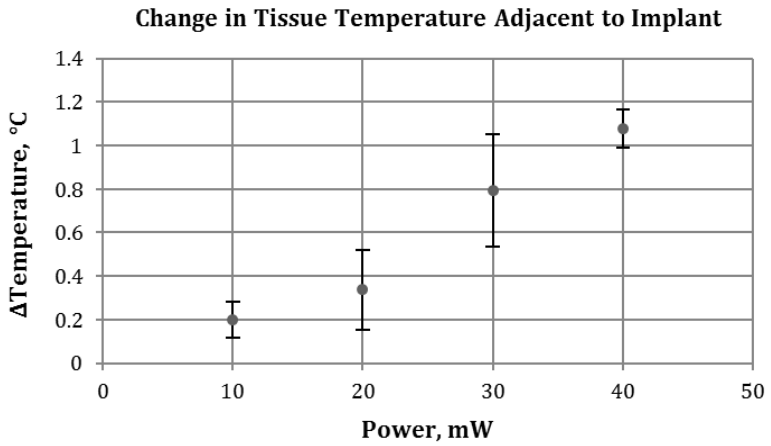

Figure 2.6 Temperature increase in bovine muscle measured immediately adjacent to a device consuming between 10 and 40 mW of power. Three samples (n = 3) are tested at each power amplitude. Local temperature changes are measured with respect to a normal body temperature baseline (37 °C) using a thermocouple. © 2013 IEEE.

2.6 Conclusion

The relative potential for health and safety hazards suggested by the results of the RF exposure and thermal diffusion analyses suggest that the effects of RF exposure — both thermal and non-thermal—is a greater concern than local temperature elevation from the thermal discharge of microelectronics. Prior to drawing any conclusion about the feasibility of far-field RF power transfer for implanted bioelectric sensors, it is crucial to note that the theoretical and numerical analyses contained in this chapter are all based on the presumption that MPE limits have been reached. This is a way of examining the best case scenario for the WPT link. In reality, a freely behaving animal will rarely be in the optimal location where MPE limits are reached, which only further diminishes the prospects of far-field RF power transfer for long-term monitoring of bioelectric activity in small animals.

However, as noted in Section 2.4, a significant reduction in the duty cycle of a sensor's on-phase could reduce the average power consumption to the point that the power link budget afforded by far-field RF power transfer might be sufficient—even when MPE limits are not reached. This solution would necessitate the design of a microelectronic system that achieves sufficiently low on-phase duty cycles of the transmitter while incorporating an effective power storage strategy. Without significant examination of the limitations of CMOS design, it is not certain that a system meeting these requirements is achievable. For this reason, alternative WPT strategies are sought for continuous power transfer to devices implanted in freely behaving animals.

It is also evident that far-field RF power transfer is not a feasible WPT strategy for the clinical application of this work. While it is certainly possible that MPE limits could be consistently applied in the controlled environment of an upper-limb prosthesis, the extremely low power budgets that can be expected—even under the condition that MPE limits are reached—for devices embedded 1 cm and 2 cm into muscle are orders of magnitude less than the power requirements of existing myoelectric sensors. This leads to the conclusion that an alternative WPT strategy is also needed for the purpose of delivering power to devices embedded deep in the muscles of amputees.

CHAPTER 3. THE MYONODE: AN IMPLANTABLE SINGLE-CHANNEL RECORDING DEVICE

3.1 Introduction

The material presented in this Chapter incorporates content from the journal article “Enhancing the Versatility of Wireless Biopotential Acquisition for Myoelectric Prosthetic Control” by R. A. Bercich, Z. Wang, H. Mei, L. H. Smith, K. L. Seburn, L. J. Hargrove, and P.P. Irazoqui, which has been accepted for publication in the Journal of Neural Engineering pending revisions. All procedures involving live animals are reviewed and approved by the Purdue Animal Care and Use Committee. Mice are obtained from The Jackson Laboratory (Bar Harbor, ME). All experiments involving human subjects are approved by the Northwestern University Institutional Review Board.

The practical limitations of near-field inductive coupling outlined in Section 1.3.2 and the extremely low far-field power link budget derived in Chapter 2 seem to suggest that neither inductive nor radiative power coupling is sufficient for continuous WPT to devices implanted in freely behaving animals. However, recent advancements in the area of MRC [144, 145] have led to improved PTEs in inductive links that are poorly coupled (e.g. disparate in size, misaligned, or far from one another). This methodology utilizes bandpass filter theory to implement optimal impedance matching conditions, resulting in precisely tuned inductive systems in which the maximum attainable PTE is

realized. This has been previously suggested as a viable option for power transfer in long-term animal monitoring with both stationary [146, 147] and non-stationary [148] external coils

Implementation of the MRC methodology by Henry Mei, a graduate research assistant in the Center for Implantable Devices at Purdue University, led to the demonstrated ability of an MRC link to sufficiently couple tens of mW of power to a coil having a diameter of 1.2 cm using an external coil with a diameter of 13 cm outputting 1 W of power. This corresponds to a PTE in the range of 1-5% rather than < 0.1%, which may be expected from far-field WPT per the link budget analysis performed in Section 2.3. The implication here is that MRC can enable levels of power transfer between two coils—having greatly disparate diameters—that would be sufficient to run many of the wireless bioelectric sensors described in the literature (see Table 2.1). The sufficient PTE of this particular pairing of coils (13 cm external coil and 1.2 cm receive coil) is demonstrated in free space with coil-to-coil distances up to 5 cm. Concerns about power attenuation in tissue are abated by the fact that MRC achieves energy transfer through magnetic fields, the power flux densities of which are largely unaffected by biological tissue.

The primary motivation for this work is to develop novel instrumentation for the study of neuromuscular disease mechanisms in freely behaving mice. Being only 13 cm in diameter and 5 cm in vertical range, the WPT environment made possible through the application of MRC methodology is not very large. However, it is sufficient for a mouse to ambulate normally and is compatible with a receive antenna that is appropriately

small for subcutaneous implantation in mice (1.2 cm), both of which enable a first pass at a fully wireless bioelectric sensor. The secondary motivation is to improve neural interfaces between muscle and upper-limb amputees. Since both of these aims entail some evaluation of muscle activity, the first microelectronics system is designed specifically for EMG acquisition and is given a simplified task set: to record and transmit one channel of data. This single-channel recording system specifically for fully wireless EMG acquisition is referred to as the Myonode

Two implementation of the Myonode are presented here: one using CMOS technology and the other using only commercial off-the-shelf circuits on a custom printed circuit board (PCB). The construction, bench top analysis, and applied *in vivo* performance of both designs are summarized in this chapter.

3.2 ASIC Implementation of the Myonode

The first implementation of the Myonode uses CMOS technology to create an application-specific integrated circuit (ASIC). This method affords the most flexibility and customizability since the designer may judiciously strip away unnecessary sources of current consumption to create a system that meets only the necessary functional requirements. Reduction of average power consumption (a direct corollary of current consumption) serves as one of the primary objectives for this ASIC as this lessens the burden on the WPT link, improving its robustness once the device implanted in an animal.

The necessary functional blocks for the Myonode's ASIC include an amplifier, ADC, RF transmitter, voltage regulators, and digital logic. Figure 3.1 shows a block diagram of the ASIC within the conceptual design of the full EMG recording device. The design and simulated performance of the EMG amplifier is described in Section 3.2.1. The remaining functional blocks of the ASIC are designed by other students from the Center for Implantable Devices at Purdue University. Specifically, the ADC and clock are designed by Hansraj Bhamra; the transmitter is designed by Oren Gall; the voltage regulators are designed by Ashir Shah; and the digital logic is designed by Jithin Joseph. CMOS design is done on the X-FAB 180 nm process using Cadence software. Bench top performance of the full system ASIC is summarized in Section 3.2.2. An analysis of prospects for the ASIC-based Myonode in the context of project needs is the subject of Section 3.2.3.

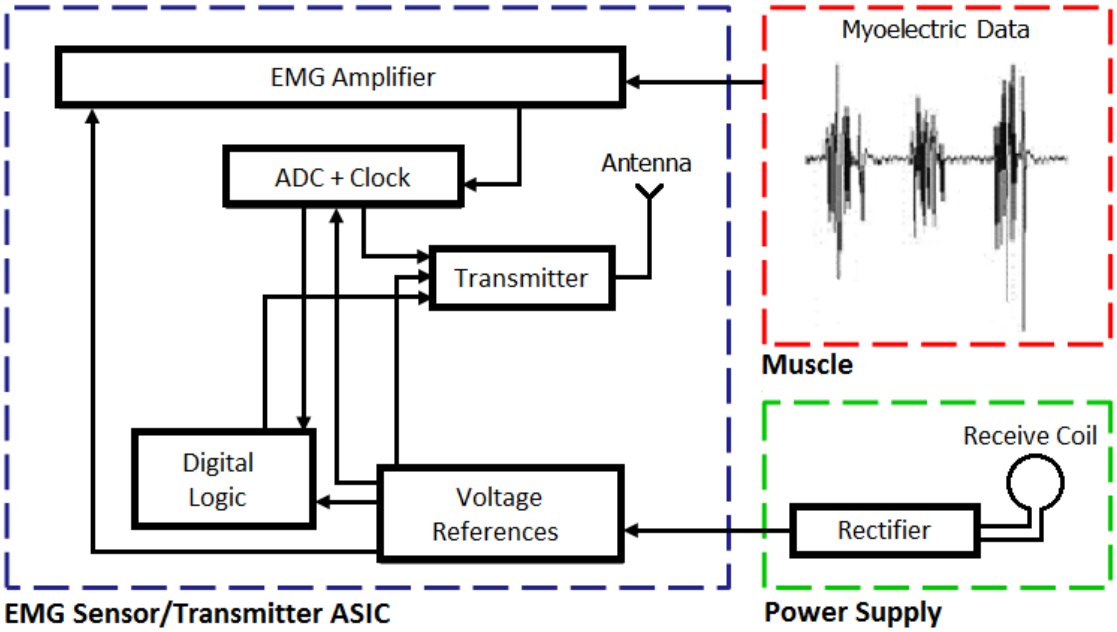

Figure 3.1 Conceptual block diagram of the full Myonode system including the EMG sensor and transmitter ASIC designed in CMOS (blue), power supply (green), and expected input signal (red).

3.2.1 EMG Amplifier Design in CMOS

The amplifier block of the EMG sensor ASIC is designed to be fully differential so that common mode noise sources are effectively rejected from the measured signal. Power line noise, for example, is a frequent artifact observed in bioelectric signals, so differential recording is common practice for both sEMG and imEMG [96, 149]. A folded cascode operational transconductance amplifier (OTA) topology [150] is selected owing to its relatively low power consumption and pervasive use in CMOS neural amplifiers within the literature [151-154]. The system is constructed such that it can run off of one supply voltage (1.8 V). In an effort to keep the first design simple and avoid integration of voltage inverters, the entire circuit operates in single supply mode, which sets the

ADC input voltage range between 0 and 1.8 V. This means that the ADC cannot read a negative voltage. Since differential EMG will exhibit both positive and negative amplitudes, both inputs need to be level-shifted to the mid-range voltage of the ADC (900 mV). This is implemented using common mode feedback within the differential amplifier circuit.

The peak-to-peak amplitude of measured EMG is very much dependent on the size of the muscle, strength of contraction, and electrode configuration. While it is true that a larger inter-electrode space will lead to a higher measured amplitude, signal attenuation through tissue will increasingly affect signal amplitude as separation between the source and the electrodes increases [155]. When measuring EMG on the surface of the skin, it is easy to implement larger inter-electrode spacing, but this will impact signal specificity, amplitude, and frequency content. For this reason it is important to consider the signal source and characteristics of the desired signal when selecting an electrode, placing electrodes, and configuring the gain response of the amplifier.

The maximum amplitude that may be expected from sEMG recorded with gel or metal dome electrodes is in the range of a few millivolts. Stimulus-evoked potentials, however, can reach tens of millivolts in peak-to-peak amplitude [149]. The Myonode is intended to collect both voluntary evoked potentials and stimulus-evoked potentials, so a low gain of 50 (34 dB) is the target for the bandpass region. It would be best under circumstances such as these—when different signals having amplitudes that differ by at least an order of magnitude—to implement adjustable gain. This feature is not included

in the ASIC in an attempt to keep the operating protocol simple on the first run. The intention being that, all other elements working properly, this ability may be integrated on subsequent systems. The resistive and capacitive elements which influence the gain of the amplifier also impact the bandpass cutoffs of the frequency response. A simulated gain of 34.7 dB, which is sufficiently close to the 34 dB specification, is achieved as a result of balancing desired gain and filtering specifications.

The majority of power in sEMG signals is contained in the frequency band from 10 to 500 Hz [149]. The high-pass cutoff used for sEMG ranges from 3 to 20 Hz as it's been suggested that some useful information can be obtained about motor unit firing patterns at frequencies as low as 3 Hz [156]. A low-pass cutoff of 500 Hz is commonly used for sEMG signals. However, biological tissue behaves like a low-pass filter [157-159], so the bandwidth of sEMG is lower in the frequency domain than EMG recorded from a group of fibers within a muscle or immediately adjacent to a single muscle fiber. For this reason the low-pass cutoff for imEMG is typically higher than that of sEMG: between 1 and 10 kHz [149]. Since the Myonode is intended for collection of both sEMG and imEMG, a bandpass region of 3 Hz to 1 kHz is the design specification.

A two-pole low-pass filter is implemented in the CMOS amplifier through feedback on the differential amplifier (first stage) and by passive low-pass filters in the second stage. Figure 3.2 shows a schematic of the full amplifier circuit with stages delineated. In contrast to ideal operational amplifiers, which have a theoretical output impedance of 0 Ω, folded cascode OTAs have a large output impedance. As a result, the feedback resistors (R1 and R2 in Figure 3.2) need to be very large (> 10 GΩ) in order to

achieve the desired low-pass cutoff. Given process variation in fabrication and the relationship between resistor length and value, it is impractical and unwise to use very large resistors or create large resistances by placing many smaller resistors in series. Some circuit designers have used transistors biased in the sub-threshold region to create large pseudoresistances [160, 161]. However, this requires additional biasing circuitry so, instead, a MOS-bipolar device described in [125] is implemented here to create a large pseudoresistance in place of R1 and R2 (see Figure 3.2).

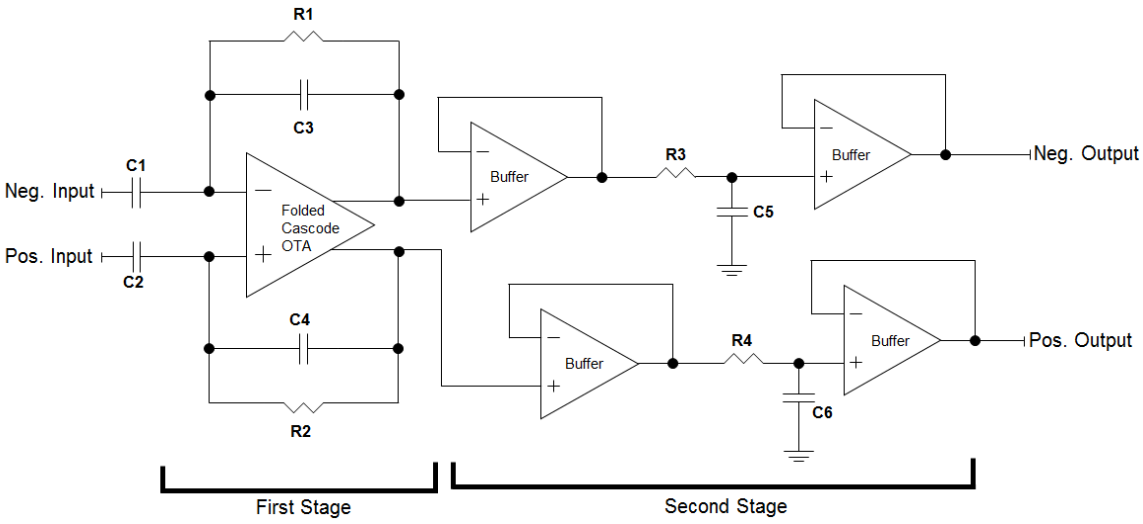

Figure 3.2 Circuit schematic of fully differential amplifier implemented on X-FAB 180 nm CMOS process. First stage is designed using a folded cascade operational transconductance amplifier (OTA) topology. Amplifier is AC coupled using front-end capacitors. Two-pole low-pass filter is implemented through feedback in the first stage and passive filtering in the second stage.

The second stage is buffered on both sides to isolate the passive filter and prevent shifting of the pole frequency due to influences of the first stage or loading from the ADC. The combined result of these filters is a simulated low-pass cutoff of 1.03

kHz, which is sufficiently close to the 1 kHz specification. The amplifier is AC coupled with capacitors C1 and C2 in order to prevent DC offsets or very low frequency signals—such as motion artifact—from reaching the amplifier inputs, which might cause saturation and railing at the outputs.

3.2.2 Full System ASIC Evaluation

The full system's functional protocol is clocked at 250kHz and has a data rate of 50 kbps. The ADC sampling rate is fixed at 5 kHz, which is selected based on the Nyquist frequency of the intended signal to avoid aliasing. The RF transmitter uses an on-off shift keying (OOK) protocol with a 4-bit start code and a 4-bit stop code to communicate each digitized 10-bit sample of EMG data. Figure 3.3(a) illustrates the full system ASIC layout in Cadence with the amplifier block highlighted in yellow. The final fabricated chip along with its physical dimensions is shown in Figure 3.3(b). Table 3.1 outlines the key performance specifications of the full system alongside the measured results for the same parameters from a sample system.

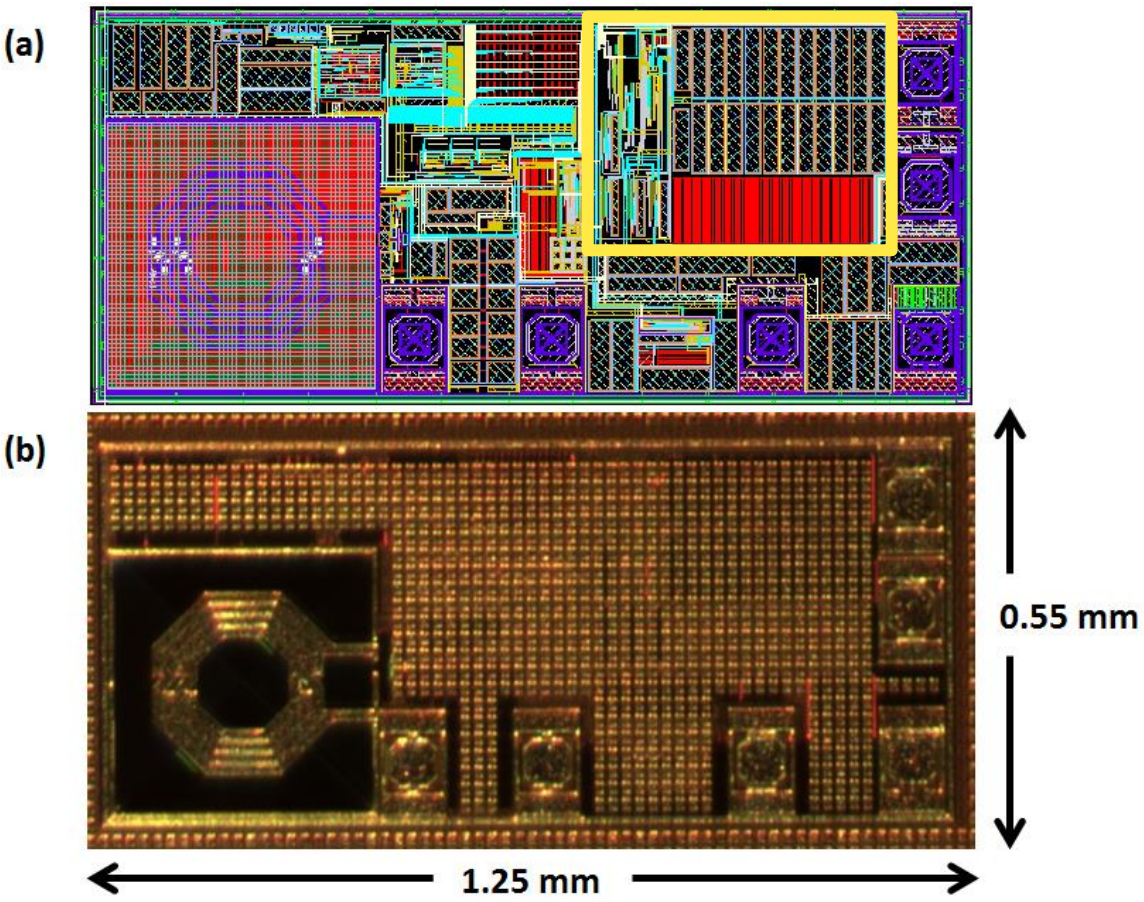

Figure 3.3 Full system ASIC designed in 180 nm CMOS process for single-channel EMG recording and telemetry with the amplifier circuit highlighted in yellow. (a) ASIC layout in Cadence software and (b) image of the fabricated full system chip with a measured footprint of 0.55 mm x 1.25 mm.

Table 3.1 Summary of simulated and measured parameters of the single-channel EMG recording and telemetry ASIC.

Parameter	***Simulated***	***Measured***	***Units***
Peak gain	34.7	36.2	dB
High-pass cutoff	2.32	32	Hz
Low-pass cutoff	1.03	1.45	kHz
ADC resolution	10	10	bits
Max. input amplitude	33	28	mV_{pp}
Sampling rate	5	5	kHz
Supply voltage	1.8	1.8	V
Power consumption	0.67	1	mW
Transmitter Frequency	2.4	2.46	GHz

The measured results shown in Table 3.1, which represent the performance of a sample Myonode ASIC indicate that this chip is able to perform the assigned task set of amplifying, filtering, sampling, and transmitting EMG. It may be noted that some parameters such as filter cutoff frequency have drifted—possibly as a result of process variation. Two clear advantages of this ASIC should be highlighted: first, the low power consumption relative to other bioelectric sensors (see table 2.1) and, second, the small footprint, which is amenable to subcutaneous implantation in very small animals.

This ASIC is used for *in* vivo EMG acquisition in an anesthetized mouse in parallel with a commercial preamplifier so that the measured signal of both instruments may be compared. The experimental procedure begins with blunt dissection to the sciatic nerve of a mouse. A two-contact platinum iridium cuff electrode is placed around the sciatic nerve and two needle electrodes are inserted into the biceps femoris muscle on the

ipsilateral side such that the inter-electrode spacing is 5 mm. Then a stimulus current is applied to the sciatic nerve through the cuff electrode and the evoked CMAP is recorded from the muscle. The stimulus current amplitude is gradually increased—recruiting more axons and their innervated muscle fibers—until the amplitude of the CMAP response stops increasing. This yields a maximum CMAP which is congruous with published results [23]. The same maximum CMAP recorded from both a commercial preamplifier (P511, GRASS Technologies) and the Myonode ASIC are pictured in Figure 3.4.

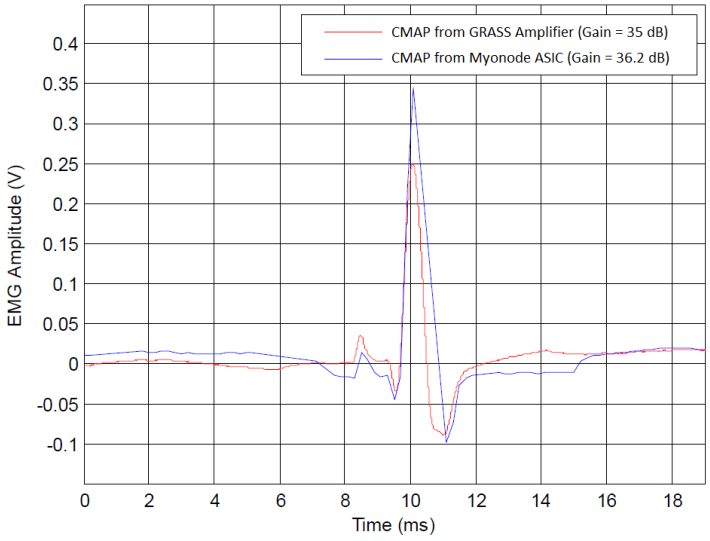

Figure 3.4 Compound motor action potential (CMAP) recorded acutely in a wild-type mouse using needle electrodes with an inter-electrode spacing of 5 mm. The same CMAP is recorded from the biceps femoris muscle of a mouse using the Myoode ASIC (blue) and a neural preamplifier (P511, GRASS Technologies) with the gain adjusted to 35 dB (red).

During this experiment the Myonode ASIC is powered using a DC voltage supply. The closely matched waveforms measured by the Myonode ASIC and a standard bench top apparatus shown in Figure 3.4 are a promising outcome for the ASIC-based system. This might encourage the next logical step to be taken: integrate the Myonode ASIC with a rectifier and coils designed for MRC power transfer so that the system may be wirelessly powered. However, there are significant functional and practical impediments to using this ASIC in chronic animal studies or for clinical neural interfaces for upper-limb amputees. An evaluation of these obstacles as well as possible solutions is conferred in Section 3.2.3.

3.2.3 Limitations of ASIC-Based System

One of the most critical limitations of the ASIC-based Myonode is the extremely low yield of working ASICs (less than 5%) from the fabricated wafer. This is a significant practical concern given the time needed to test each system, which is done using a probe station owing to the very small size of the input and output pads. Additionally, the ASIC must be adjoined to a rectifier and some implement for wireless power coupling before the system can operate in a WPT environment. This has the advantage of modularity but increases complexity in an already delicate and miniature build process.

Neither of these obstacles is necessarily a showstopper. However, the ultimate limitation is that the ASIC is one-trick pony without any flexibility in operation or performance. This makes the effort and expense of putting together even a small quantity of devices that could be implanted in animals fall out of balance with the utility

of the end-product. Specifically, the gain, bandwidth, sampling rate, and telemetry cycle of the ASIC—all of which are fixed—mean that a different system would need to be designed for each signal of interest.

Alternatively, it is possible that some flexibility might be built into the ASIC through features like programmable gain, tunable filters, and flash memory for reprograming the device's functional protocol. These are highly advanced elements, though; which means they require large amounts of time and expertise to implement. Not to mention the three- to four-month lead-times associated with fabrication of CMOS ICs. But perhaps the most compelling reason to avoid building such a complex system in CMOS is the fact that much of the effort is put into building circuit elements that may be thought of as "overhead"—that is, a replication of circuits that already exist and are available off-the-shelf. These commercial ICs are designed by experts for a variety of general and niche applications Moreover, the natural progression towards miniaturization in electronic technology means that most ICs come in very small form factors. Using only commercial ICs would allow a system to be built up from relatively small—in both function and size—components while leveraging the availability of sophisticated and reliable circuits. This has the added benefit of being replicable by other investigators interested in building and using the tool rather than negotiating the use of a proprietary circuit, which is better for the purposes of knowledge sharing in the scientific community.

This is not to say that a final, polished design wouldn't be best implemented in CMOS. However, given the developmental state of the project and the fact that the

engineering design process is iterative in nature, it is wisest to work with modular and easily integrated parts for quick prototyping and testing. For this reason device design in CMOS is deferred and the remainder of this work is focused on the development of miniature microelectronics systems for fully wireless bioelectric data acquisition that is built using only commercially available, off-the-shelf components.

3.3 Custom PCB Implementation of the Myonode

The second implementation of the Myonode uses only commercially available ICs and passive components assembled on a custom designed PCB. This leverages the cutting edge in state of the art electronics while simultaneously increasing the reliability of the end device. This system offers a comprehensive and non-proprietary solution to many of the logistical challenges associated with device development as well as recording biopotentials chronically in both humans and small animals.

All microelectronic elements are available off-the-shelf and include an established ARM Cortex-M0 processor. This sidesteps many of the practical impediments of working with ASIC-based systems by simplifying replication of the system and facilitating rapid changes to its functional protocol afforded by reprogrammable firmware. In fact, one of the most exciting prospects of this technology is the ease by which more advanced processing tasks could be outsourced to the onboard microcontroller. For example, some processing tasks for advanced pattern recognition prosthetic control algorithms [86] might be incorporated in firmware so that directives rather than raw data are telemetered to the prosthetic limb. By integrating some level of processing or decision-

making prior to data transmission, a prosthetic control algorithm's performance might be augmented, accelerated, or in other ways enhanced. Flexible data processing and consolidation implemented in rewritable firmware may also prove to be a means of reducing total device power consumption by reducing the amount of data that is transmitted (and thereby reduce the RF transmitter's "on" time).

The circuit design, integration, prototype build process, packaging, and bench top evaluation of the custom PCB-based Myonode are covered in this section. Throughout the design phase, particular attention is given to the size constraints that come with working in mice. The maximum physical dimensions and permissible weight of the implant become even more restrictive when one considers that mouse models for neuromuscular diseases tend to be smaller than their wild-type counterparts owing to dysfunctional development or atrophy of skeletal muscle [162, 163]. Conceding that the device must be suitable for implantation both healthy and disease model mice results in a single-channel bioelectric sensor with a significantly smaller volume and mass than any comparable commercially available system.

The task set for the custom PCB-based Myonode is the same as the task set for the ASIC-based Myonode: continuous acquisition and telemetry of EMG. Key duties performed by the microelectronics integrated on the custom PCB include filtering, sampling, digitizing, and transmitting recorded data in real-time. The analog front-end (AFE) circuit for amplifying and filtering EMG prior to digitization is described in Section 3.3.1. The circuit structure for wireless power rectification and management is described in Section 3.3.2. The integration of the AFE, power management circuitry, the

MCU that orchestrates the functional protocol of the device, and the MCU's required peripherals is the subject of Section 3.3.3. Layout of the custom PCB and build procedure for the Myonode is also covered in Section 3.3.3. The bench top performance of the PCB-based Myonode is presented in Section 3.3.4.

3.3.1 AFE Design Using Commercial ICs

The AFE of the custom PCB-based Myonode is a differential recording channel comprised of a low-gain instrumentation amplifier (Texas Instruments, INA333) followed by a second gain stage that incorporates an active low-pass filter (see Figure 3.5 for a circuit schematic of the full AFE). The INA333 is selected for its high common-mode rejection ratio (CMRR) (100 dB), high input impedance (100GΩ), low power consumption (50μA), and appropriately small footprint (3 mm x 3 mm) [164]. One significant advantage to building the system from off-the-shelf components is the ability to adjust gain and bandpass filter cutoff frequencies as needed. Typically a majority of the gain is allocated to the second stage so that any DC offsets and low frequency signals from motion artifact or rectification of high-frequency noise is removed prior to significant amplification as these may otherwise cause the signal to rail.

Gain on the first stage is typically 10 (20 dB)—the minimum necessary to achieve the peak CMRR from the INA333. This gain is set using a single resistor as directed in [164]. The second stage gain is usually 30 (29.5 dB) for sEMG, resulting in a total AFE gain of 300 (49.5 dB). Second stage gain is usually 100 (40 dB) for imEMG, resulting in a

total AFE gain of 1,000 (60 dB). Second stage bandpass gain may be calculated using the known gain equation for an inverting operational amplifier:

$$Gain = \frac{V_{out}}{V_{in}} = -\frac{R6}{R5} \tag{3.1}$$

Prior to the instrumentation amplifier, the signal passes through a first-order, low-pass filter. Both inputs are DC biased to a mid-supply common mode voltage (designated CM in Figure 3.5) using pull-up resistors (R1 and R2 in Figure 3.5), which is necessary when using the INA333 in single-supply mode. Following passage through a buffer, this mid-supply voltage (designated REF in Figure 3.5) also provides a reference voltage to which the INA333 level-shifts its output. This same buffered voltage reference is supplied to the non-inverting input of the second stage op amp to maintain the mid-supply offset at the output of the AFE, which goes directly to the ADC. This DC offset is necessary since the SoC operates in single supply mode and its ADC can only read positive voltages. The buffer in Figure 3.5 prevents high frequency noise that may shunt to the common-mode supply voltage (CM in Figure 3.5) from coupling into the second stage of the amplifier and injecting noise into the downstream signal path.

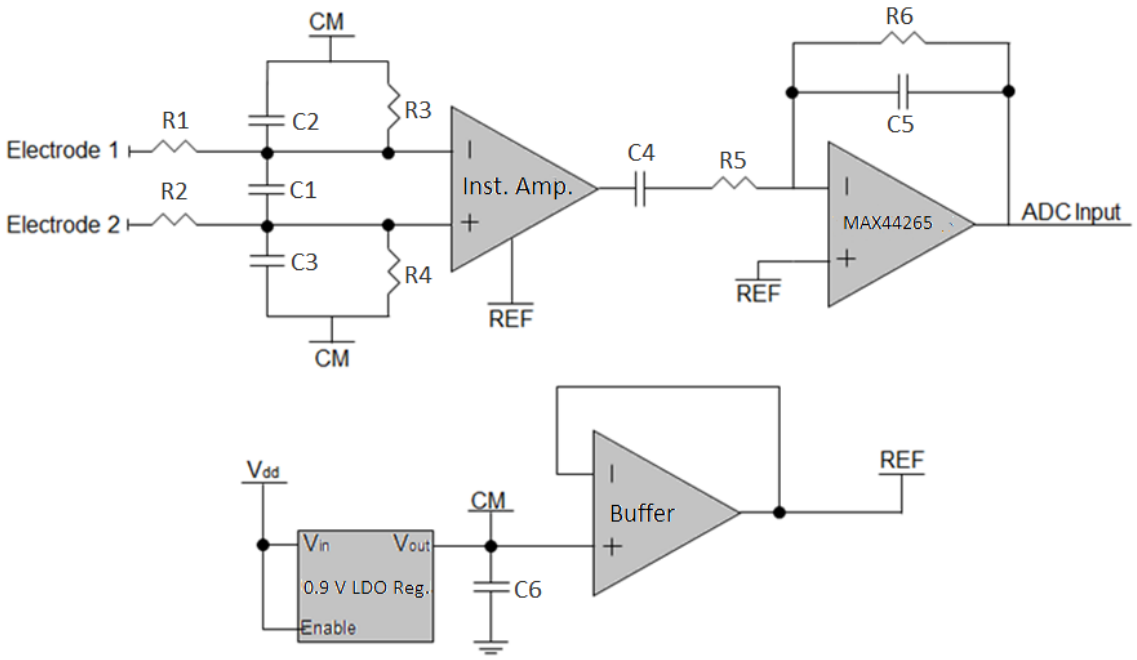

Figure 3.5 Analog front-end (AFE) of the custom PCB-based Myonode. The AFE consists of a low-gain first stage instrumentation amplifier and a higher gain second stage inverting amplifier. A mid-supply reference voltage is generated by a low drop-out (LDO) regulator and buffered to create a low impedance source. A low-pass filter prior to the instrumentation amplifier serves to remove high frequency noise from induced by the incident electromagnetic field necessary for wireless power coupling. A high-pass filter between the first and second stages AC couples the signal and an active low pass filter in the second stage allows for selection of the low-pass cutoff frequency.

The front end low-pass filter serves to shield alternating currents induced by the incident electromagnetic fields (which have frequencies in the single to tens of MHz) from the instrumentation amplifier inputs where they can be rectified into large amplitude, lower frequency noise that lies within the signal bandwidth. The bandwidth of the entire AFE may be estimated using established RC filter equations as follows:

$$f_{hp} = \frac{1}{2\pi C_4 R_5} \tag{3.2}$$

$$f_{lp} = \frac{1}{2\pi C_5 R_6} \tag{3.3}$$

where f_{hp} is the high-pass cutoff frequency and f_{lp} is the low-pass cutoff frequency.

More precise estimations of the AFE frequency response and small signal transient response are done using Simulation Program with Integrated Circuit Emphasis (SPICE)-based software. TINA-TI, a circuit simulator developed by Texas Instruments, is used here to take advantage of its library of component macros, which includes the INA33. Figure 3.6 shows the Bode magnitude and phase responses of the AFE configured for measurement of imEMG in a mouse. Figure 3.7 shows the simulated small signal response to a 100 Hz, 1 mV_{pp} for the same AFE configuration. The TINA-TI circuit simulation is also used to select the appropriate passive component values to attain desired AFE gain and bandwidth for other applications such as sEMG for prosthetic control.

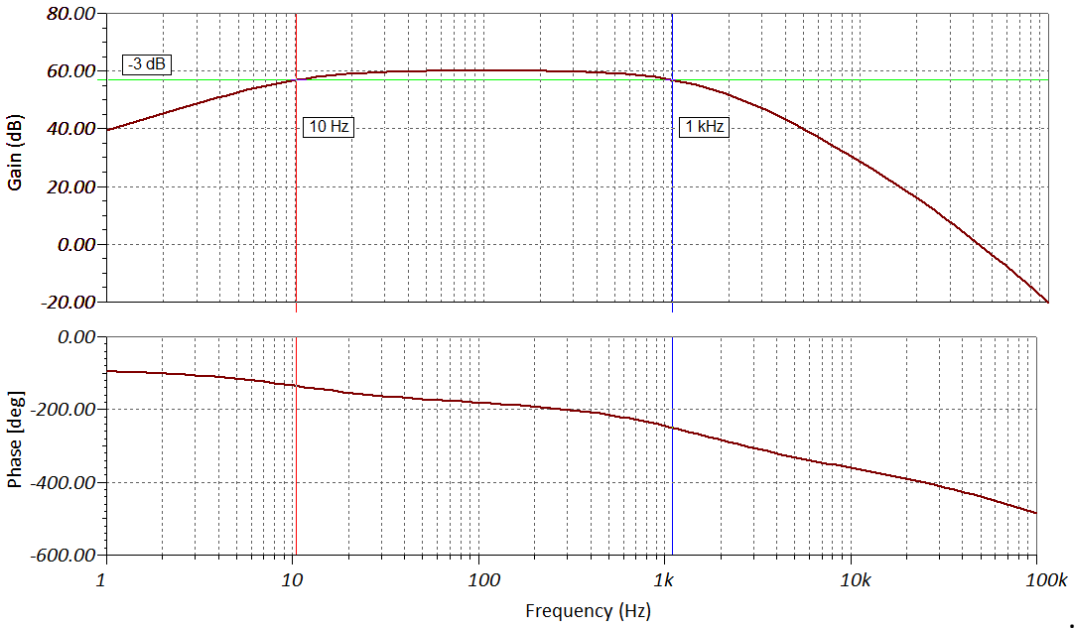

Figure 3.6 Bode gain and phase responses of the Myonode analog front-end (AFE) simulated in TINA-TI. AFE is configured for with a bandpass gain of 60 dB and a bandwidth of 10—1,000 Hz.

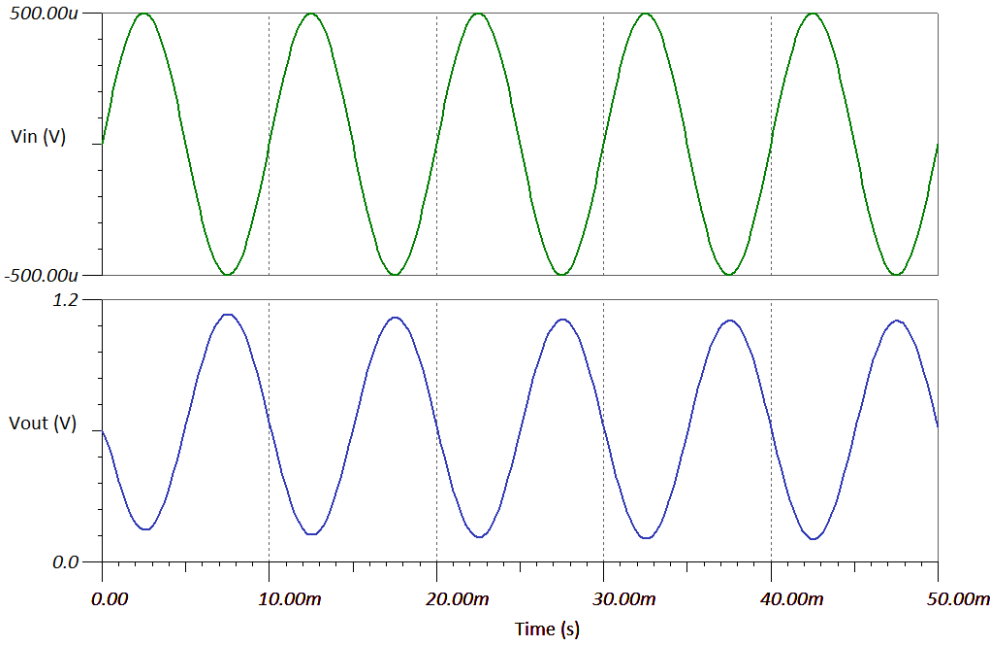

Figure 3.7 Small signal transient response of Myonode analog front-end (AFE) to a 1 mV_{pp} sinusoidal input waveform at 100 Hz, where the phase delay is exactly 180°.

3.3.2 Power Management Circuitry

Conversion of applied magnetic fields into a usable voltage supply is achieved by the rectifier and power management circuit shown in Figure 3.8. Alternating currents induced in receiving coil are capacitive filtered through an impedance matching network (K-inverter) before being rectified to a DC voltage. The rectifier topology used in this device is a single stage bridge rectifier. A storage capacitor on the output of the rectifier serves to buffer the supply voltage during short bursts of elevated current consumption, such as those that occur when the transmitter is turned on to send data. The rectified voltage is regulated to 1.8 V by a low-dropout (LDO) linear voltage regulator. This regulated voltage supply is used to power all active circuit components. Subsequently, this voltage is down-regulated to 0.9 V to provide a stable common-mode reference voltage to the AFE (see Figure 3.5). Stabilizing capacitors are used at the outputs of both regulated voltages and decoupling capacitors are placed proximate to IC power supply pins to reduce the effects of electromagnetic interference (EMI).

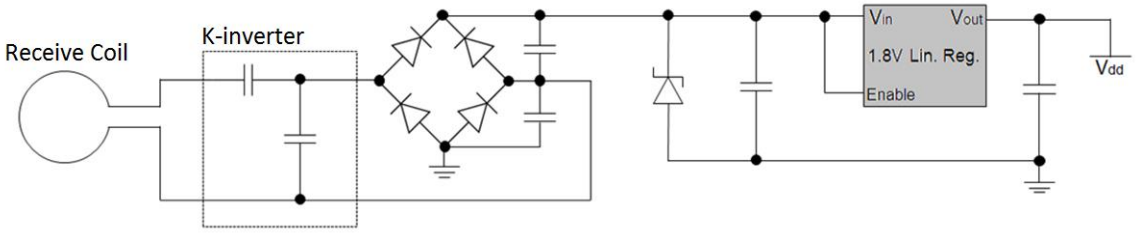

Figure 3.8 Power rectification and management circuitry on the custom PCB-based Myonode. Incoming alternating currents are capacitive filtered in the k-inverter (C1 and C2) and rectified to a DC voltage in a single stage bridge rectifier. A stabilizing capacitor (C5) serves to buffer the supply voltage from spikes in current consumption and is placed in parallel with a 5.6 V Zener diode, which protects the regulator from rectified voltages above its maximum input voltage.

All power necessary to run the Myonode's microelectronics is wirelessly coupled to the system using the MRC strategy implemented by Henry Mei. This design method enables the realization of maximum attainable PTE. This method works by implementing analytically derived optimal impedance matching conditions suggested by the bandpass filter model of inductive links. This allows the WPT link to be precisely tuned for optimal PTE to single or multiple receive devices [165, 166].

The WPT link is designed for operation at 13.56 MHz. This is selected by a combination of factors including desired dimensions of the testing environment (which influences the geometry of the external coil) as well as considerations for the designated ISM radio bands. The source for the electromagnetic field is supplied by an RF signal generator (Agilent, N5182A) and amplified by a class E amplifier (Mini-Circuits, ZHL-1-2W-S+). In the course of all bench top and animal work the power level emitted

by the external coil is kept below maximum output power requirements as designated by the FCC regulations for intentional radiators [106].

3.3.3 Full System Integration and PCB Design

Device logic is mediated by a central MCU. The MCU employed in this device is a 32-bit ARM® Cortex™ M0 within a low-power system-on-chip (SoC) package (Nordic Semiconductors, nRF51822). This SoC has a built-in 8/9/10-bit ADC which receives data in the range of 0-1.8V from the AFE. It also has an embedded 2.4GHz transceiver which outputs modulated data packets through a balun and finally to a ceramic 2.4GHz chip antenna (Johanson Technologies, 2450AT07A0100). System logic and operations are clocked at 16 MHz by means of an off-chip crystal oscillator. Figure 3.9 shows a schematic of the microcontroller and its peripherals.

The Myonode is enabled with wireless data telemetry through an embedded transceiver on the low power SoC. The sampling rate of the system is typically set to 5 kHz, which requires the MCU to wake up from sleep mode every 200 µs, record a data point, then go back to sleep. Utilizing sleep mode is one of multiple strategies employed to reduce total power consumption. In addition to running all active components on the lowest possible voltage supply (1.8 V), the device is able to save power by putting samples into packets for transmission rather than sending each sample independently. This minimizes overhead power consumption from transmitter startup and reduces the total amount of time in which the transmitter is active; a state in which it draws a current of approximately 14 mA. However, as the packet size increases, the probability

of data corruption during wireless transmission becomes higher. To balance between efficiency and data integrity, a payload length of 32 bytes is chose. Once 31 bytes of data is collected, the microcontroller triggers the transmit task and the transmitter uses direct memory access to retrieve the 31 samples stored in memory and puts them in the payload. Each packet of data consists of a 5-bit preamble and 5 bytes of address information followed by the payload (1-byte packet ID + 31 bytes of data) and, finally, a 2-byte cyclic redundancy check. The firmware for the Myonode is written in C programming language by Grant Wang, a member in the Center for Implantable Devices at Purdue University.

The device communicates with a base station using the telemetry protocol developed by Nordic Semiconductor. The base station's functional tasks are regulated by the same Nordic Semiconductor SoC as the Myonode. It receives data packets through the integrated receiver which has a sensitivity of -85 dBm for a 0.1% bit error rate (BER) at 2 Mbps. The data is sent via a serial-peripheral interface (SPI) to a computer where is can be plotted in real-time and saved. In the case where multiple devices are operating in an array, the base station can receive data from up to eight channels simultaneously by the sharing the SPI bus. Additionally, each device is assigned a unique 2 MHz-wide channel within the 2.4 GHz ISM band to avoid interference and synchronization issues. In all cases the wireless signal is modulated using Gaussian frequency shift keying (GFSK).

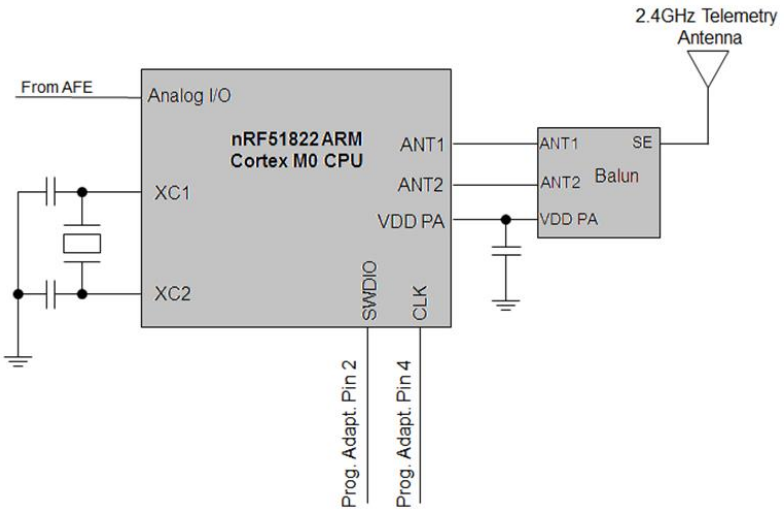

Figure 3.9 Circuit schematic of the system-on-chip (SoC) and its essential peripheral components for timing and data transmission, which are used in the custom PCB-based Myonode. The nRF51822 SoC has an integrated analog-to-digital converter (ADC), 2.4 GHz transceiver, and 32-bit ARM® Cortex™ M0.

The AFE, power rectification and management circuitry, MCU, and necessary MCU peripherals are integrated on a custom 4-layer PCB fabricated by Sierra Circuits. Efforts to miniaturize the finished device implored that the following custom PCB specifications be used: 0.004” minimum trace width/spacing, 0.006” minimum via diameter, 0.03” finished board thickness and one blind via set on an FR-4 dielectric substrate. A low temperature solder paste (Chip Quik, SMDLTFP) is used to assemble microelectronic components on the board. Following assembly the firmware is programmed into the MCU’s flash memory through a peripheral 10-pin M50 vertical male header that is not part of the final device. This header is detached and the extra board material is removed to minimize the size of the finished device, which has dimensions of 5mm x 8 mm x 2.7 mm.

The recording electrode pair is connected to the microelectronics through two 0.3 mm vias and set with a two-part silver conductive epoxy (8331S-15G, MG Chemicals). Devices built for chronic implantation use 304 series stainless steel wire (0.051 mm diameter) insulated with nylon to connect the board to two gold pad electrodes deposited on a parylene substrate similar to a patch or epimysial electrode. The geometry of the electrode pads used for the *in vivo* experiments is square with a side length of 0.5 mm and an inter-electrode spacing (center to center) of 3 mm.

The receiving coil for chronic implantation in mice is assembled using 22 AWG magnet wire (Belden, 8051) and is formed by making three turns around a rod with a diameter of 12 mm. The coil is connected to the PCB by soldering to pads connected to the inputs of the K-inverter. The receiving coil adjoined to the PCB can be seen in Figure. 3.10. The final step in assembly is the process of sealing the device, which is done using parylene C deposition. Parylene C is a conformal dielectric with demonstrated biological inertness [167]. It is vapor deposited onto the device to a thickness of 20 µm prior to implantation.

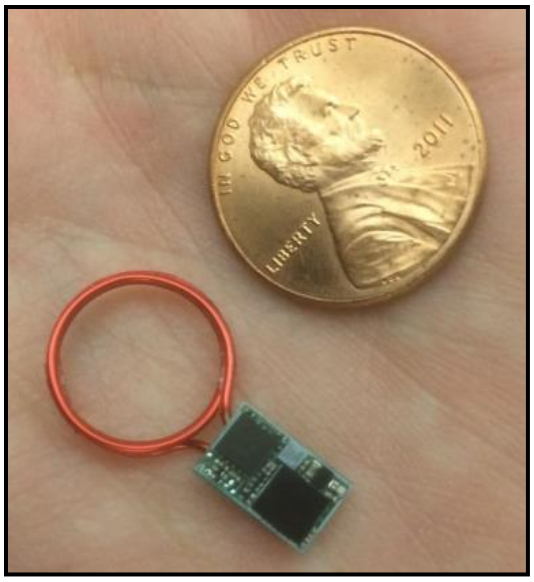

Figure 3.10 Myonode device constructed from commercial microelectronics integrated on a custom PCB which measure 5 mm x 8 mm x 2.7 mm once assembled. The PCB is affixed to a rigid receive coil having a diameter of 1.2 cm and a thickness of 3 mm, which is tuned for MRC power transfer with an external transmitting coil having a diameter of 13 cm.

Alternatively, coils printed on a thin, flexible substrate are designed to reduce the effective footprint of the receive coil and better sustain dynamic loading and flexural stress, which are expected in both applications of the Myonode. These coils are 15 mm x 15 mm and are printed on a polyimide substrate fabricated by FlexPCB (see Figure 3.11). They have a total thickness of 0.13 mm and a minimum bend radius of 0.91 mm, which allows them to conform to the shape of a body. This may improve biocompatibility for subcutaneous implantations in mice and simplify integration with fabric body liners for the purposes of sEMG control of upper-limb prostheses.

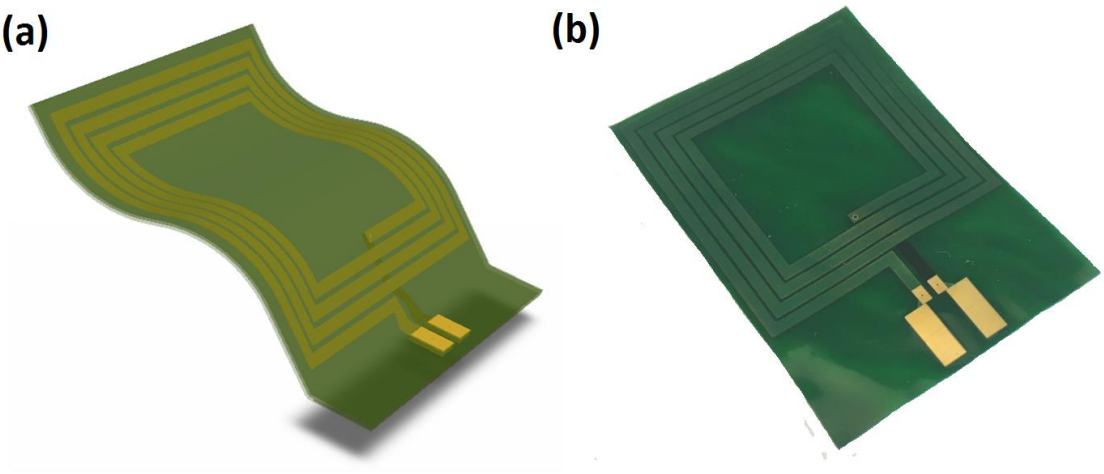

Figure 3.11 (a) Rendering of receive coil fabricated on a flexible polyimide substrate with 2 oz. copper deposition and insulating polyimide coverlay. Coil footprint is 15 mm x 15 mm and has a finished thickness of 0.13 mm. (b) Picture of the fabricated flexible coil.

3.3.4 Bench Top Performance of the Myonode PCB

The assembled Myonode PCB is put through a series of engineering confidence tests prior to being used for bioelectric data acquisition. These include a fidelity check, a wireless powering check, and a soak test. The data fidelity check is performed by applying a sinusoidal waveform across the differential inputs and comparing the known input waveform to the reconstructed signal following digitization, transmission, and reconstruction. An example of this is given in Figure 3.12 for a device configured to collect sEMG. The wireless powering check entails placing the finished device in the WPT environment and observing successful device power up and data transmission. The soak test is carried out through submersion of the packaged device in 0.9% phosphate buffer solution (PBS) for 24 hours followed by a second wireless powering check.

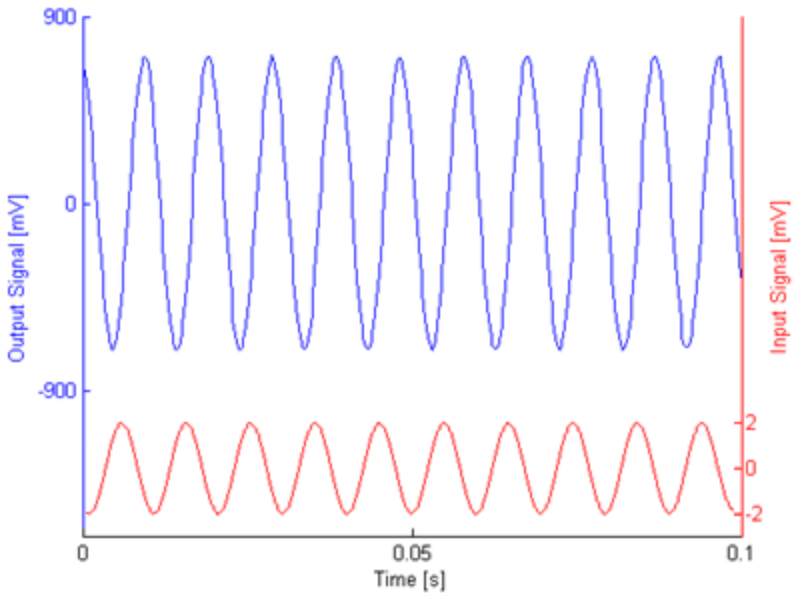

Figure 3.12 Data fidelity test for a device configured for sEMG collection. Analog front-end (AFE) gain is set to 300 (49.5 dB)

The frequency response of the AFE circuit is measured using a dynamic signal analyzer (Agilent, 35670A) and is shown in Figure 3.13. The measured result is a close match with the Bode plot generated by the TINA-TI circuit simulation given in Figure 3.6. The input-referred noise of the system is quantified by measuring the power spectral density (PSD) at the AFE output when the differential inputs are shorted together and subsequently factoring out the gain response. Integrating the measured PSD, which is shown in Figure 3.14, over the recording channel bandwidth yields the peak-to-peak input-referred voltage noise, which is 2.3 V_{pp}.

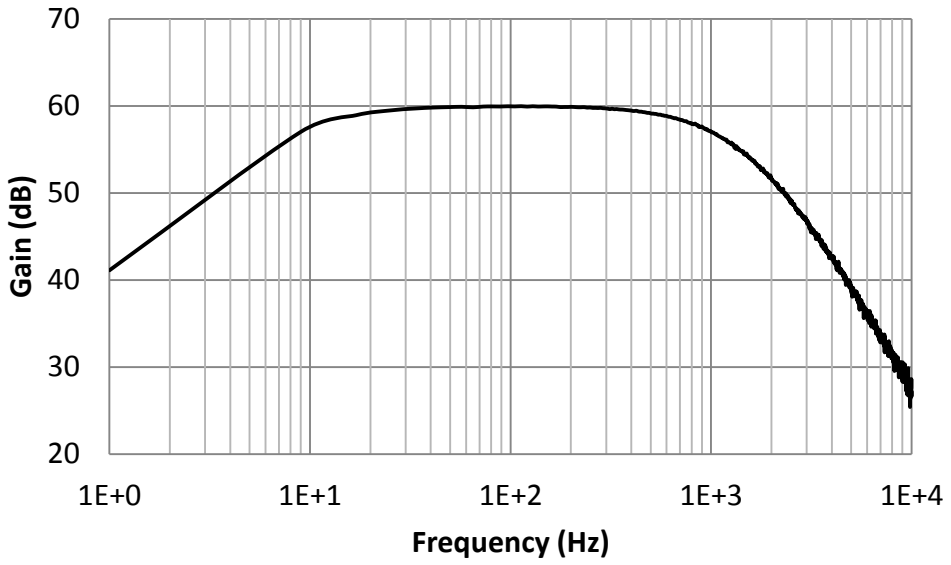

Figure 3.13 Measured frequency response of the custom PCB-based Myonode analog front-end (AFE) configured for intramuscular EMG (imEMG) recording. Bandpass gain is 60 dB, high-pass -3 dB cutoff is 10 Hz, and -3dB cutoff is 1 kHz.

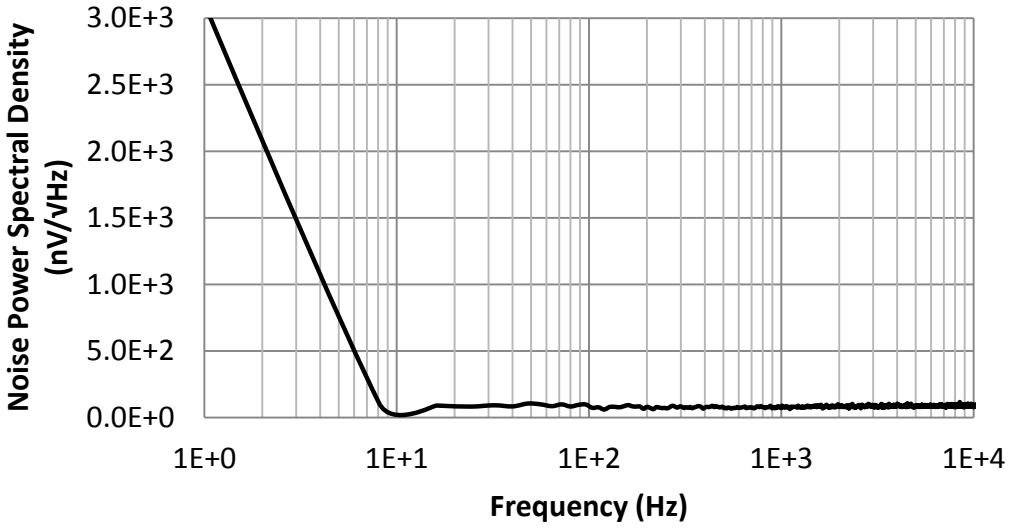

Figure 3.14 Measured input-referred noise power spectral density (PSD) of the analog front-end (AFE) on the custom PCB-based Myonode. Integration of the PSD over the bandwidth results in a total input-referred noise of 2.3 μV_{pp}.

The common-mode gain of the recording channel is measured on the dynamic signal analyzer by shorting the differential inputs together and applying a sinusoidal input waveform with an amplitude of 700 mV_{pp} while sweeping the frequency across the bandwidth. The input waveform amplitude is selected so that it is large enough to be detected at the highest common-mode attenuation without railing the AFE at the frequency of lowest common-mode attenuation. Using both the differential and common-mode gain measurements allows the CMRR of the AFE to be calculated:

$$CMRR(f) = 20log_{10}\left(\frac{A_d(f)}{A_{cm}(f)}\right) \tag{3.1}$$

where $A_d(f)$ is the frequency dependent differential voltage gain and $A_{cm}(f)$ is the frequency dependent common-mode voltage gain. Figure 3.15 plots the calculated CMRR from 1 Hz to 5 kHz and reveals that the CMRR is greater than 80 dB from 1 to 100 Hz. This is important because the largest expected common-mode noise source is power lines, which create electromagnetic fields oscillating at 60 Hz. It is of interest to note that the reported CMRR of the INA333 instrumentation amplifier is >100 dB . The reason for this discrepancy is the addition of passive elements (resistors and capacitors) prior to the instrumentation amplifier input (see Figure 3.5). These circuit elements are necessary for single supply function within the WPT environment, but cause CMRR depletion due to mismatch in their values (surface mount chip components of this size tend to have tolerances between 1 and 5%). While on the low end, a CMRR of 80 dB

meets the minimum recommended specification for EMG [168].Table 3.2 serves to consolidate this and other performance specifications for the custom PCB-based Myonode.

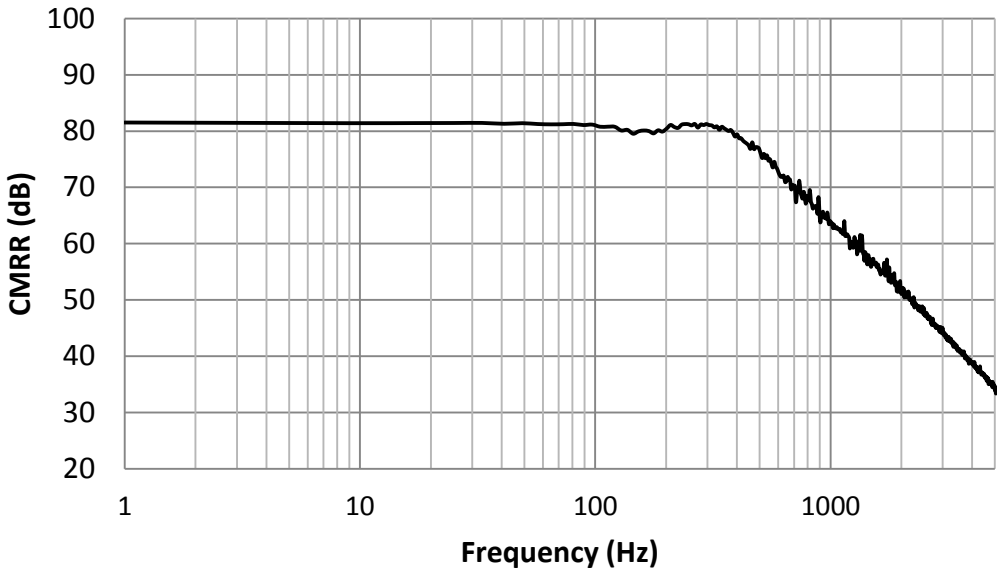

Figure 3.15 Measured common-mode rejection ratio (CMRR) of the analog front-end (AFE) on the custom PCB-based Myonode. Input waveform was common to both AFE inputs and was 700 mV_{pp} in amplitude.

Table 3.2 Summary of custom PCB-based functional parameters. Minimum and maximum values given for adjustable parameters and reflect ranges used in this work. Typical values represent default settings or measured characteristics.

Parameter	***Conditions***	***Min***	***Typ.***	***Max***	***Unit***
Bandpass gain		40	60	66	dB
High-Pass filter cutoff		0.1	10	--	Hz
Low-Pass filter cutoff		--	1	5	kHz
ADC digital resolution		8	8	10	bits
ADC analog resolution		--	4.7	0.6	µV
Input-referred voltage noise	f = 10Hz to 1kHz	--	2.3	--	μV_{pp}
Common-mode rejection ratio	f = DC to 60Hz	--	>80	--	dB
Sampling rate		--	5	20	kHz
Transmission (data packet send) rate		--	161	--	Hz
Transmitter output power		-20	4	4	dBm
Transmission center frequency		--	2.4	--	GHz
Transmission channel bandwidth		--	2	--	MHz
Average current consumption	Sampling Rate = 5kS/s	--	1.6	--	mA
Average power consumption	Sampling Rate = 5kS/s	--	2.9	--	mW

3.4 *In Vivo* EMG Acquisition in Mice

The *in vivo* validation of the Myonode involves implantation of the device in both wild-type and disease model mice. The purpose of these experiments is threefold: first, to confirm that the packaging strategy is viable for device implantation; second, to determine whether or not the device is suitably small for subcutaneous placement in mice; and third, to observe the fidelity of power transfer within the WPT environment. An explanation of the surgical methods and experimental procedures used to successfully measure voluntary and spontaneously evoked EMG in both wild-type mice and a familial MD disease model are contained in this section.

3.4.1 Experimental Design and Methods

The first *in vivo* test for the fully wireless Myonode is to measure a known stimulus-evoked response with animal under anesthesia. This serves as a final check to be sure that the electrode design and configurable circuit parameters have been chosen and implemented correctly. The device's recording electrodes are placed on the surface of the lateralis gastrocnemius (LG) muscle and 100 µs-long stimuli are applied to the sciatic nerve using a bench top stimulator. Stimulus frequency is kept low (0.5 Hz) to avoid time-dependent changes in the measured response as a result of nerve desensitization or muscle fatigue, and the evoked responses are recorded at a sampling rate of 5 kHz. The stimulus current amplitude is gradually increased until an evoked response is observed. Figure 3.16 illustrates a series of five stimulus-evoked CMAPs measured by the Myonode in response to a stimulus pulse with a current amplitude of 72µA (charge of 7.2 nC per cycle).

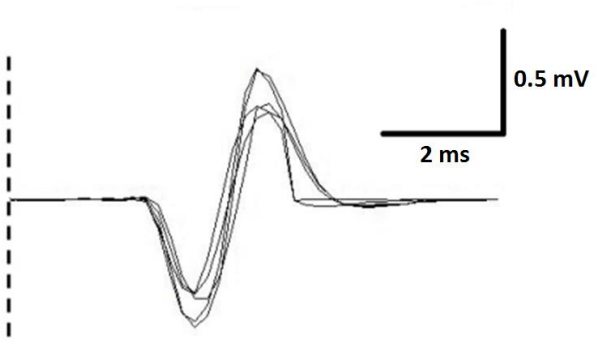

Figure 3.16 Five superimposed compound muscle action potentials (CMAPs) measured from the lateral gastrocnemius (LG) muscle by the fully wireless Myonode in response to 100µs, 72µA stimulation applied to the ipsilateral sciatic nerve.

Following demonstration that the device—as well as its supporting hardware and software—can collect and reconfigure a CMAP response, the device is implanted in a mouse to record chronic, voluntary evoked EMG. The surgical procedure includes a 1 cm incision transverse to the animal's midline while in the prone position. Blunt dissection technique is used in the midsection of the back to create a pocket for the device to be inserted subcutaneously. The electrode pads are placed on and sutured to the surface of the biceps femoris. Electrode sutures are placed at the junction between the electrode leads and pads and the device is secured to the fascia by two suture loops around the receive coil. The biceps femoris muscle is the selected target for the first implantation since it is close to the animal's midsection, where the bulky device will fit under the loose skin without inhibiting motion of the limbs. This allows the surgeon to avoid making a larger single incision or second incision in order to reach a target that is more remote relative to the device. Following recovery the animal is placed inside the WPT environment for data collection.

The WPT testing environment constructed for untethered mouse work consists of a two-turn transmitting coil made from 10 AWG copper wire made to fit around the base of a tub with a 13 cm diameter as shown in Figure 3.17. The dimensions of this environment are selected such that there would be sufficient coupling between the transmitting and receiving coil at any point within the enclosed space and sufficient room for the mouse to comfortably move. Both of these aims are achieved within while maintaining an output (transmitting) power below 1 W using the testing environment shown in Figure 3.17.

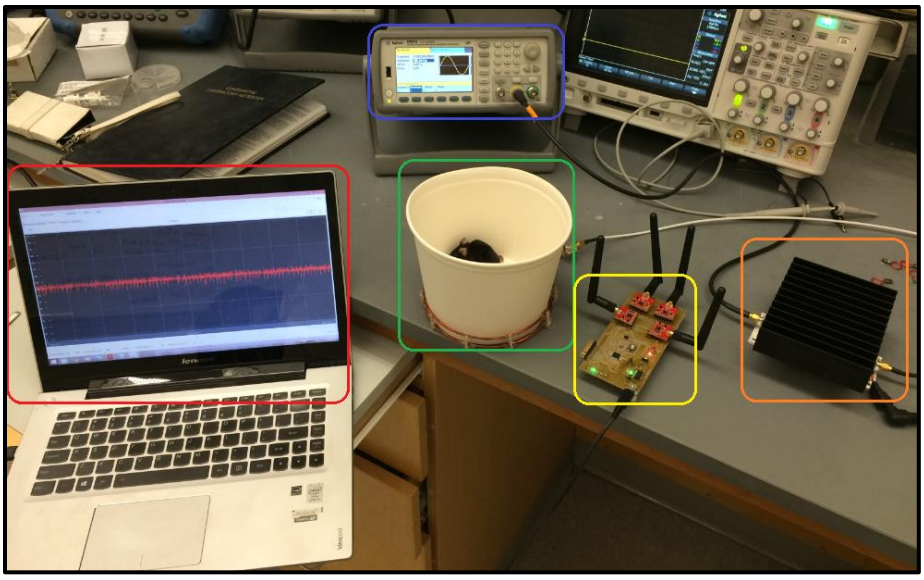

Figure 3.17 Experimental setup for chronic implantation of custom PCB-based Myonode in freely behaving, untethered mice. The wireless power transfer (WPT) environment consists of a power transmitting coil encircling a tub with a 13 cm diameter (green). The RF signal is sourced from a waveform generator (blue) and amplified through a class E amplifier (orange). Data is telemetered from the implanted Myonode to a base station (yellow), which relays the data to a software interface (red) through a USB interface.

3.4.2 Collection of Voluntary Evoked EMG in Wild-Type Mice

All wild-type mice are from the C57BL6/J (Black 6) strain. The *in vivo* EMG collected from a freely behaving wild-type mouse is shown in Figure 3.18 along with baseline data collected while the mouse is under anesthesia. These data are recorded from epimysial (pad) electrodes on the biceps femoris. The data collected on day 1 show the characteristic, periodic interference patterns as the mouse moves around the WPT environment. This is an exciting outcome as it demonstrates that the device and integrated WPT strategy can enable collected of voluntary evoked EMG from an untethered, freely behaving animal. However, after three days post-implantation, the

EMG signal is visibly deteriorated and eventually lost within the noise floor. It is suspected and subsequently confirmed that this is due to a mechanical failure of the electrode leads, which caused one of the differential inputs to float.

The wild-type mouse experiment is terminated at day 16 so the device can be explanted and inspected. Importantly, though, the device continued to work in the WPT testing environment, suggesting that the surgical and packaging strategies will support long-term viability.

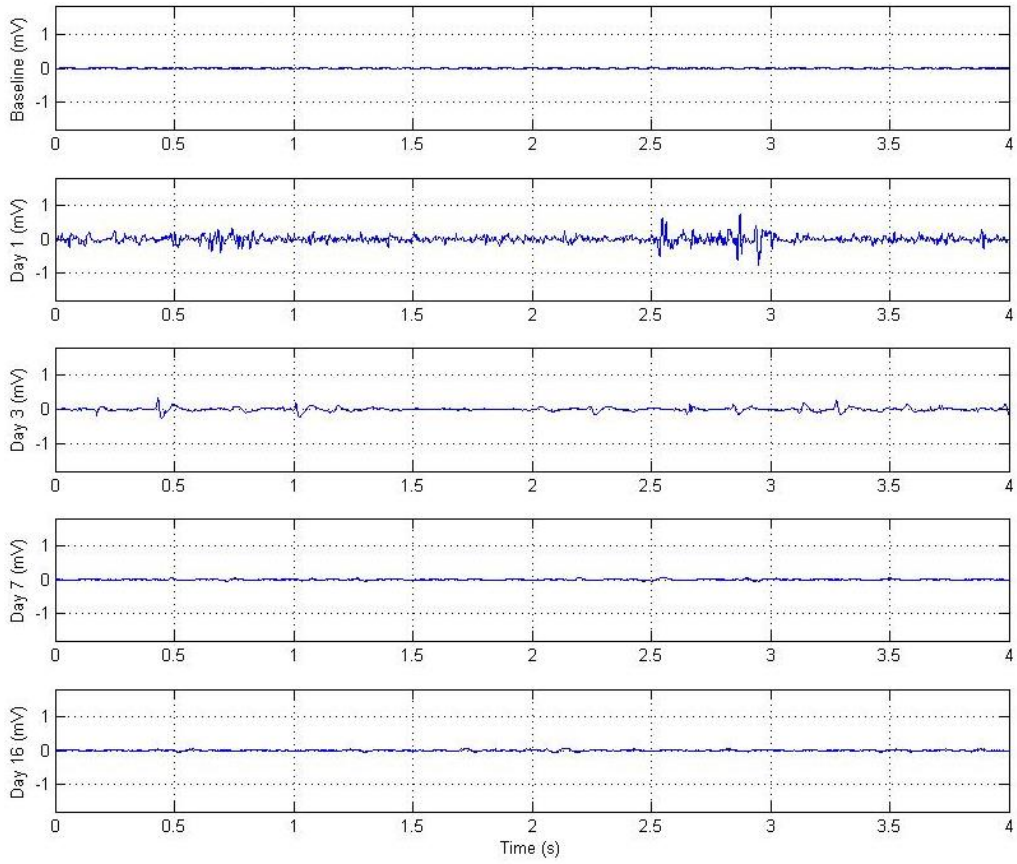

Figure 3.18 EMG recorded from biceps femoris muscle of a mouse over the course of 16 days. Baseline data is collected from anesthetized animal immediately following device implantation. Signal deterioration over time is due to a mechanical failure at the junction between the electrode pad and lead. Device operation and telemetry is successful for 16 days at which point the experiment is ended so that the device may be explanted and examined. All data has been digitally bandpass filtered (5Hz-1kHz passband) and notch filtered at 160Hz and all 160Hz harmonics to remove periodic noise associated with data transmission.

3.4.3 Collection of Aberrant Muscle Activity in Neuromuscular Disease Model

A Myonode device is implanted in a mouse model for familial MD to collect disease-related aberrant muscle activity. The surgical procedures and device placement are identical to those used for chronic implantation in wild-type mice. In this case the device is implanted in a mouse that has a mutation of the *nmf417* allele in the LAMA2

gene (strain C57BL/6J-Lama^{2dy7J}/J). Mutations of the LAMA2 gene cause congenital MD type 1A in humans [169]. This model is characterized by hypomyelination, muscular degeneration, and eventual loss of hind limb function. As peripheral nerves and muscle become affected, large, transient muscle fasciculation can be seen. This overt phenotype is the reason that this particular disease model is selected for early applications of the Myonode. EMG associated with these fasciculation can be recorded from the mouse during stationary periods in which spontaneous contractions of the hind limb are observed.

Figure 3.19 illustrates aberrant muscle fasciculation collected from a familial MD model mouse using the fully wireless Myonode in the WPT testing environment. This electrophysiological phenotype is recorded during a stationary period (no ambulation) which spontaneous contractions of the hind limb are observed. This is one example of a disease signature that can be tracked with relative ease using a fully wireless and implantable biosensor. This signature can be used to better understand disease progression or evaluate novel therapies without the potential confounds introduced by a tethered apparatus or battery replacement in a battery-powered system.

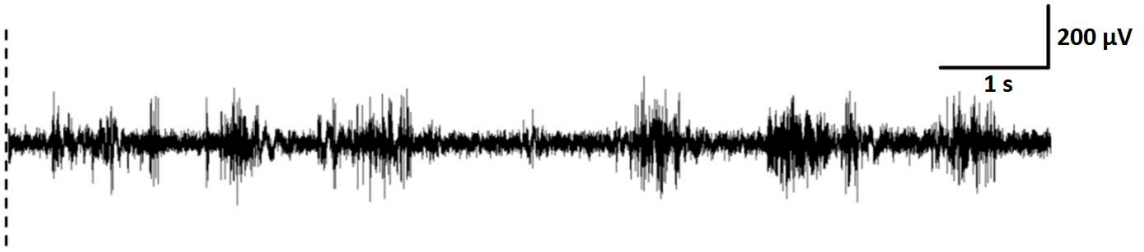

Figure 3.19 Aberrant muscle fasciculation measured from the biceps femoris muscle of a mouse model for familial muscular dystrophy (MD). The animal is stationary during the recording period during which time spontaneous contractions of the hind limb are observed.

3.5 Human EMG Measurement for Prosthetic Arm Control

In this section the custom PCB-based Myonode is used to collect human imEMG and sEMG, which is subsequently integrated with established myoelectric control schemes to direct both virtual and electric-powered upper-limb prostheses. One of the goals for the wireless, single-channel Myonode is to embed multiple devices in an array within muscles to create reliable neural interfaces for upper-limb prosthesis control. The current shape and size of the device does not permit intramuscular implantation, so further refinement of the device and an institutional review board (IRB) approval is needed before this can happen. In the interim, however, two of the most critical capabilities of the device may be tested: first, its ability to measure the desired signal and, second, its ability function when placed in an array with other devices.

Human-subject imEMG is collected to demonstrate that the device can retrieve useable EMG from a differential electrode pair embedded in muscle. Human-subject sEMG is used to test an array of eight devices functioning simultaneously. In both cases

the usability of the measured EMG is demonstrated by interfacing it with established myoelectric prosthetic control systems.

3.5.1 Collection of imEMG from an Able-Bodied Human Subject

An imEMG signal from the *extensor carpi radialis longus* (ECRL) muscle in an able-bodied human subject is collected with the fully wireless device and used to control a powered prosthetic arm in development at the Rehabilitation Institute of Chicago [170]. The imEMG is collected using bipolar fine wire EMG electrodes (Natus Medical, Inc.) that are connected to the Myonode through an interposer board. Fine wires are introduced into the ECRL muscle using a hypodermic needle. The insertion location is guided by reference texts [171] and confirmed with corresponding test contractions. The EMG is sampled at 5 kHz. The mean absolute value (MAV) of the EMG signal is calculated from a 250 ms sliding window with a 50 ms frame increment. The MAV is used as the input to a three-state configuration of single-site myoelectric control [77].

The magnitude of the MAV signal is mapped to one of three possible states in this myoelectric control system: no motion, hand close, or hand open. The mappings is determined by two thresholds on the MAC signal, which delineated three ranges corresponding to the three states. The no motion state resulted from MAV activity less than the lower threshold; the hand close state resulted from MAV activity between the two thresholds, and the hand open state resulted from MAV activity greater than the higher threshold. Threshold values are set empirically by the experimenters—similar to clinical methods—such that the user could repeatedly differentiate between all three

states without fatigue. When in either of the two active states, the prosthesis is moved at a constant velocity.

Figure 3.20 depicts imEMG collected by the Myonode from the ECRL muscle of an able-bodied patient. While configuring the three motion classes of the myoelectric control system, the patient is directed to produce three isolated contractions at a self-selected “high-intensity” followed by two isolated self-selected “low-intensity” contractions, which can be seen distinctly in Figure 3.20. These data are streamed in real-time and used to differentiate between three states of a single degree of freedom, resulting in real-time myoelectric control of a prosthetic hand. Figure 3.21 portrays the setup for this experiment.

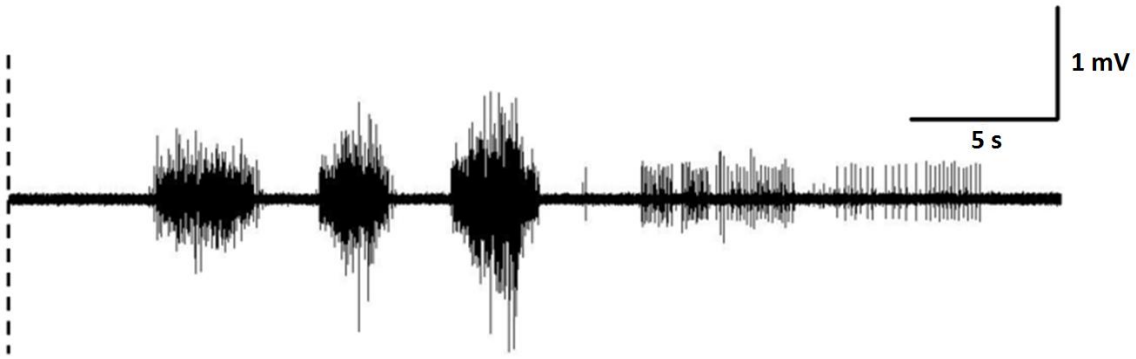

Figure 3.20 Intramuscular EMG (imEMG) collected by a fully wireless Myonode from the extensor carpi radialis longus (ECRL) muscle of an able-bodied human subject (gain = 54 dB). Subject is directed in this instance to produce three self-selected “high-intensity” contractions followed by two self-selected “low-intensity” contractions.

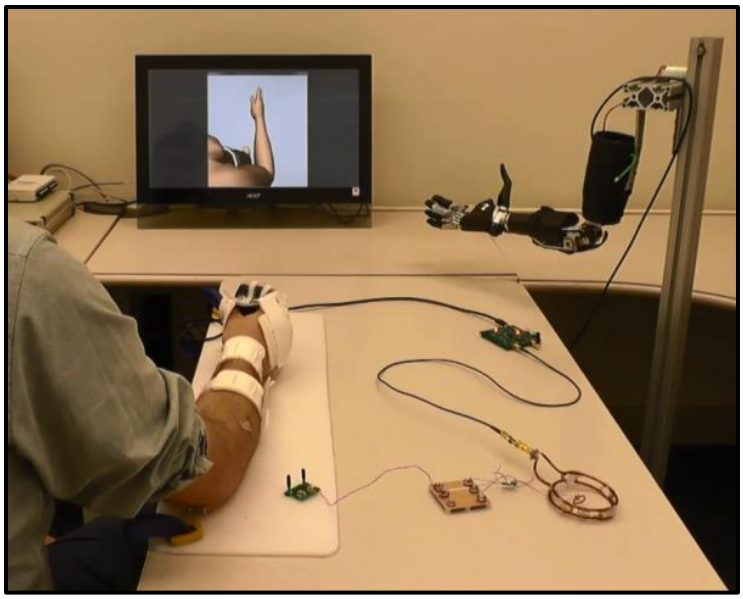

Figure 3.21 Experimental setup to collect imEMG from extensor carpi radialis longus (ECRL) muscle to direct hand open and hand close in both a virtual and robotic prosthetic arm. Fine wire needle electrodes are fed through an interposer board to connect to the Myonode device on the bench top.

3.5.2 Myonode Cuff Array for Multi-Channel sEMG Recording

In addition to wirelessly powering a single device, the MRC optimization methodology can be expanded to incorporate multiple receivers by strategically controlling the power distribution [172]. Power coupling to eight devices is achieved by application of an anti-Helmholtz transmitting coil designed by Henry Mei. This coil is intended to be worn around the forearm as shown in Figure 3.22(a) in a manner similar to current inductive power links for transradial amputees [50]. The transmitting coil is made using 8 AWG copper wire and consists of two coils strategically wound in opposite directions then connected in parallel from the feed point indicated in Figure 3.22(b) to achieve an anti-Helmholtz magnetic field distribution. This field distribution is

characterized by magnetic fields which point outward and perpendicular to the surface of the forearm as shown in Figure 3.22(c). This allows for adequate and equivalent coupling between the transmitting and receiving resonators sufficient to power eight devices positioned circumferentially around the forearm.

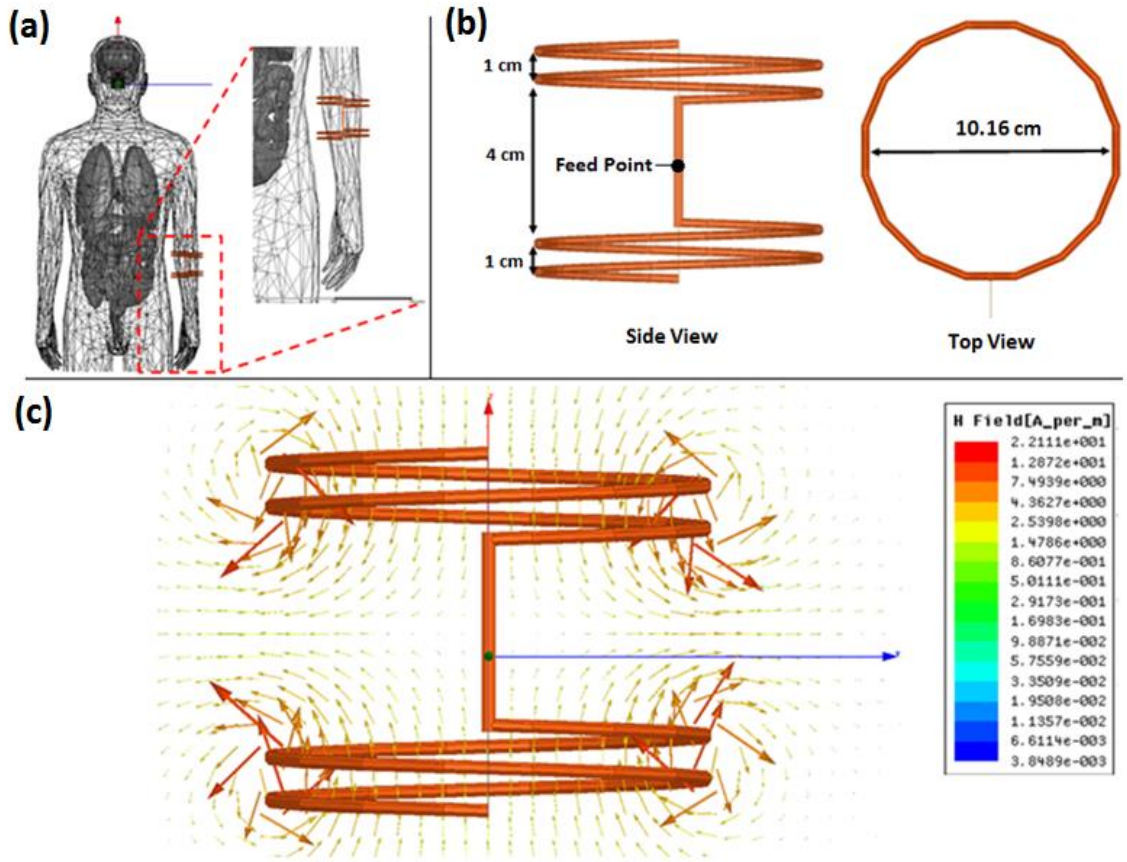

Figure 3.22 Simulation of the transmitting anti-Helmholtz coil for power transfer to an array of Myonode's placed circumferentially around the forearm. (a) Intended placement of the transmitting coil around a human body model in HFSS®. (b) Transmitting coil dimensions when viewed from the side and top. (c) Illustration of the magnetic (H) field vectors characteristic of the anti-Helmholtz construction.

The flexible receive coils described in Section 3.3.3 are used here as they will conform the surface the forearm and put less stress on the junction with the PCB. The intended arrangement of eight printed spiral coils within the anti-Helmholtz coil is depicted in Figure 3.23. Figure 3.24(a) shows the assembled fabric forearm cuff with eight Myonode devices connected to dry metal dome electrodes (Motion Control, Inc.) embedded in the fabric cuff. This arrangement allows for eight channels of differential sEMG to be measured around the circumference of the forearm. Minimal adaptations were required of the Myonode PCB in order to make it compatible with the forearm cuff. A stainless steel extension spring is connected to the each differential input via on the PCB by way of a copper post potted in the via at one end and inserted into the extension spring at the other end. The copper post is soldered at both junctions for stability and electrical continuity. Metal snap connectors are soldered to the free ends of the extension springs so that they could be easily connect and disconnected from the dry metal dome electrodes. Figure 3.24(b) shows one of these modified Bionodes adapted for integration with the fabric cuff.

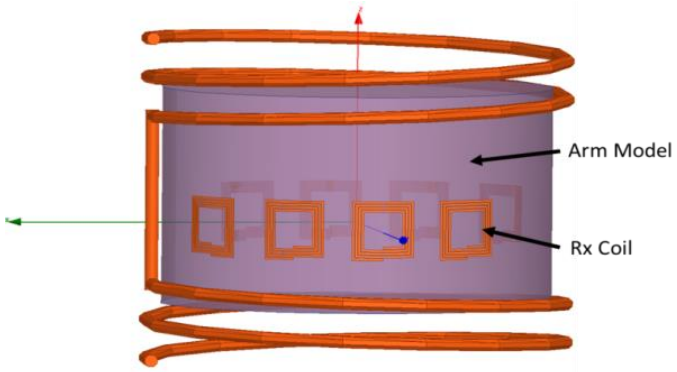

Figure 3.23 Transmitting anti-Helmholtz coil modeled in HFSS® with eight flexible receive coils positioned equidistant from one another around the inside coil the transmitting and spaced equidistant from one another on the surface of the forearm (purple).

Figure 3.24 Adaptation of the Myonode for integration of multiple devices on an adjustable forearm cuff for multi-channel surface EMG (sEMG) recording. (a) Fabric forearm cuff with eight pairs of embedded dry metal dome electrodes. Electrodes interface with the differential recording inputs of the Myonode through metal snaps. (b) Single Myonode adapted for the forearm cuff. Metal snaps are soldered to an extension spring which is connected to the Myonode through copper post potted in a via. The rigid receive coil is replaced by a flexible coil that will conform to the curve of the forearm.

During testing the fabric cuff is secured snugly around the proximal third of the subject's forearm—near the center of the brachioradialis muscle. An elastic bandage is wrapped around the cuff and forearm to protect the microelectronics. The anti-Helmholtz coil is then slipped over the top of the cuff and the elastic bandage. A pattern recognition system is used to correlate the streaming sEMG data from the array of devices to the intended motion of the user. In order to train the system, the user provides four repetitions of training contractions, which are comprised of 3-second contractions for each of the following seven motion classes: no motion, pronation, supination, wrist flexion, wrist extension, hand open, and hand close. A set of time domain features—the Hudgins set—is used, which includes MAV waveform length, number of slope sign changes, and zero crossing rate [173]. Additionally sixth order autoregressive features are calculated for each channel from 250 ms sliding windows with a 50 ms frame increment. Finally, a linear discriminant analysis (LDA) classifier is trained using features extracted from the training contractions. The user is then able to use the classifier to direct three degrees of freedom in a virtual prosthetic arm. During real-time control the LDA classifier successfully predicted which motion class the user wished to generate from newly produced sEMG features and the corresponding velocity output to the virtual arm is made proportional to the mean sEMG amplitudes produced and normalized by motion class [174].

This experiment demonstrates that eight Myonode devices can be wirelessly powered simultaneously using an anti-Helmholtz transmitting coil with a power output of less than 1 W. The usability of the retrieved data is exemplified through successful

categorization of seven different motion classes using established myoelectric prosthetic control algorithms. Figure 3.25 shows an image of the experimental setup for multi-channel sEMG acquisition and control of a virtual arm.

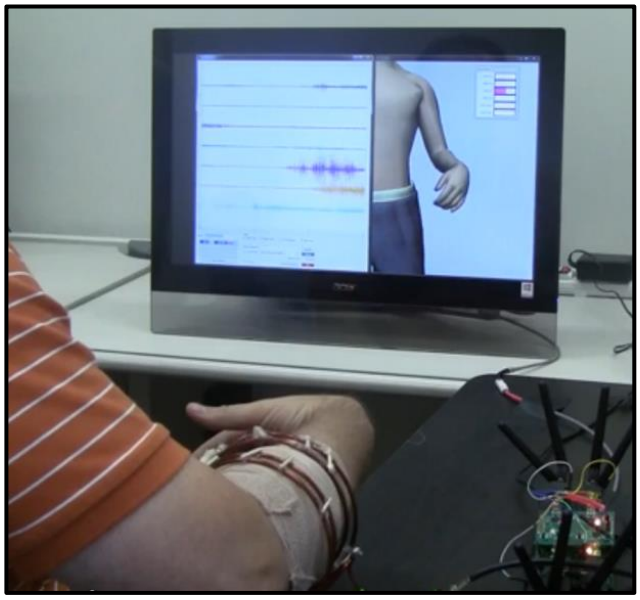

Figure 3.25 Experimental setup for multi-channel sEMG collection from an able-bodied subject. Data are collected from eight Myonode devices integrated on a fabric forearm cuff and powered through a wireless power transfer (WPT) link utilizing magnetic resonance coupling (MRC). Data are classified in real-time using a pattern recognition control system which is subsequently used to direct three degrees of freedom in a virtual arm.

This experiment offers the following key result: that multiple Myonode devices can be successfully powered in an eight-channel array while retrieving usable EMG. The eventual goal of this project is to collect motor control information from within the muscle, which will require further reduction in the dimensions and an alternative packaging strategy. It is worth noting that the Myonode in its current form may offer

some benefit to sEMG-modulated prostheses that are presently issued to patients. Specifically, multiple Myonode devices might be embedded in prosthetic sockets or elastomeric liners in order to wirelessly collect sEMG. This might simplify the patient-prosthesis interface by removing all rigid electrical connections between the prosthesis and the electrodes. The Myonode would serve as a wireless preamplifier connected directly to the electrodes and close to the signal source and it would telemeter the sEMG data to the processor rather than sending it through a rigid adapter. This would lessen restrictions on how the prosthesis is designed and mounted. Moreover, it would eliminate the chance of an electrical failure or interruption due mechanical stresses and failures. Lastly, it would significantly streamline the use of elastomeric liners, which can improve suspension of the prosthesis and the electrode-skin contact [175].

The potential uses for the Myonode in prosthetic control are not limited to upper-limb amputees. Lower-limb amputees are an important patient population to consider as they significantly outnumber upper-limb amputees [174] and EMG collection has been shown to improve control of powered prosthetic legs [176, 177]. Lower-limb amputees could benefit from chronic, wireless imEMG recording for many of the same reasons as upper-limb amputees (higher signal selectivity, signal permanence, etc.), but also because sEMG recorded in lower-limb prosthetic sockets contain substantial motion artifact caused by heel-strike [178]. This issue could be negated by permanent recording channels implanted in the residual muscle.

3.6 Conclusion

The Myonode represents the first pass at a fully wireless and implantable bioelectric sensor for freely behaving mice. One implementation of the Myonode attempts to build the functional circuit blocks in CMOS in hopes of benefiting from the smaller size and power consumption that come with ASIC-based systems. This resulted in a circuit that is capable of recording and transmitting bioelectric data on a power budget of 1 mW, but suffered from an overwhelmingly low production yield, difficulties interfacing with the ASIC chip, and functional rigidity. A second, more successful, implementation of the Myonode is designed and built using commercial off-the-shelf ICs and passive components integrated on a custom-designed PCB. This results in a finished device which is larger and demands more power than the ASIC. However, the additional size and power draw are counterbalanced by significant benefits such as configurability, customizable firmware, quick prototyping, and—most importantly—use of cutting edge microelectronics. This takes advantage of the state of the art in circuit design as well as quality control procedures already in place for commercial ICs, assuring greater reliability of the end-product.

The Myonode is designed specifically for EMG collection and is used to observe voluntary evoked muscle activity from a wild-type mouse and spontaneous aberrant muscle activity in a mouse model for familial MD. These are exciting outcomes as they demonstrate that the device is capable of collecting useful metrics for tracking neuromuscular diseases over time (see Section 1.1.1). It also affirms the viability of MRC power transfer to receiving devices implanted in freely behaving animals. Additionally, a

known and repeatable CMAP waveform is measured to validate the *in* vivo data digitized and transmitted by the Myonode. This stimulus evoked response is collected mid-surgery while the animal is under anesthesia. However, CMAP responses are needed to normalize voluntary muscle activity in each animal over time in a longitudinal study. The amplitude of the CMAP response itself can also be an indicator for muscle atrophy [23]. A single channel of EMG is sufficient for a proof of principle, but a more advanced instrument is needed to accurately interpret changes in muscle behavior over time. For this reason the fully implantable device will need an integrated stimulator to evoke the CMAP and be tuned appropriately to measure the CMAP.

Chronic electrophysiology in freely behaving animals faces many of the same obstacles as chronic electrophysiology in humans for prosthetic control. For this reason the work that went into developing an implantable system for mouse work also offered an opportunity to contribute to amputee rehabilitation. The human clinical work reported in this chapter includes three important results: 1) The Myonode is able to record usable imEMG, making it functionally suitable for intramuscular electrodes; 2) multiple Myonodes can be simultaneously powered to generate eight usable channels of sEMG; and 3) the Myonode in its current form could improve the interface between current socket liners and prosthetic sockets by using it as a permanently integrated preamplifier. The immediate utility of the Myonode for elastomeric liners as well as the Myonode's compatibility with a more flexible and efficient WPT strategy (MRC) represent advancements in neural interfaces for prosthetic control.

The next phase of this work will expand the capabilities of the Myonode and tackle its critical limitations. These limitations include single-tasking, weak mechanical properties of the electrode interface, and the small WPT testing environment. These fixes and new features result in a more sophisticated and versatile device termed the Bionode—the development and application of which is the subject of Chapter 4.

CHAPTER 4. THE BIONODE: A FULLY IMPLANTABLE RECORDING AND STIMULATING DEVICE FOR LONG-TERM SMALL ANIMAL MONITORING

4.1 Introduction

The material presented in this Chapter incorporates content from the journal article “Bionode for Fully Wireless Recording and Stimulating of Bioelectric Events in Rodents within a Large Volume Cavity Resonator” by R. A. Bercich*, S. T. Lee*, D. J. Pederson, Z. Wang, M. A. Arafat, H. Mei, C. Quinkert, G. Albors, J. P. Somann, J. G. R. Jefferys, and P.P. Irazoqui, which has been submitted for publication to IEEE Transaction on Biomedical Engineering. This chapter also incorporates content from the journal article “Cavity Resonator Wireless Power Transfer System for Freely Moving Animal Experiments” by H. Mei, K. A. Thackston, R. A. Bercich, G. R. Jefferys, and P. P. Irazoqui, which has been submitted for publication to IEEE Transactions on Biomedical Engineering. All procedures involving live animals are reviewed and approved by the Purdue Animal Care and Use Committee.

The development and application of the Myonode device—a fully wireless and implantable single-channel bioelectric sensor—is detailed in Chapter 3. This chapter is dedicated to the development and application of the Bionode, which evolved from the Myonode. Functionally and practically the Bionode greatly improves upon the Myonode, but there are five key advancements that make the Bionode amenable to a wide range

of electrophysiological studies and truly state-of-the-art for fully wireless animal monitoring. First, it has an integrated biphasic, current-controlled stimulator for precise evocation of biopotentials. Second, it offers two independently configurable recording channels. Third, the electrode interfaces are fully redesigned for reusability as well as improved mechanical and electrical stability. Fourth, it is enabled with bidirectional telemetry for open communication between the implanted device and an external base station, which allows for immediate changes to functional protocol and stimulus directives. Lastly, the Bionode is compatible with a large, resonant cavity WPT environment which affords more space and flexibility for freely behaving animal experiments. These advancements along with some minor improvements to the system are described in Sections 4.2 through 4.4.

The Bionode device described in this chapter reflects the end result of three design iterations. The first iteration used single supply mode on all microelectronics and a high side stimulator (meaning that both output electrodes are driven to high voltages that are disparate in amplitude by the product of current and electrode impedance during stimulation). The second iteration addressed stimulus artifacts that occur on startup due to improper default switch configurations within the stimulator circuit as well as high amplitude, transient current spikes that would occur at the onset of each stimulus pulse as a result of switching noise. The third iteration moves segments of the AFE and stimulator into dual supply mode and implements a low side stimulator to address current shunting to the AFE inputs, which causes sustained saturation of the recording channels during stimulation.

Recent progress in cavity resonator-based WPT system lead by Henry Mei has produced large volume animal testing environment that itself serve as a magnetic field source and container The cavity resonator is designed to maximize PTE through optimal impedance matching in a manner similar to the MRC power transfer method employed for the Myonode [70, 71]. The electrical and physical characteristics of the cavity dictate its resonant frequency and thereby the operation frequency of the WPT link. The resonant cavity used in this work is 60 cm x 60 cm x 30 cm and is made out of sheet aluminum (thickness = 1.6 mm), which results in a resonant frequency between 340 and 350 MHz. This is an important point because the higher operation frequency (relative to that of the coil pairing used for WPT to the Myonode) allows the size of the receive coils to be reduced while maintaining similar PTE performance. This is a wonderful piece of enabling technology as it improves two conditions of the Myonode system: the restrictive size of the animal monitoring environment and the coil size, which is cumbersome at 1.2 cm.

The Bionode consists of a power module board and a core module, which has all of the microelectronics needed for biopotential acquisition, neuromodulation (stimulation), and bidirectional telemetry. Temperature sensing is also enabled through the incorporation of a thermal sensor. The power module board and the core module are separate PCBs which are assembled individually and then stacked to minimize the footprint of the Bionode at the expense of increased thickness. The Bionode is designed strategically so that it can take advantage of WPT using the novel cavity resonator system. This includes the integration of a-biaxial receive coil system (two receive coils

oriented in transverse planes) on the power module to minimize sensitivity to misalignment between the receiving device and magnetic field direction. The profile of the magnetic field ($\vec{H}$) within the cavity is characterized by its TM_{110} resonant mode and circulates about the feed point in its center [71]. The use of this cavity and its adaptation for longitudinal collection of neuromuscular information in mice is detailed within the experimental design and methods for chronic mouse work in Section 4.7.1.

Sections 4.6 and 4.7 detail the use of the Bionode within a series of acute and chronic experiments in both rats and mice. These experiments serve importantly to demonstrate device *in vivo* viability and data validity. More excitingly, though, they include the application of the Bionode to the study of neuromuscular and motoneuron disease mechanisms. The ability to use the Bionode to expose new information about clinically relevant disease models is an exciting end result to this engineering design challenge.

4.2 Power Module Development

The power module acts as a power supply by coupling RF energy sourced from a large cavity resonator and rectifying the induced voltage to DC. Orientation mismatch of the transmitter and receiver is a notorious problem for freely behaving animal experiments. While the resonant cavity solution has improved performance compared to conventional WPT systems, it is not immune. To lessen the effect of device orientation as a result of animal movement on PTE, two perpendicular copper coils are

connected to the power module: each with a separate optimally designed impedance matching circuit. The methodology of the optimal impedance matching for the cavity is described in [71].

4.2.1 Circuit Design for Power Management

Figure 4.1 shows a circuit diagram of the full power module board. The inputs to this circuit are two AC voltages induced in the receive coils. These each pass through their own J-inverter impedance matching network before both are rectified and summed by a voltage doubler. This constitutes a biaxial RF-to-DC conversion circuit. This rectified voltage is fed to a bank capacitor (68 μF capacitance) which stores excess charge in a kind of reservoir. This storage capacitor serves to buffer the power supply lines during periods of elevated current consumption such as ADC sampling or data transmission.

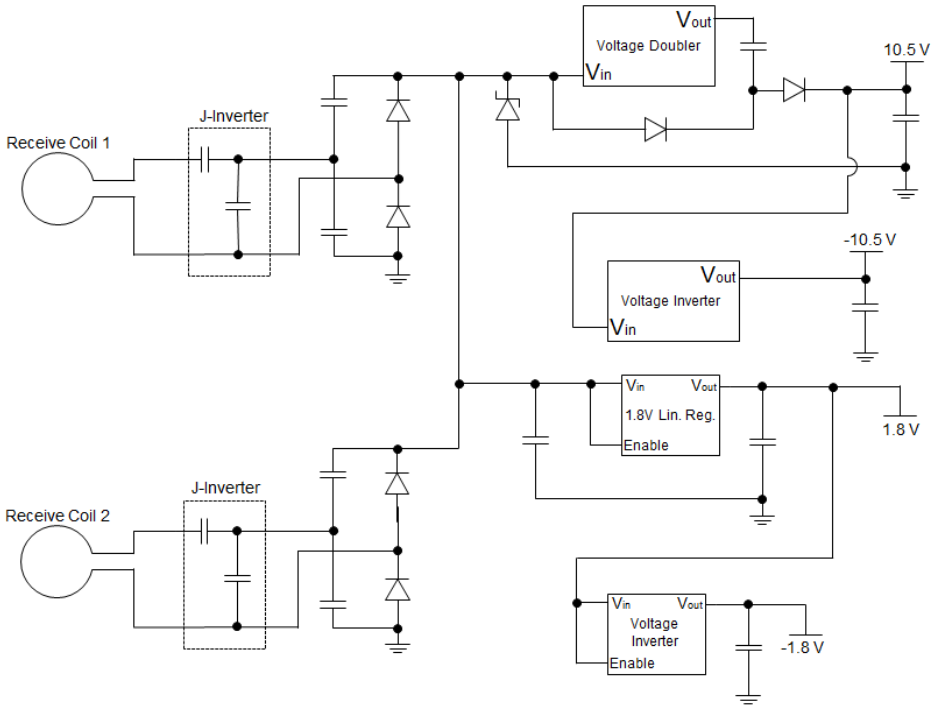

Figure 4.1 Circuit schematic of the Bionode's power module board. AC voltages induced in two receive coils by incident RF fields are passed through impedance matching networks (J-inverters), rectified, then regulated to the four voltage supplies needed for dual supply operation of the Bionode's analog front-end (AFE) and stimulator.

The unregulated, rectified voltage is also surge protected by a 5.1 V Zener diode. The rectified voltage is then applied to a network of voltage regulators and inverters which output all the necessary power supplies for the main PCB. This network includes a low-dropout (LDO) linear regulator to produce a 1.8 V supply (VDD) used by the AFE, stimulator, and MCU. This supply is subsequently inverted by a switched capacitor voltage inverter (MAX1720, ON Semiconductor) to create a -1.8 V supply (VSS) for the AFE and stimulator. The rectified voltage is also doubled using another switched capacitor voltage converter (TL7660, Texas Instruments) to generate a larger voltage

headroom for the stimulator. The 5.1 V Zener diode on the rectified voltage limits the output of the voltage doubler to 10.2 V in theory and 10.5 V in practice. A second TL7660 is placed in series with the first and configured as a voltage inverter rather than multiplier to generate the -10.5 V supply for the stimulator.

The power module has a footprint of 8mm x 13.5 mm and a thickness of 0.56 mm (unpopulated). The four-layer PCB is designed in Altium and fabricated by Advanced Circuits using on FR-4 substrate. Once the microelectronics have been assembled on the power module, it is stacked and electrically connected by wires to the core module using five connection points (VDD, VSS, 10.5 V, -10.5 V, and ground). A picture of the assembled power module is shown in Figure 4.2.

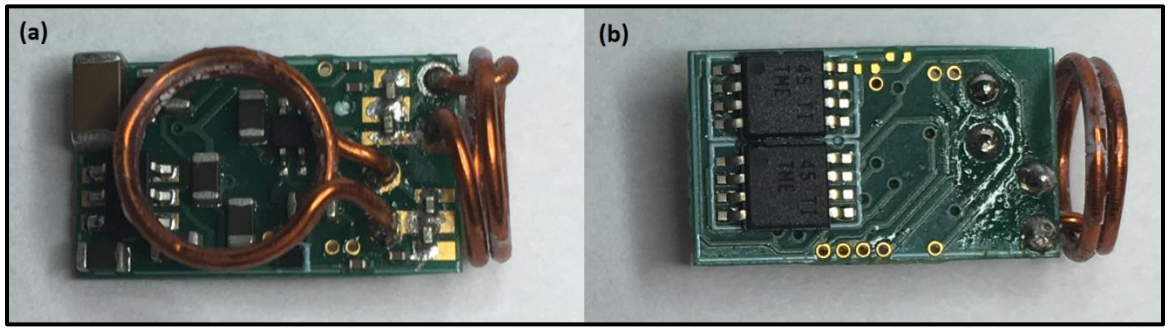

Figure 4.2 (a) Front view and (b) back view of assembled power module PCB board with 5 mm diameter biaxial receive coils. Footprint dimensions are 8 mm x 13.5 mm.

4.2.2 Flexible Substrates for Power Module Boards

An alternative to the rigid power module is designed using copper deposited on a polyimide substrate with a polyimide coverlay in a manner similar to the flexible coil

fabrication discussed in Section 3.3.3 and is shown in Figure 4.3. This has three key advantages: 1) It reduces the power module board thickness by over 400%, which decreases the total thickness of the device; 2) the flexible coil is able to conform to the shape of the body once implanted, which makes it less of an obstruction than rigid coils; and 3) the receive coil is continuous with the circuit board, reducing the chances of a mechanical failure from a soldered joint at the coil terminals. The flexible power module is used for one iteration of the Bionode as shown in Figure 4.4. It is not used in the final Bionode design owing to changes in the power module circuit to accommodate a dual supply mode as well as difficulties incorporating a second printed coil for the biaxial receive coil system.

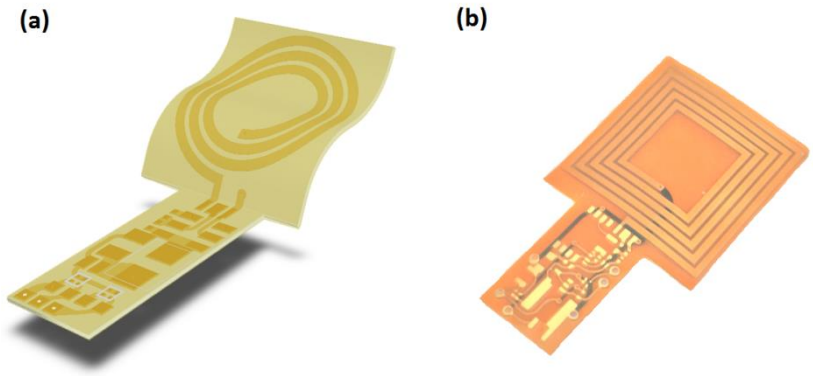

Figure 4.3 Flexible power module fabricated from a flexible polyimide substrate with a thickness of 013 mm with an integrated. (a) Rendering of power module in Altium with a round receive coil and (b) Photograph of fabricated power module with a 15 mm square coil.

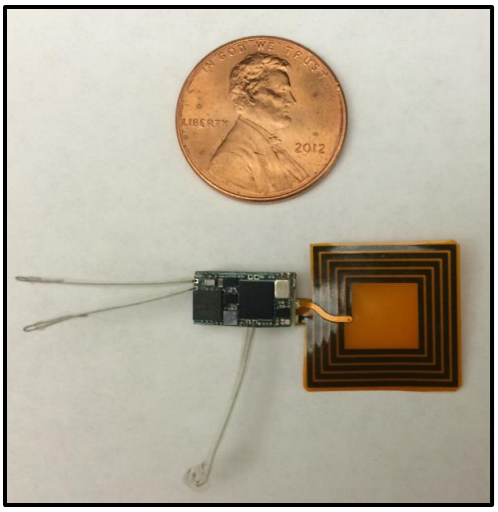

Figure 4.4 Bionode core module stacked on top of a flexible power module board.

4.3 Bionode Core Module Development

The purpose of the Bionode's core module is to integrate the microelectronics for biopotenial acquisition, neuromodulation, thermal sensing, and telemetry. The power supplies for all core module microelectronics are provided by the power module board (see Section 4.2). The same Nordic Semiconductor SoC that is used in the Myonode is used on the Bionode's core module to run and coordinate its various tasks. The SoC has 256 kB of flash memory which, once again, allows for rapid changes to the device's protocol through reprogrammable firmware.

Wireless communication between the Bionode's core module and a user interface for saving data and changing the device's functional parameters is facilitated by a base station. The communication protocol, firmware development, and base station design are the results of incredible work done by Dan Pederson and Zhi Wang: two members of the Center for Implantable Devices at Purdue University. Briefly, the Bionode sends

recorded data points, stimulation circuit status, and thermal measurements to the base station. During the normal data collection phase, the Bionode digitizes data from each recording channel using the SoC's integrated ADC. The ADC can be set to collect data using either 8- or 10-bit precision. Once 40 bytes of data have been acquired, the Bionode sends a wireless data packet to the base station.

Multiple settings and instructions can be communicated in the opposite direction—to the Bionode—through update packets sent by the base station to the transceiver embedded in the SoC on the Bionode's core module. Configurable settings include recording parameters (sampling rate, ADC digital resolution, and selection of ADC input channels) and stimulation parameters (amplitude, pulse width, frequency, duration, and calibration settings). Instructions to begin or end a stimulation session as well as update the temperature measurement are also permitted.

4.3.1 AFE for Biopotential Recording

Topologically the AFE on the Bionode is very similar to the AFE on the Myonode (see Section 3.3.1) and consists of an instrumentation amplifier (first stage) followed by a higher gain second stage and bandpass filter. Figure 4.5 displays the circuit diagram for the Bionode's AFE, which has undergone three changes since the Myonode: first, the instrumentation amplifier is run in dual supply mode; second, the reference voltage is generated by a resistor divider rather than a regulator; and third, an alternate second stage op amp IC is used.

The transition from single supply to dual supply eliminates the need for pull-up resistors to maintain a common mode, mid-supply, DC bias on the inputs to the instrumentation amplifier (first stage). This greatly increases the input impedance of the recording channels, which equates to twice the pull-up resistance in the Myonode since both input are tied to the same reference voltage for DC biasing. Alternatively, this topology takes advantage of the high differential impedance (100 GΩ) of the INA333.

The input voltage range for the ADC on the Myonode is 0 to 1.8 V: a setup made possible by prescaling the analog input to the MCU. Prescaling puts limitations on the sampling rate and is not used in the Bionode where the ADC still operates in single supply mode but uses the default input voltage range of 0 to 1.2 V. Therefore the AFE output must still be offset to the middle of the ADC input voltage range. Here the AFE takes advantage of a 1.2 V reference voltage readily available from the digital-to-analog convert (DAC) that is introduced to the system as part of the stimulator circuit. This 1.2 V reference is voltage divided in half using equal valued resistors (R3 and R4 in Figure 4.5) and buffered to create a low impedance source.

The second stage op amp is the OPA313 (Texas Instruments), which has a higher gain-bandwidth product (1 MHz) than its predecessor. This lessens the limitations on the low-pass filter cutoff and allows it to be raised to 10k while maintaining that a majority of signal gain occurs in the second stage (typically 40 dB). This makes the recording channel more suitable for general neural recording since single unit potentials from individual nerves, muscle fibers, and neurons have frequency content in the range of several kHz [179].

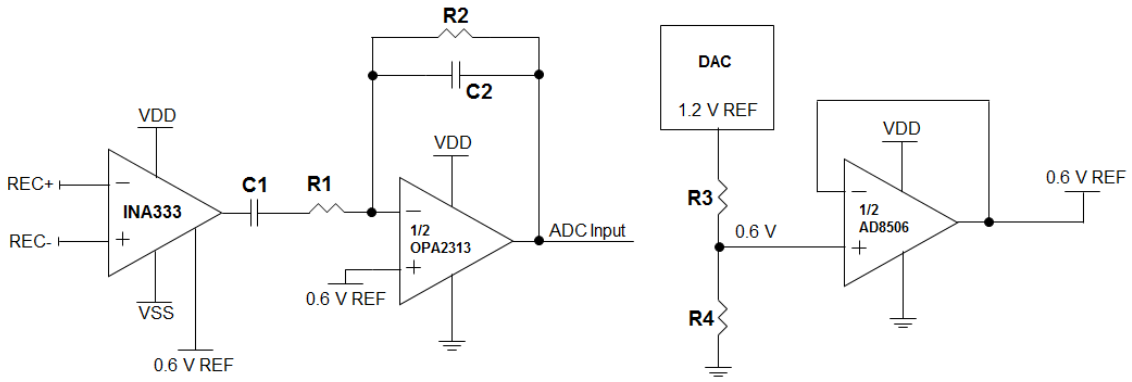

Figure 4.5 Bionode analog front-end (AFE) circuit diagram. Instrumentation amplifier (first stage) is followed by a higher gain second stage with an integrated bandpass filter. A reference of 0.6 V is needed to bias the AFE output to the middle of the ADC input range. This reference comes from the digital-to-analog converter(DAC) following voltage reduction through a resistor divider.

The Bionode contains two independent recording channels. The gain and bandwidth of each channel's AFE can be reconfigured through passive component selection. The gain of the first stage is set by a single resistor, Rf, based on the relationship given in [164] while the gain of the second stage may be approximated by the known gain equation of an inverting operational amplifier (see equation 3.1). Meanwhile, the bandwidth cutoffs may continue to be approximated by equations (3.2) and (3.3) and verified using SPICE software for circuit simulation. The passive component values selected in order to achieve the appropriate gain and bandwidth for bioelectric activity of the peripheral nerves and muscles in mice are recorded in Table 4.1.

Table 4.1 Passive component values used in Bionode analog front-end (AFE) for neuromuscular target signals in mice.

Target Signal	***Total AFE Gain***	***Rf***	***C1***	***R1***	***C2***	***R2***
CMAP	60 dB	11 kΩ	1 µF	10kΩ	20 pF	1 MΩ
Spontaneous EMG and NAP	34 dB	25 kΩ	1 µF	10 kΩ	330 pF	100 kΩ

The frequency response for each of the two anticipated AFE configurations is simulated in TINA-TI and shown in Figure 4.6. The gain of each channel must be selected carefully since the Bionode does not have the ability to adjust gain after implantation. Gain is selected for each channel based on results from *in vivo* experiments outlined in Section 3.4 as well as within the literature [23]. Given the demonstrated capability of maximum CMAP responses to exceed peak-to-peak amplitude of spontaneous EMG activity by at least an order of magnitude, it is not judicious to use the same channel to target both signals until adjustable gain is integrated. Rather, one channel should be used specifically for CMAP responses and another for spontaneous EMG or NAP. The Bionode's AFE has a CMRR of at least 80 dB from DC to 60 Hz and an input referred noise of 2.73 μV_{pp}, which are measured using the same methodology outlined in Section 3.3.4.

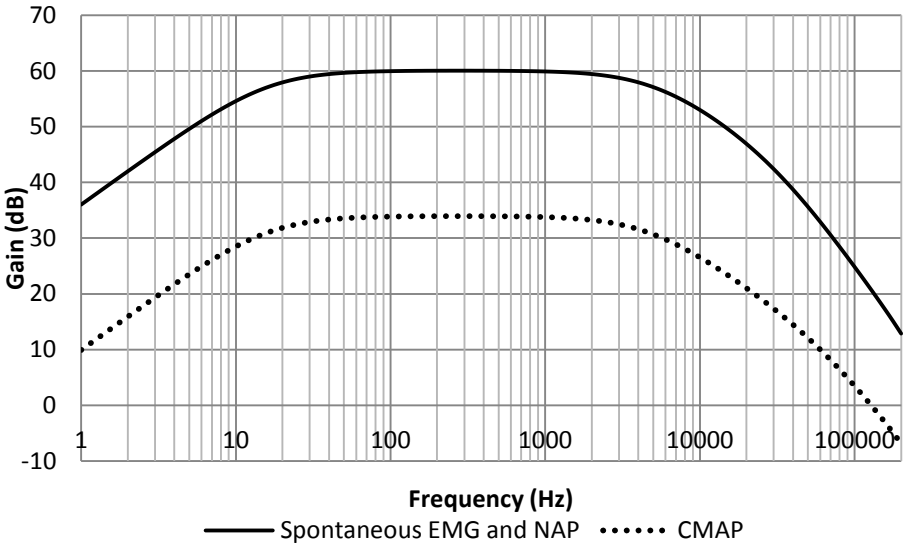

Figure 4.6 Simulated frequency response of the analog front-end (AFE) configured for spontaneous EMG and NAP (solid line) and CMAP (dotted line).

4.3.2 Current-Controlled, Biphasic Stimulator

The first step to integrating a stimulator on the Bionode is selecting the mechanism by which charge will be precisely injected into the excitable tissue. Voltage-controlled (potentiostatic) stimulation is certainly easier to implement and, as demonstrated by Simpson and Ghovanloo, more power efficient than current-controlled (galvanostatic) or charge-controlled (switched-capacitor) stimulators [180]. However, a voltage-controlled stimulator presents a critical limitation which is that it offers no command over the level of current applied to the system. This is an issue because the electrical model of the tissue-electrode interface includes a capacitive element on account of the Helmholtz double layer which is forms between electrodes and extracellular fluid. This means that each pulse will begin with a phase of rapidly decaying

capacitive current and then approach a more stable Faradaic current. This means that the current amplitude at any time during a stimulus pulse will be dependent on the properties of the electrode and impedance between the working and counter electrode (which is likely to change over time as scar tissue forms in and around a cuff electrode placed on a nerve). Since the level of depolarization—and thus the electrophysiological response—of an electrically excitable tissue membrane is directly related to the amplitude of the current, an absence of this information makes it extremely difficult to reproduce and compare results from different animals [181]. For this crucial reason, a current-controlled rather than voltage-controlled stimulator is selected for the Bionode.

The recommended parameters for electrical stimulation are well characterized and include biphasic pulse generation for charge balancing. This allows for the reversal of electrochemical processes that occur during a stimulating pulse, which helps to prevent electrode degradation and resulting deposition of chemical species into tissue [181]. Other stimulation parameter such as frequency, pulse width, and pulse pattern distribution are not as well studied and are of interest for biological efficacy and decreased power consumption in the recently burgeoning field of electroceuticals [182, 183]. While outside the scope of this work, it is exciting to note that the Bionode and its supporting hardware and software constitute a streamlined and comprehensive platform for testing these additional parameters for functional electrical stimulation and other therapeutic devices.

Figure 4.7 shows a circuit diagram of the biphasic, current-controlled stimulator designed for the Bionode. Credit is due here to Muhammad Arafat, a student in the

Center for Implantable Devices at Purdue University, who helped to develop the stimulator topology in its current (dual supply) form. The output current to a stimulating (working) electrode (designated STIM in Figure 4.7) is achieved using an op amp constant current sink with parallel N-channel and P-channel MOSFETs for generating either positive or negative current. The time-dependent features of the stimulus output (pulse width and pulse period) are regulated by a single pole triple throw (SP3T) switch that selects between an off-state (output connected to ground) and two possible on-states: one for a negative (cathodic) pulse and another for positive (anodic) pulse relative to a counter electrode that is connected to circuit ground. All stimulation parameters (rate, pulse width, and amplitude) are controlled by protocols in the MCU.

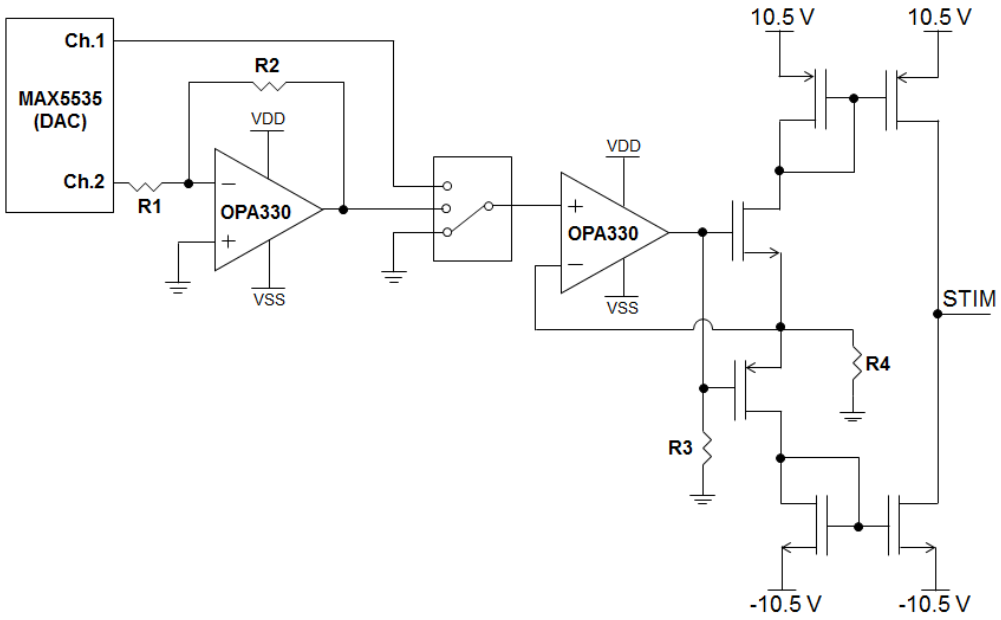

Figure 4.7 Circuit schematic of the Bionode's biphasic, current-controlled stimulator. Both positive and negative stimulus pulses may be applied to the STIM node, which is connected to a working electrode. Stimulus current is collected by a counter electrode shorted to circuit ground.

The current amplitude during each stimulation phase is determined by a programmable control voltage generated by a 12-bit DAC (MAX5535, Maxim Integrated) either directly (for anodic pulses) or following a unity gain voltage inverter (for cathodic pulses). The inverting op amp, which operates in dual supply mode, is needed since the DAC (operated in single supply) cannot output negative voltages. The control voltage is applied to the non-inverting terminal of an op amp during a stimulus pulse, which will drive the inverting input to the same voltage. The voltage on the non-inverting input is applied across a known resistor—R4 in Figure 4.7—to create a constant current sink with a current amplitude easily derived from Ohm's Law (equated to the control voltage

divided by R4). The resistor R4 is set to 200 Ω by default and for all applications in this work.

The current through R4 is replicated by current mirrors using matching P-channel MOSFETs (UM6K34N, Rohm Semiconductor) or N-channel MOSFETs (NX3008PBKS, NXP Semiconductors), depending on the direction of the current. This allows for isolation between the portion of the circuit that sets the desired current and the portion of the circuit that applies the desired current to the tissue. The matched current is directed to the working electrode (STIM) and collected by a counter electrode referenced to circuit ground. One disadvantage of this topology is that it requires a very close match in MOSFET characteristics within each current mirror in order for the applied current to match the set current through R4. Even though the MOSFETs selected for the current mirrors are identical parts that even come in the same package, the relationship between desired and applied current is non-linear and varies from build to build.

The same non-linearity is observed —to a lesser extent--in stimulus pulse width. Lower stimulus currents necessitate a more dramatic positive calibration in the pulse width. Figure 4.8 compiles stimulator calibration curves for four different stimulator builds at a desired pulse width of 100 μs. Blue traces represent positive pulse calibration and red traces represent negative pulse calibration. Pulse amplitude correction, which is indicated by solid traces can range from -50 to +146 μA for positive pulses and from -80 to +6 μA for negative pulses. Pulse width correction for both negative and positive pulses becomes less dramatic at higher current amplitudes; however, they are significant in the lower range of requested current amplitude where correction may be

as high as +50 µs (half the pulse width setting). The implication of Figure 4.8 is that the stimulator topology implemented on the Bionode can supply predictable and reliable stimulus waveforms provided that each stimulator build has been characterized and is accompanied by its respective calibration data. This is an inconvenience but not an obstruction to the application of this device to animal work.

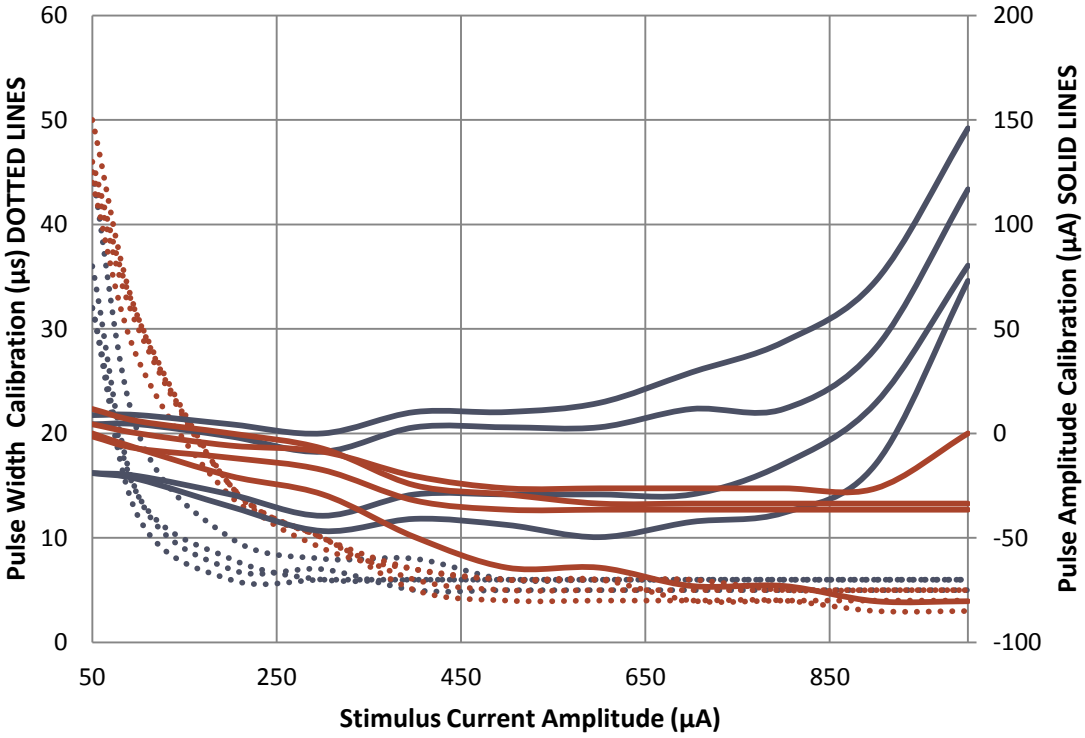

Figure 4.8 Stimulus pulse width (dotted lines) and amplitude (solid lines) calibration curves for correcting nonlinearity between requested and actual parameters of positive (blue) and negative (red) stimulus pulses. Requested pulse width is 100 µs.

The functional performance of the stimulator is evaluated on the bench top by connecting its output to a known load impedance (10 kΩ), sweeping the stimulator's functional parameters (pulse width, current amplitude, and pulse repeat time/duty

cycle), and calibrating the pulse width and current amplitude at each set of stimulation parameters. Figure 4.9 illustrates a sampling of the biphasic stimulator outputs for a range of stimulus current amplitude settings at a 50% duty cycle. When optimally calibrated, the measured charge balance error is less than 1% at a pulse width of 100 µs. This is calculated by integrating the current through a 10 kΩ resistor during 200 successive stimulus pulses (alternating between anodic and cathodic) Dividing this integral by the number of pulses gives the average net charge imbalance per pulse pair.

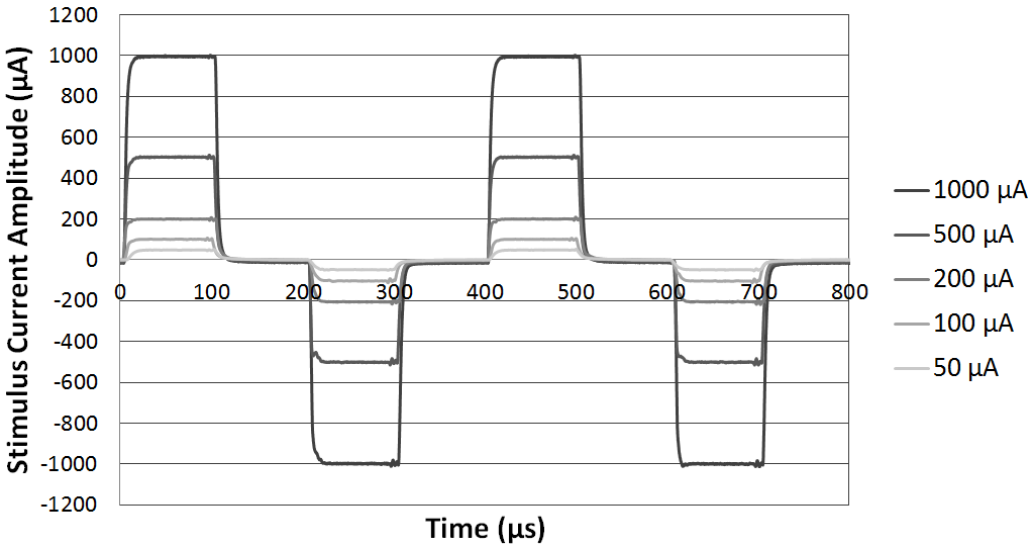

Figure 4.9 Current-controlled, biphasic stimulator output measured on the bench top using a 10 kΩ load between the working electrode and counter electrode (ground). Pulse width, current amplitude, and duty cycle are all selectable in real-time telemetry from the base station to the Bionode. A pulse width of 100 µs and a 50% duty cycle are used here to illustrate the measured output current for a range of amplitude settings.

A significant challenge that appears repeatedly across iterations of the Bionode is the propensity for erroneous stimuli during power up. These ultimately result from a

delay between initial generation of the electromagnetic field and control of digital logic lines to the switch that controls the phase (on or off) of the stimulator. This means that the logic lines that designate switch position (see Figure 4.7 for an example) float to unknown and likely high voltages on account of high line impedance before the MCU is able to startup and carry out its programmed protocols, which include regulating the voltages on these digital I/O lines. This issue is exacerbated by the relatively long (compared to the other ICs on the core module) MCU startup time, which is over 100 ms when powered from an ideal DC voltage supply. However, the delay between initial voltage rise on the power supply line and MCU startup can increase dramatically as a result of variable rise rates and possible fluctuations on the main voltage supply line; both of which can occur unpredictably with WPT to a freely behaving animal.

Consider the following likely scenario: an electromagnetic field source is turned on and couples energy to a receiving device within the cavity resonator. The induced AC current is continuously rectified, which causes an increase in the rectified voltage as its storage capacitor is charged. Once the rectified voltage reaches approximately 1.2 V, the 1.8 V LDO regulator will turn on and follow the input (rectified voltage) as it increases up to 1.8 V. Once the LDO regulator turns on (at a rectified voltage as low as 1.2 V) current will travel to and diffuse throughout the Bionode, partially turning on some ICs and possibly inducing transient elevations in electrical potential in extremely close, short, and high impedance traces. Simultaneously, as the DAC boots up (which will happen faster than MCU boot up), its output will float until it receives directives from the MCU. At the same time the digital logic pins for the switch on the output of the DAC are

unregulated and may float to a logic high condition that connects the control voltage from the DAC to the constant current sink. This results in erroneous and undesirable stimuli within tissue and has been observed both on the bench top and *in vivo*. Furthermore, this activity is erratic in nature, and so presents a challenge to the circuit design, which is often done under the easier but limiting assumptions of constant DC powering and steady state conditions.

This artifact is potentially catastrophic in situations where coupling between the resonant cavity and receive coils on the power module may not offer a sufficient PTE to run the device in all possible locations and positions of the animal. One can imagine a scenario in which the animal moves into a position such that the device is beginning to turn on when suddenly a large, unwanted stimulus is applied. This would likely cause the animal to move abruptly, causing a quick shift in voltage supply amplitude. This would, in the best case scenario, increase the supply voltage so the system continues to turn on and, in the worst case scenario, decrease the supply voltage and return to conditions in which the system is poised to deliver another unwanted stimulus. The likelihood of frequent, unwanted stimulation to the peripheral nerve in this case would likely lead to experimental confounds and unnecessary stress imparted on the animal. Even more disastrous to study outcomes is the possible behavioral conditioning that would result from a large and likely painful stimulus delivered every time the device turns on. This might cause the animal to avoid areas of its environment where WPT is adequate to power the device.

One solution that is implemented in the course of iterating the Bionode's core module is the use of pull-down and pull-up resistors on the switch logic lines in order to hold these to either high or low logic levels during startup at the expense of added current consumption during normal operation. The stimulator topology shown in Figure 4.7 is no exception to this matter as the SP3T switch has two digital logic lines directing the switch position. This switch is outfitted with a pull-up resistor to the positive voltage supply (1.8 V) on one digital pin for a forced logic high and a pull-down resistor to ground on the other digital pin for a forced logic low. This logic configuration ensures that the output of the switch is toggled to ground by default even when the device is starting up.

However, even when logic lines can be configured intelligently for startup as they have been here, there is still the possibility that another critical node in the stimulus circuit path will float to a non-zero voltage relative to circuit ground up until the point when all active components in the system are turned on and operating in steady state. This turns out to be the case for the assembled stimulator on the Bionode. Despite control over the digital lines of the phase switch, high amplitude currents can be measured on the stimulator output during startup. This reemerging problem is addressed by observing that the only way for current to flow through the single N-channel or P-channel MOSFETs on the output of the op amp is if the gate voltage is biased. The likely explanation here is that the output of the op amp, which operates in dual supply mode, runs positive for the short period of time between activation of the positive rail and subsequent activation of the negative rail. To understand why this

happens, recall that the-1.8 V supply voltage (VSS) is generated on the power module by a voltage inverter preceded and supplied by the 1.8 V LDO regulator than generates VDD. For this reason, the Bionode's core module will always see changes in VDD before changes in VSS during startup.

A pull-down resistor to ground on the gates of these MOSFETs is a simple and elegant way to stifle this unwanted bias voltage as it cuts the problem off at its source. The pull-down resistor (R3 in Figure 4.7) needs to be sufficiently small so that any voltage applied to the gates will readily discharge to ground. The size of this resistor is determined empirically by incrementally decreasing the resistance until the startup artifact disappears. The value of R3 is 1 kΩ for the extent of this work. This solution comes at very little expense since the op amp output is almost always 0 V under normal operation (no stimulation) and only increases total device consumption during the brief periods of stimulation. This does not noticeably affect the behavior of the stimulator itself because once the op amp is fully turned on it can source enough current to effectively bias the gate voltages as needed.

4.3.3 Thermal Sensing

The Bionode is equipped with a temperature sensor IC (TMP112, Texas Instruments) on the core module in order to monitor thermal changes within the device. Due to the position of the sensor on the surface of the core module PCB and the packaging strategy, which placed a barrier between the internal microelectronics and the external tissue environment, the sensor is not in direct contact with the device-

tissue interface. Rather, it sits adjacent to the heat source. This makes it difficult to compare temperature changes in the tissue to the appropriate safety thresholds and recommendations outlined in Section 2.5. However the temperature change measured by the sensor is more exacting than that experienced by the tissue because the temperature at the source will always be greater than the temperature experienced by the tissue. Resultantly, a limit may be imposed on the temperature rise at the source which automatically shuts down the device once an established threshold has been crossed. If this threshold is equated to maximum safe temperature changes in tissue, this would prevent tissue damage from thermal toxicity.

The fidelity of the temperature monitoring protocol is demonstrated in a controlled water bath. A packaged Bionode is submerged in the bath adjacent to a commercial thermocouple (Fluke 80BK-A Type-K). The Bionode's power supply terminals are wired out of the device and connected to DC power supply. Wireless powering is not desired in this experiment as it will likely cause local heating within the device as a result of electromagnetic field induction and voltage rectification. This would unnecessarily complicate the temperature gradient profile when the experimental objective is to confirm that the thermal sensor—as it is implemented and packaged—will accurately track known temperatures changes in its environment.

The temperature of the water bath is raised to 40 °C and then allowed to cool. During cooling the temperatures measured by the thermocouple and IC thermal sensor are recorded at a rate of one sample per minute. The results of this experiment are plotted in Figure 4.10. The offset between the temperatures measured by the thermal

sensor and the thermocouple over time is 0.525 ± 0.057 °C. These data suggest that there is a consistent DC offset in the thermal sensor measurements across the range of temperatures likely to occur near a subcutaneous implant in a rodent. This means that accounting for this offset in each device can be done using a simple, single-point calibration at a known reference temperature.

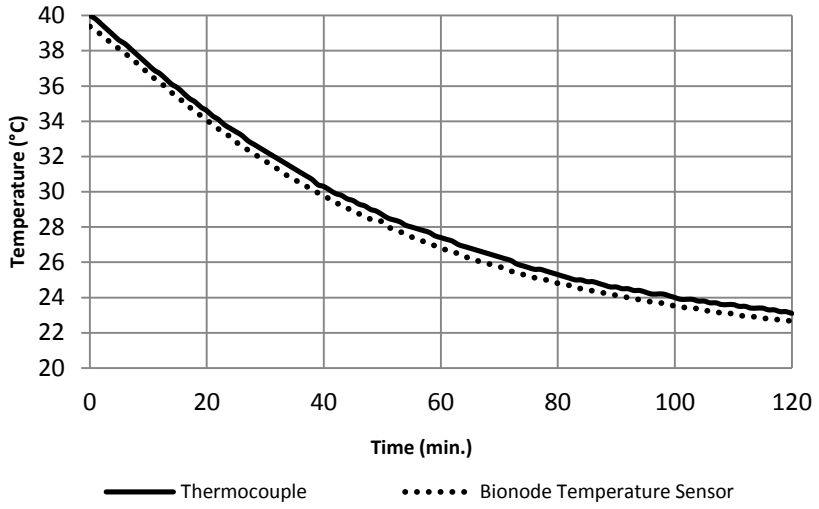

Figure 4.10 Comparison of temperature measurements from a thermal sensor IC (TMP112 mounted on the Bionode's core module PCB) and a commercial thermocouple tracking change in water bath temperature over time.

4.3.4 Custom PCB Design for Integration of Core Microelectronics

The microelectronics for the Bionode's core module are integrated on a six-layer PCB made from FR-4 substrate with thickness of 1 mm. This PCB is fabricated by Advanced Circuits and has a footprint of 8mm x 13.5 mm (the same as the power module). Given the unavoidable close proximity of the mixed-signal electronics, care is taken during layout tot physically isolate the analog, digital, and RF blocks of the

Bionode. Figure 4.11 shows front and back views of a core module PCB designed and 3D rendered in Altium as well as pictures of an assembled prototype.

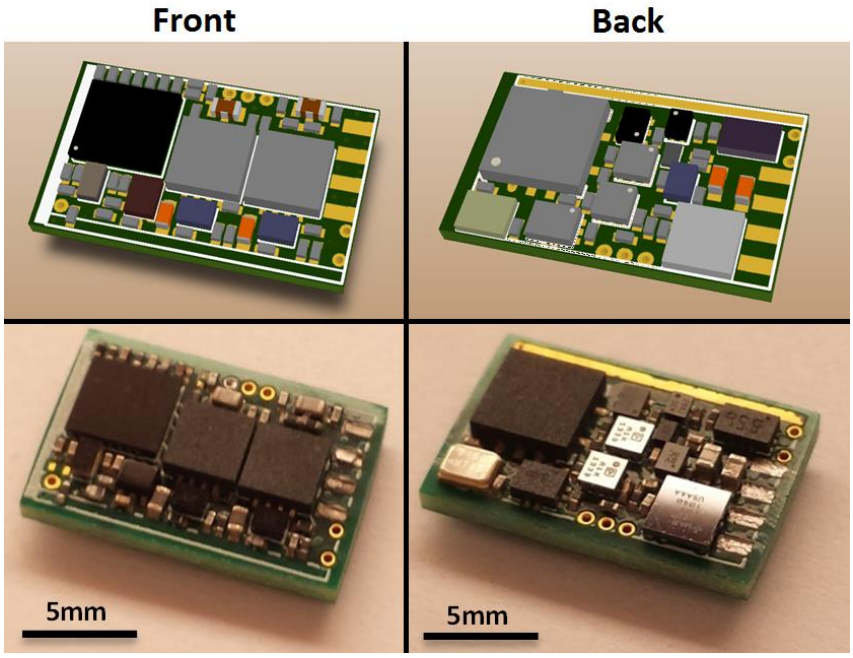

Figure 4.11 Front and back view of the Bionode core module rendered in Altium and fabricated on a custom PCB.

A monopole strip antenna for bidirectional telemetry at 2.4 GHz is printed on the bottom layer of the PCB and replaces the chip antenna that is used for the same purpose on the Myonode. Because of the RF communication frequency and the limited real estate, this antenna is inevitably electrically small. Electrically small monopole antennas exhibit better performance (measured in antenna gain) when the length of the antenna increases to approach a quarter wavelength at the frequency of operation. Consequently, the antenna is placed adjacent to the longer edge of the board to

maximize its length, which is 11.5 mm. The input to the antenna is impedance matched to maximize the power transferred to the antenna, which increases signal power and fidelity.

4.4 Bionode Full System Bench Top Characterization

The power and core modules together constitute the implantable system, which communicates wirelessly with an external base station. Figure 4.12 shows a block diagram of the complete hardware system that highlights the key functional blocks. In addition to two recording channels, one stimulating channel, and a thermal sensor, the device also offers two optional input channels which connect directly to ADC input pins on the SoC. These are included so that the Bionode device can be paired with other types of sensors. The external base station serves to route incoming data from the implant to a graphical user interface (GUI) for real-time viewing and data storage. The GUI also enables communication of directives such as sampling rate, ADC resolution, and stimulation parameters to the implant.

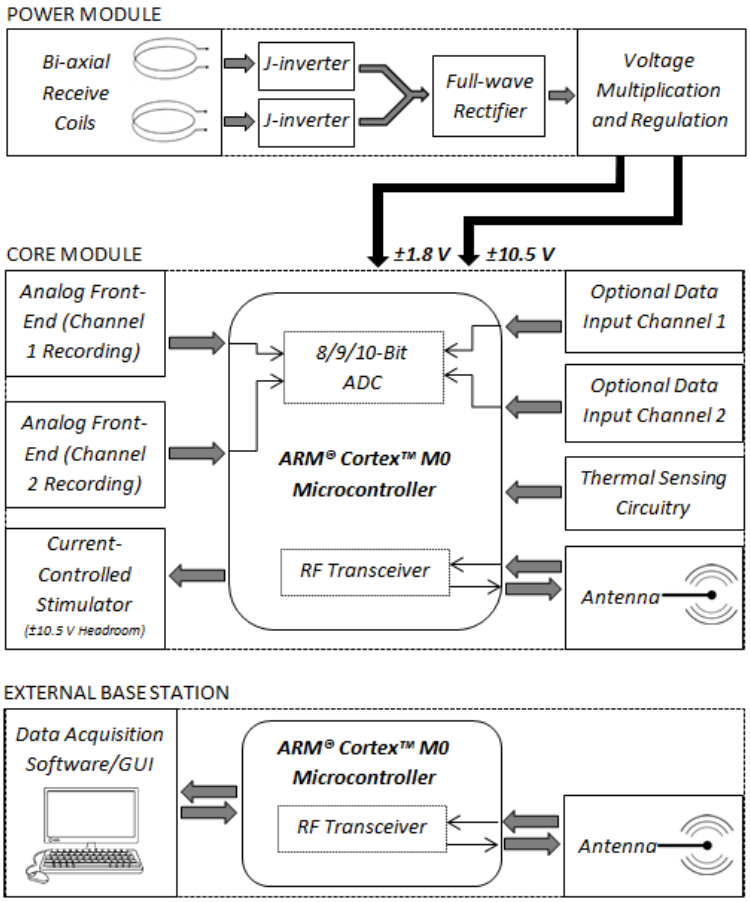

Figure 4.12 Block diagram illustrating key sub-elements of the fully Bionode system. The implantable Bionode device includes the power module board stacked on top of the core module board. The power module board provides the supply voltages necessary to run the microelectronics on the core module. The device is enabled with two-way telemetry with an external base station, which relays data to a computer. The graphical user interface (GUI) is written in Python3 and can be used to plot and save data. The GUI is also able to control functional parameters of the remote device such as sampling rate, ADC resolution, and stimulus waveform settings.

It is necessary to understand the cumulative power consumption profile of the Bionode in order to make inferences about the PTE of the WPT link once the device is operating in an animal. This information is also needed to select an appropriately sized storage capacitor for the rectified voltage on the power module. This is because certain

phases of the device's functional protocol (like sampling and transmitting) draw additional current for short periods of time. It is important that during these phases of elevated current consumption the supply voltages do not droop and initiate shutdown of any onboard ICs. The power consumption profile over time is compiled using a small-value (5 Ω) resistor in series with the each of device's voltage supplies and measuring the differential voltage across the series resistor over time. The current drawn from each supply is calculated using Ohm's Law and then all the individual currents are summed. Figure 4.13 illustrates the cumulative, temporal power consumption of the device when it is sampling at a total rate of 5 kHz. The average power consumption under these conditions is 5.03 mW. Figure 4.14 illustrates the total temporal power consumption of the device when it is sampling at a total rate of 25 kHz. The average power consumption under this condition is 6.72 mW.

The smaller spikes observed in Figures 4.13 and 4.14 are associated with ADC operation during data sampling. Also clear in these figures are much larger, sustained spikes that occur less frequently and are attributed to transmitter use. In both scenarios the ADC resolution is maintained at 8-bit, which means that after every 40 samples (small spikes) a larger spike should occur as the transmitter is turned on to send a packet of data as established by the telemetry protocol. This is confirmed by the matching count of small spikes between large spikes during both 5 kHz and 25 kHz sampling.

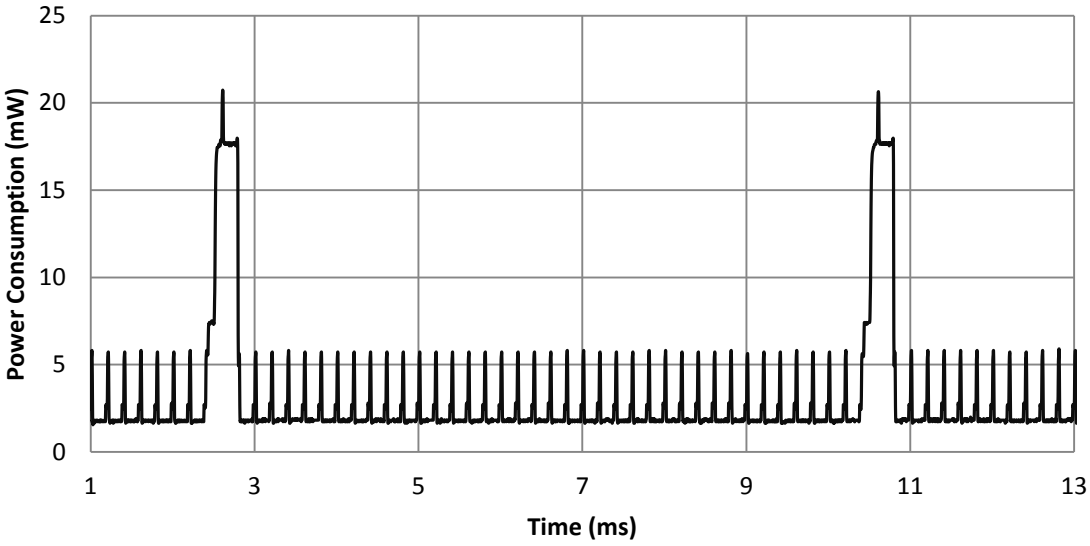

Figure 4.13 Power consumption profile of the Bionode over time when sampling rate is set to 5kHz and stimulator is off.

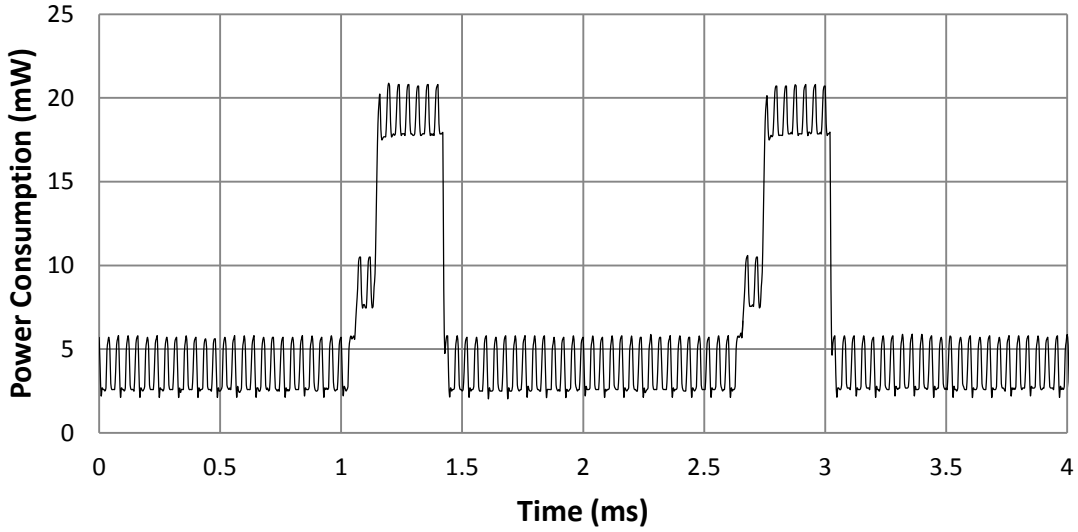

Figure 4.14 Power consumption profile of the Bionode over time when sampling rate is set to 25 kHz and stimulator is off.

The average power consumption is a useful metric for comparing this system to other bioelectric sensors (see Table 2.1), but doesn't by itself reveal the dynamic loading

conditions that must be considered when designing an effective power management strategy. It is established in Section 4.2.1 that the rectified voltage is limited to approximately 5.25 V in practice as a result of a 5.1 V Zener diode and that this rectified voltage is applied across a large storage capacitor that serves as a charge bank. Since the amount of charge stored in a capacitor is directly proportional its capacitance, it is desirable to make this capacitor as large as possible so that it can buffer periods of large current draw. This is especially important when the system has recently turned on and the rectified voltage may be just barely above the 1.8 V needed for stable operation of the most ICs—including the MCU. In this vulnerable state, rapid fluctuations on the power supply might cause the device to turn off and on repeatedly: prohibiting the collection of continuous data. A worst case scenario approximation for the amount of charge that may need to be available at any time is calculated by integrating the large power spike corresponding to data transmission at 25 kHz. This results in a total charge budget of 6.44 μC. A 47 μF capacitor is able to source this quantity of charge while experiencing a voltage drop of only 0.14 V. This means that a rectified voltage as low as 1.94 V is all that needs to be reached between the time when the MCU turns on and the first transmission occurs in order to prevent untimely shutdown in the middle of startup. In practice, this makes it much easier for the system to start up and immediately reduce power supply ripple.

Each device undergoes the same series of engineering confidence tests prior to implantation as outlined in Section 3.3.4. Figure 4.15 shows an example of an affirmative data fidelity check for the two channel configurations given in Table 4.1.

During this test a known input waveform (sine wave) is applied to both input channels, and the telemetered signals are reconfigured and plotted. The amplitude of the test signal is set to 2mVpp—the lowest amplitude sine wave that can be generated cleanly by available equipment. A frequency outside of the AFE bandwidth (10 Hz in this case) is used to prevent the signal from railing in the high gain (60dB) channel.

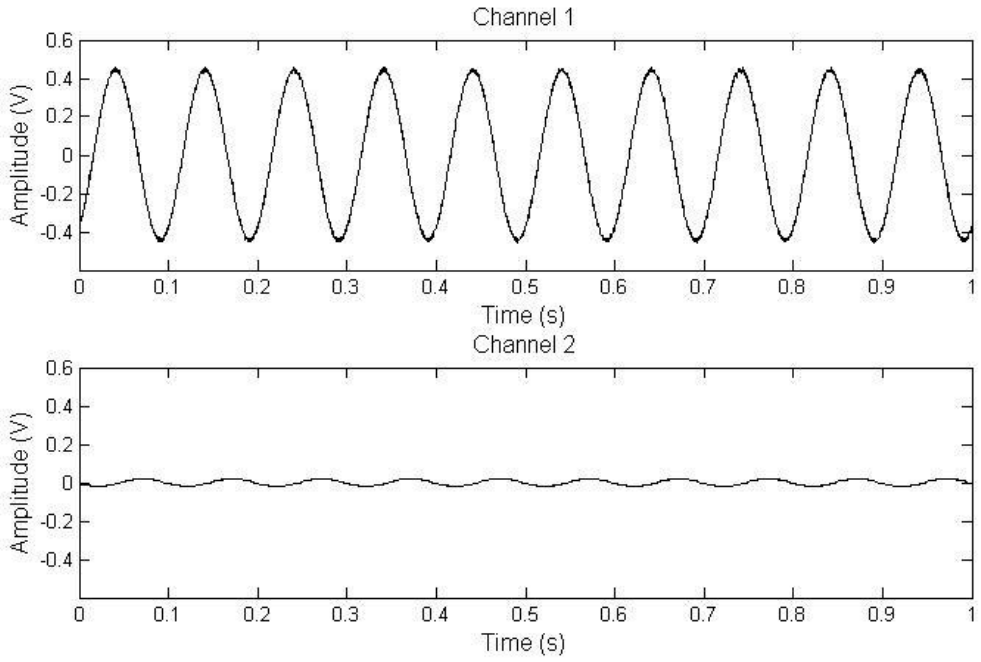

Figure 4.15 Full system response to a known input sine wave with an amplitude of 2 mV_{pp} and a frequency of 10 Hz. Channel 1 is the output from the high gain (60 dB in bandpass) analog front-end (AFE) intended for spontaneous muscle and nerve activity while channel 2 is the output from the low gain (34 dB) in bandpass) AFE intended for larger CMAP responses.

The peak-to-peak amplitude of the signal into the ADC (after the effects of AFE gain and filtration) is predicted in circuit simulation to be 1.07 V for the high gain channel and measured to be 0.92 V. The predicted peak-to-peak amplitude of the signal

outputted from the second, low gain (34 dB) channel is 52.7 mV and measured to be 42.7 mV. The slight discrepancies between simulated and measured results at this out-of-band frequency are likely due to the tolerances (1-5%) of the passive components used to set the bandwidth. However, deviations in the AFE frequency response on this minor scale will not perceivably alter the quality of measured bioelectric signals.

The performance characteristics of the full system Bionode as well as those specific to the AFE and stimulator are summarized in Table 4.2. Typical values represent either measured system parameters or default parameters, although some of these may be altered during assembly or within the firmware. When given, minimum and/or maximum values designate the permitted ranges of parameters that can be adjusted at any time using the GUI and wireless communication to the device. The Bionode's high level of functionality and flexibility is reflected in Table 4.2, which specs out the most advanced implantable system available for mouse electrophysiology.

Table 4.2 Bionode performance characteristics. Typical values represent measured characteristics for the default configuration. Minimum and maximum values represent ranges for adjustable parameters.

		Conditions	Min.	Typ.	Max.	Units
Recording Channels	*Gain* [1]		--	60	--	dB
	High-pass cutoff [1]		--	0.01	--	kHz
	Low-pass cutoff [1]		--	1	--	kHz
	CMRR	*DC to 60 Hz*	80	--	--	dB
	Input Impedance [2]		--	100	--	GΩ
	Input-referred noise	*f =0.01-3 kHz*	--	50	--	nV/√Hz
	Ch.1 → Ch.2 crosstalk		--	-99	--	dB
	Ch. 2 → Ch.1 crosstalk	*f =100Hz*	--	-98	--	dB
	ADC resolution		8	--	10	bits
	ADC input voltage range		--	1.2	--	V
	Total sampling rate (SR)		1	--	25	kHz
Stimulator	*Voltage headroom* [3]		±4	±10.5	±10.5	V
	Current amplitude	*Load = 10 kΩ*	50	--	1,050	µA
	Current amplitude resolution		--	1.5	--	µA
	Pulse width (PW)		50	--	--	µs
	Pulse width resolution		--	1	--	µs
	Pulse rate		--	--	20	kHz
	Charge Balance Error	*PW = 100 µs*	--	< 1	--	%
Other	*Mass* [4]		--	2.2	--	g
	Average power consumption	*SR = 5 kHz*	--	5.0	--	mW
		SR = 25 kHz		6.7		
	Peak power consumption	*Transmitter on*	--	20.5	--	mW
	Temperature resolution	*0-65 °C*	--	0.07	--	°C

[1]These parameters may be modified during the build phase based on signal of interest.
[2]Input impedance reported by INA333 datasheet released by Texas Instruments [25]
[3]Voltage headroom depends on power transfer efficiency (PTE) and is limited to 10.5V to prevent damage to the voltage regulator IC.
[4]Mass measured after medical epoxy encapsulation.

4.5 Implant Assembly for Mice

The Bionode's power and core modules are placed inside a cylindrical capsule when implanted in rats. This packaging strategy allows the contents of the capsule to be removed and adapted at the expense of greatly increasing the total volume of the

implant. At over 3 cm long and 1 cm wide this implant is unsuitable for a mouse of any size. An alternative packaging strategy is needed that maximally reduces the dimensions of the device. The strategy must also support a modular electrode interface whereby different types of electrodes may be easily connected for different experimental goals and disconnected for reuse.

This second objective does not necessarily preclude the use of parylene-C deposition, which is used to seal the Myonode (see Section 3.3.3). Sealing the device with a 15 to 20 µm-thick layer of parylene-C layer is certainly the least bulky packaging strategy and would lead to the smallest total volume and mass. However, such a thin barrier between the biaxial receive coils and the tissue means that the coil properties are likely to be affected and thereby detuned by the tissue. This would make it difficult to achieve optimal impedance matching conditions as the tuning process would have to somehow anticipate the variable conditions of the device's environment once implanted. More importantly, though, the conformal dielectric does not offer structural support to mechanically stabilize the now complex assembly of modules and coils. These present multiple points of weakness for the flexural and torsional loading likely to occur once implanted. For this reason an alternative coating process is used, which results in a more rigid and permanent fixture of the device modules.

The process of packaging the Bionode for implantation in mice is described in Section 4.5.1. This process simultaneously addresses the requirements for miniaturization, reusability, robustness, and post-packaging coil tuning. The ability to replace or add capacitive elements to alter the coils' impedance matching networks

after the device has been sealed is a crucial capability since the process of sealing the coils has been shown to detrimentally alter their tuning. A method of protecting and isolating this circuitry so that it is always accessible is integrated into the build process that produces a packaged, readily implantable device. Sections 4.5.2 and 4.5.3 describe the build and electrical performance of the two types of electrodes used in this work: cuff electrodes and anchored intramuscular electrodes.

4.5.1 Packaging of Bionode Modules

Figure 4.16 illustrates the step-by-step packaging process for a Bionode intended for implantation in mice. It begins with a fully assembled core module, which includes a temporary 10-pin header for ease of programming and debugging. The first step is to remove this header and solder 0.51 mm-diameter male pins (Mill-Max, 3320-0-00-15-00-00-03-0) to the now exposed pads of the recording and stimulating channels' inputs and outputs. These pins will be used to modularly connect to different types of electrodes and are manufactured at a length of 6.35 mm. However, they are trimmed to two thirds this length prior to mounting to avoid lengthening the device more than is necessary why still ensuring electrical continuity to the companion female header (Mill-Max, 3061-0-19-15-21-27-10-0). At this stage a small piece of clear tape is placed above the microelectronics on the core module to isolate them electrically from components and traces on the bottom side of the power module, which is stacked on top of the core module to reduce the total footprint of the device. The two modules are mechanically

and electrically affixed to one another through five parallel wires. Each wire connects a supply voltage or, in one case, ground between the two modules.

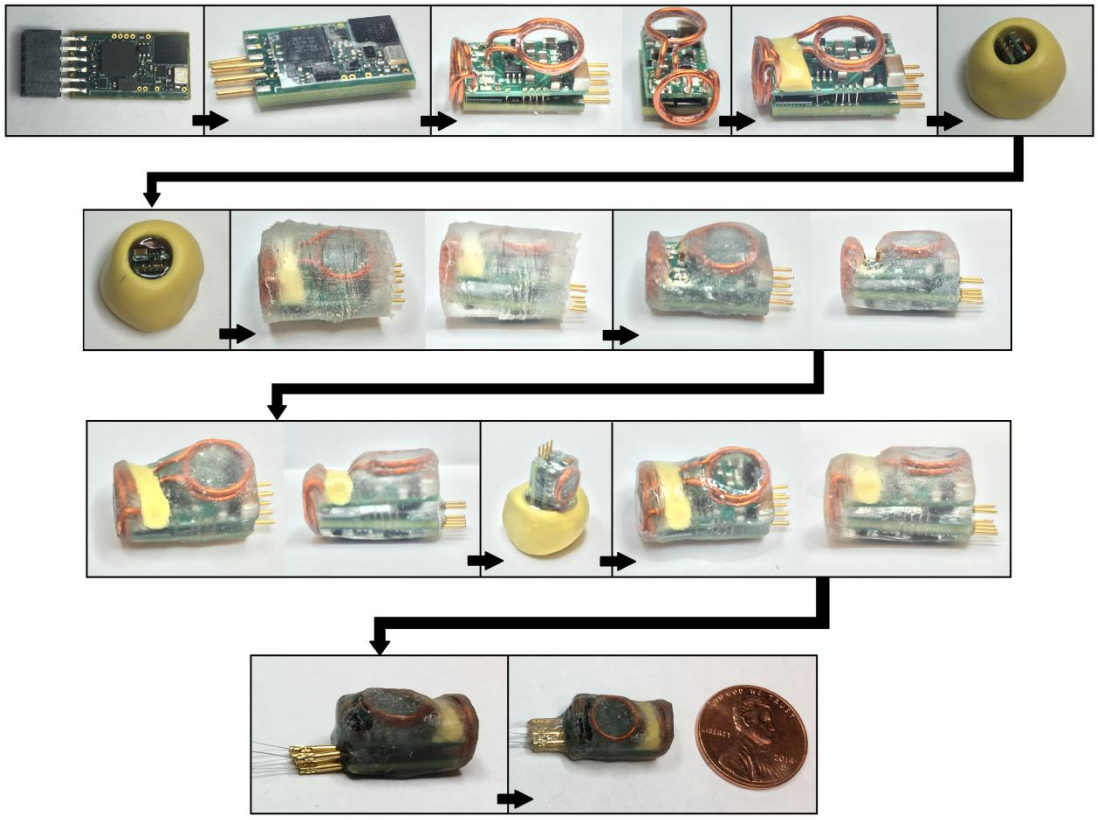

Figure 4.16 Bionode packaging process for implantation in mice.

Next, a two-part mold putty is mixed and press-fit into the space around the coils' impedance matching circuitry to protect it from direct contact with the epoxy which will permanently secure the modules and electrode pins in place. The putty is again used to create a cylindrical mold for the device that will allow it to be inserted lengthwise while protruding the electrode pins. The mold is filled halfway with a medical epoxy (Loctite,

M-31CL) and the device is slowly inserted into the mold. Additional epoxy is added from the top to fill open space around the device. Care is taken to make sure the level of the epoxy does not surpass the top edge of the board where it can begin to detrimentally coat the electrode pins, which should be left exposed.

Once the epoxy has set, the device is removed from the mold and excess epoxy is removed using a rotary contour sander (Dremel, 100-N/6). During the sanding process the epoxy above the putty insert protecting the impedance matching circuitry is etched away and the insert is removed. At this point the coils undergo their final tuning to account for any changes in performance on account of the epoxy shell. After tuning a second putty insert is placed above the impedance matching network to prevent detuning from epoxy adjacent to the capacitors and to allow for future access to the matching network as needed.

A second, shorter, cylindrical mold is made in order to seal the open part of the device around the putty insert. Half of the device is placed inside the mold and a second round of medical epoxy is injected and allowed to set. The device is then removed from the mold and excess epoxy is once again removed by the rotary contour sander to minimize the volume of the finished device. The average mass of the Bionode in this form (without electrodes) is 2.24 g (n = 4). The maximum dimensions are 8 mm x 8 mm x 15 mm, resulting in an estimated volume of 0.96 cm^3. A comparison to other fully implantable devices that have been used in mice (see Table 1.1) demonstrates that the Bionode is suitably small for mice that are 16 g or larger.

The pin terminals between the Bionode and the selectable electrodes present a challenge in that they, too, must be isolated from the tissue environment. However, since it is desirable that the devices be reusable, these interfaces must be sealed with something that is less permanent than medical epoxy but still biologically inert. After the desired electrodes have been attached to the electrode pins, a two-part silicone adhesive (Nusil, MED2-4213) is mixed and applied between and around the pin terminals and heat set at 100 °C. This adhesive serves to isolate the input and output channels from the surrounding tissue while also easing flexural stresses on the leads wires where they are crimped into the female headers. The transition from flexible wire to rigid header is the most likely point of mechanical failure due to repeated or excessive bending, so extra silicone is built up around this junction to add springiness to—and prevent very small radii of curvature from occurring at—the joint.

4.5.2 Recording Electrodes for Chronic imEMG

The epimysial recording electrodes that are used for EMG collection with the Myonode are phased out in the Bionode on account of the lack of success with anchoring them to the muscle while simultaneously avoiding catastrophic failure of the joint between the lead and electrode surface. They are replaced by anchored imEMG electrodes, the build process of which is described in [184]. Briefly, two 7-stranded stainless steel (type 316) wires coated in perfluoroalkoxy alkane (PFA) (A-M Systems, 793200) are placed in parallel and crimped together inside the barrel of a 27 gauge needle on one end. A knot is tied with both wires approximately 4 cm from the needle

and a 1 mm-long exposures is cut with a scalpel on each wire between the knot and the needle. On one wire this exposure begins 2 mm from the knot and on the other wires this exposure begins 4 mm from the knot, resulting in an inter-electrode spacing of 2 mm. The free ends of the wires that are not crimped together into the needle are crimped individually to female header pins that connect to the male electrode pins on the Bionode. Figure 4.17 illustrates two sets of these imEMG electrodes (as well as a stimulating cuff electrode, which is the subject of Section 4.5.3) affixed to the Bionode.

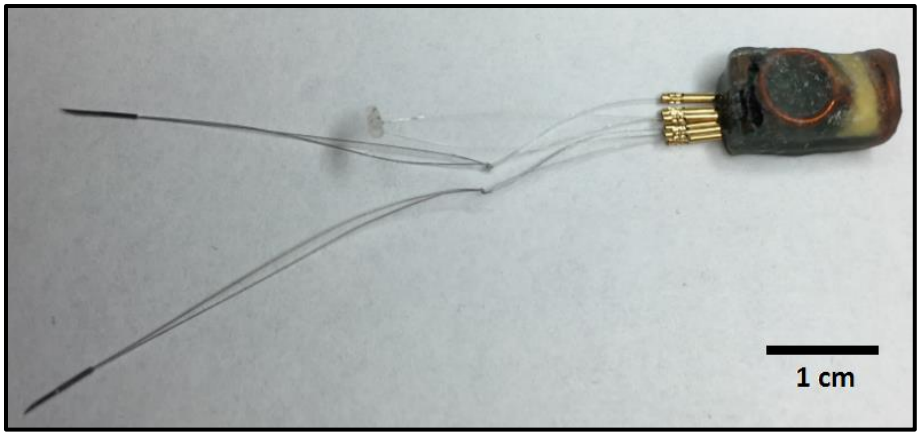

Figure 4.17 Bionode implant equipped with two pairs of intramuscular EMG (imEMG) recording electrodes and a stimulating cuff electrode.

The implantation procedure is fairly simple and involves threading the needle and its wires through the target muscle until the knot stops further advancement of the wire. When this is done care must be taken to ensure that the distance from the insertion point (where the knot is now flush with the muscle) to the exit point is at least 5mm so that both electrode exposures are embedded within the muscle. A second knot

is tied with both wires at the exit point such that the tightened knot sits flush with the surface of the muscle. Finally, the needle and excess wire are removed by making a cut close to the second knot.

4.5.3 Cuff Electrodes for Peripheral Nerves

A cuff electrode is designed specifically for either recording or stimulating of peripheral nerves in mice. This cuff electrode is an adaptation of the build process described in [23]. The base of each cuff electrode is a 3 mm length of silicone tubing (A-M Systems, 806700), which has an inner diameter of 0.635 mm and an outer diameter of 1.2 mm. A 30 gauge needle is inserted into the tube interior and then out of the tube approximately 1 mm circumferentially from the insertion point. A 6 cm length of 7-stranded stainless steel wire—the same wire used for the imEMG electrodes (see Section 4.5.2)—is cut and a 5 mm length of the wire is bared at one end by stripping off the PFA coating with a scalpel. The stripped end of the wire is threaded through the needle and then the needle is extracted, leaving behind the wire interwoven in the tube wall. The portion of the bare wire inside the tube is then shaped to the interior wall of the tube, forming a semicircular electrode contact that occupies at least 75% of the tube's interior circumference. This process is repeated 1 mm down the length of the tube to create a second electrode contact and an inter-electrode spacing of 1 mm.

The bare ends of both wires protruding from the tubing are trimmed to approximately 1 mm from the surface of the tube and then fixed in place with the same silicone adhesive used to seal the electrode interface (see Section 4.5.1). This prevents

the bare wire ends from slipping back through the tubing wall. The other end of the wires which are still coated with PFA and form the electrode leads are also fixed to the tubing with silicone adhesive. Finally, a lengthwise cut is made in the wall of the tubing between where the lead wires enter and the extra wire exits so that the cuff can be slipped around the nerve. Each lead wire is then crimped into a female header pin compatible with the male electrode pins on the Bionode. Figure 4.17 illustrates one of these cuff electrode as well as two recording imEMG electrodes connected to the Bionode.

The electrical performance of these cuff electrodes needs to be characterized since it can affect the performance of the stimulator circuit. For simplicity the stimulator is evaluated on the bench top using a 10 kΩ resistor to represent the electrode and tissue impedance load at the stimulator output. In reality, this is not a good model for an electrode surrounded by an electrolyte. As pointed out in Section 4.3.2, the electrode-tissue interface can be modeled by a resistor in parallel with a capacitor, so the electrode impedance will have some dependence on the frequency content of an applied voltage. It is possible that by a combination of electrode material and small surface area the impedance of the electrode might be high enough that the voltage headroom (±10.5 V) might be reached before the desired current amplitude is reached. For this reason the frequency-dependent impedance profile of each cuff electrode is measured using a Gamry Reference 600+ potentiostat. During the electrochemical impedance spectroscopy (EIS) test the cuff electrode is submerged in a phosphate buffer solution (PBS) bath with a measured pH of 7.4. Figure 4.18 plots the impedance

of a series of fabricated cuff electrodes. As a point of comparison to other cuff electrodes, the average total impedance of these cuff electrodes is reported at 1 kHz and is 13.8 ± 6.8 kΩ (n = 16). The high standard deviation of the measured impedance is likely due to the fact that the cuff electrodes are made by hand and the surface area of the wire exposed inside the silicone tube can change on account of process variation.

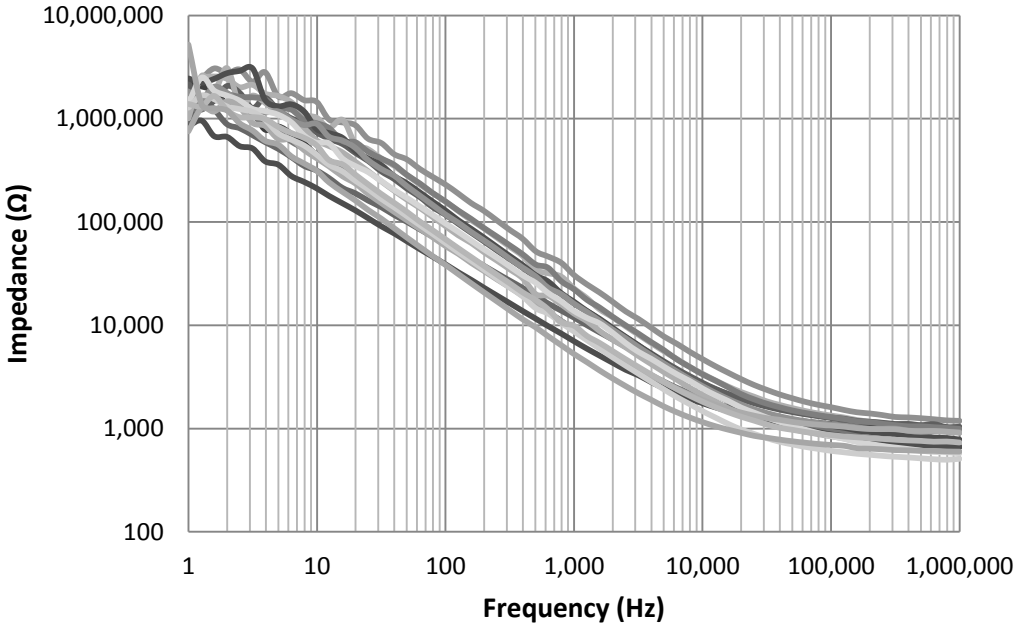

Figure 4.18 Impedance profiles of 16 mouse nerve cuff electrodes. Average impedance at 1 kHz is 13.8 kΩ.

The rectangular waveform of the current pulse applied during stimulation (see Figure 4.9) will result in a complex frequency composition of the corresponding voltage waveform. What's more, the voltage needed to source the desired current will depend on the amplitude and pulse width of the stimulus. This makes it difficult to predict whether or not the stimulator will reach its voltage headroom and undesirably cap the

output current based on the data of Figure 4.18 alone. Instead, the current through the cuff electrode is measured directly to confirm that currents up to 1 mA may be applied through the cuff electrode without reaching the voltage headroom. During this test the cuff electrode is submerged in 0.9% PBS and the voltage across a low-value (5 Ω) resistor in series with the cuff electrode is measured over time. Figure 4.19 compiles the measured current through the cuff electrode for the same series of stimulus waveforms given in Figure 4.9 (where a 10 kΩ load is used in place of the cuff electrode in PBS).

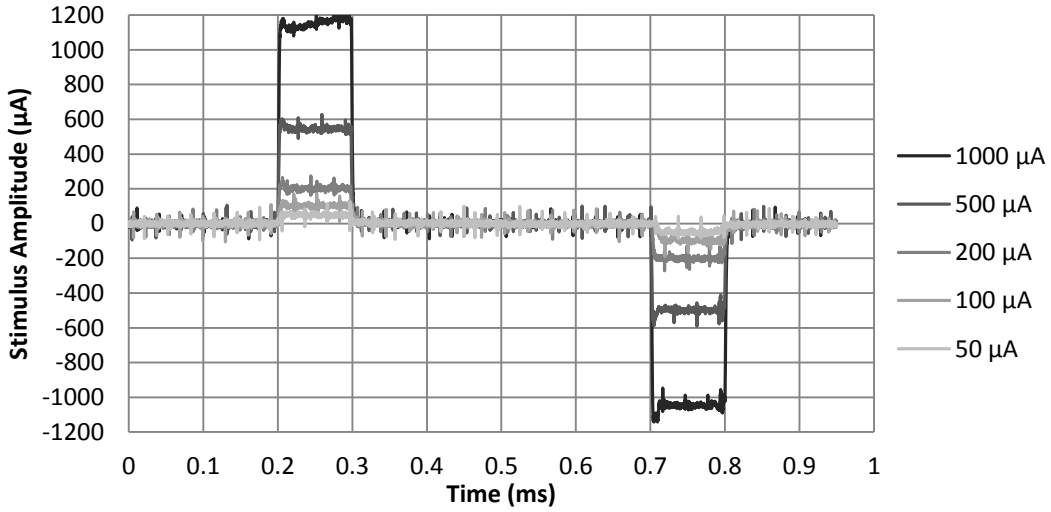

Figure 4.19 Stimulus current measured in series with a nerve cuff electrode submerged in 0.9% phosphate buffer solution (PBS) for five different current amplitude settings. Pulse width is set to 100 µs.

The added noise observed in Figure 4.19 compared to Figure 4.9 is due to the fact that very small voltages are being measured across a 5 Ω series resistor instead of much larger voltages measured across a 10 kΩ load resistor. However, the rectangular

current pulse is still seen clearly and closely matches the current amplitude setting. This affirms that the current amplitude is not being clipped as a result of high electrode impedance. A moment is taken here to point out a slight discrepancy in the measured current amplitudes of Figures 4.19 and 4.9. Particularly at higher pulse amplitudes there is an overshoot of achieved current as compared to desired current. This can be attributed to the fact that the stimulus amplitude calibration (see Section 4.3.2) is performed when the stimulator's load is a 10 kΩ resistor. This issue might be addressed to some extent by performing the stimulator calibration using a cuff electrode in PBS as the stimulator's output load. However, this still does not guarantee a perfect replication of *in vivo* load conditions, and there will always be some mismatch between optimal calibrations on the bench top and *in vivo*.

The sensitivity of the stimulator's amplitude calibration to changes in the load impedance, part-to-part variation in current mirror MOSFETs, desired pulse width, and supply voltages is a weakness of this stimulator topology. However, these shortcomings can be handled by anticipating the stimulus pulse configurations that will be used in a chronic animal study and determining the optimal calibration for each of these potential configurations on the bench top under stimulator load conditions proximate to those that will exist *in vivo*. This strategy is employed for each Bionode used in this work.

The data of Figure 4.19 confirms that these cuff electrodes are suitable for the environment and stimulus pulse parameters anticipated for this work. However, it would also be useful to know how close the stimulator is to reaching its voltage headroom in case a change in electrode-tissue impedance should occur and necessitate

a higher voltage to achieve the same current. For this reason the voltage at the output of the stimulator connected to a cuff electrode in 0.9% PBS is measured during a 100 µs, maximal (1 mA) stimulus pulse, which can be seen in Figure 4.20. Figure 4.20 shows that the voltage under these stimulus conditions will not exceed 3.25 V, which means that the cuff electrode impedance would have to more than triple before the voltage headroom (10.5 V) is reached. This is unlikely to occur given that the current necessary to generate a maximum CMAP from a peripheral nerve cuff in a mouse remained unchanged over the course of 60 days in a previous study [23].

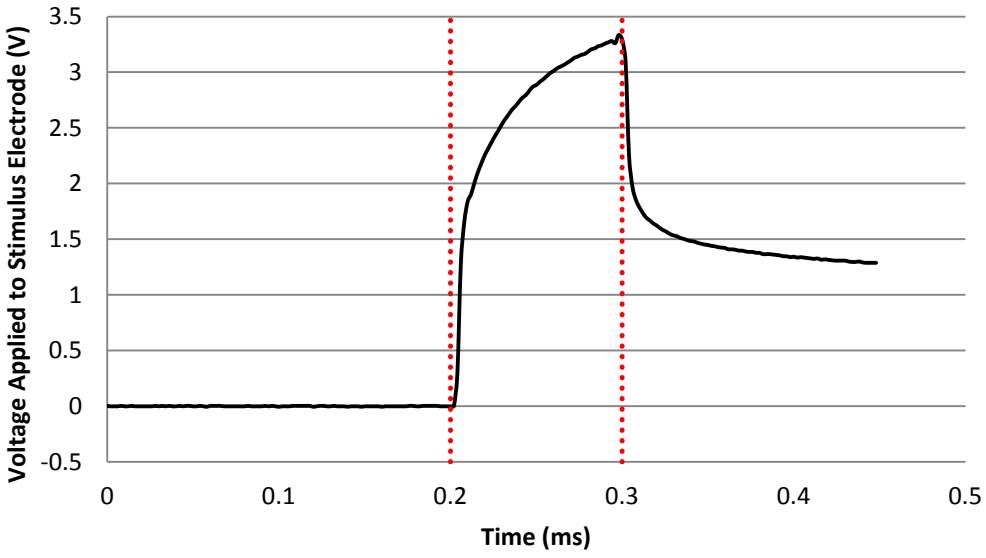

Figure 4.20 Stimulator output voltage corresponding to a 100 µs rectangular current pulse of 1 mA. Dotted red lines delineate stimulus pulse duration.

4.6 Acute *In Vivo* Performance in Rodents

The Bionode is intended for use in both rats and mice. The first *in vivo* evaluation of full system functionality involves concurrent use of the stimulator and recording

channels to measure stimulus evoked potentials in an anesthetized rat. The procedures and outcomes of this experiment are covered in this section. This experiment is followed by a similar procedure in a mouse in order to verify the efficacy of the recording and stimulating electrode strategies designed specifically for mouse work as described in Sections 4.5.2 and 4.5.3. This second experiment also serves to illustrate the expected amplitude of evoked CMAP signals, which will validate the gain selected for the recording channel. For the sake of CMAP amplitude resolution the maximum CMAP should occupy most of the ADC input voltage range, but it is important that the gain not be so high that the signal rails before the maximum CMAP is achieved. This experiment allows the gain on the channel intended for CMAP collection to be chosen intelligently.

4.6.1 Experimental Design and Methods

Simultaneous nerve stimulation using the Bionode's biphasic, current-controlled stimulator and measurement of CMAP response with the Bionode's AFE is performed first in a female Long Evans rat weighing 330 grams obtained from Envigo (Indianapolis, IN). This is done by first connecting a two-contact cuff electrode between the stimulator output and circuit ground then placing the cuff around the sciatic nerve of the rat. Stimulus pulses are then applied to the nerve and the CMAP response those stimuli are recorded from the biceps femoris muscle using the imEMG electrode described in Section 4.5.2. The current amplitude is gradually increased until the peak-to-peak amplitude of the CMAP response plateaus. The stimulus pulse width is fixed at 100 µs

during this experiment and a stimulation frequency of 2 Hz is used to avoid time-dependent changes in the measured response. Since CMAP responses in rats can be ten of mV in magnitude, the Bionode's AFE is configured for a gain of 25 (28 dB) to prevent saturation. The Bionode is powered from a DC supply during these experiments and the AFE output recorded on an oscilloscope for ease of data collection. These procedures are subsequently repeated in an anesthetized mouse.

4.6.2 Graded CMAP Response to Applied Stimuli

Figure 4.21 illustrates the peak-to peak amplitude of the CMAP measured in the biceps femoris muscle resulting from increasing stimulus current amplitude applied to the sciatic nerve of a rat. The threshold current needed to elicit a measurable CMAP response is 300 µA and the maximum CMAP amplitude is 30 mV_{pp}. Figure 4.22 shows a series of CMAPs recorded for stimulus current amplitudes ranging from 300 µA to 400 µA. During this experiment the stimulus artifact precedes the CMAP response by approximately 2 ms and is not shown.

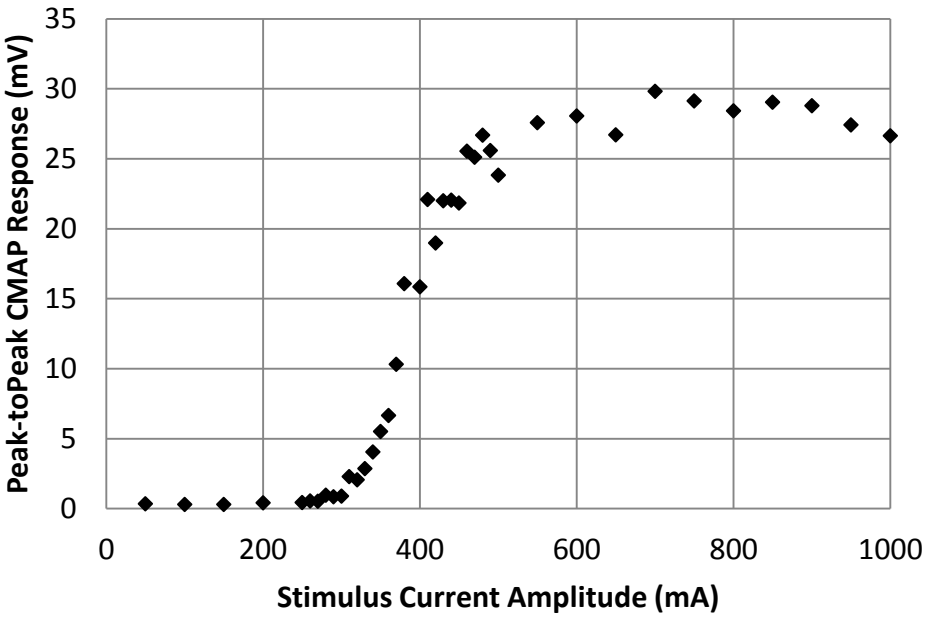

Figure 4.21 Peak-to-peak compound motor action potential (CMAP) response measured in the biceps femoris muscle by the Bionode's analog front-end (AFE) in response to increasing stimulus current amplitude from Bionode's stimulator applied to the sciatic nerve. Pulse width and stimulus frequency are fixed at 100 µs and 2 Hz, respectively.

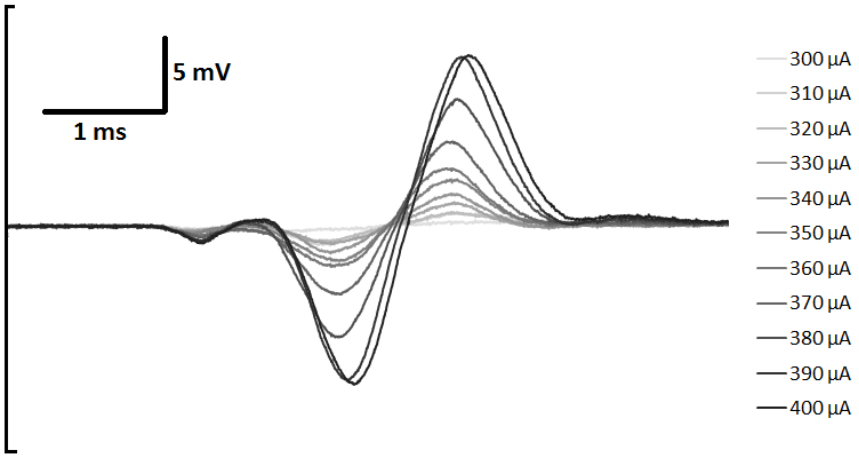

Figure 4.22 Samples of measured compound motor action potentials (CMAP) responses to stimulus amplitudes ranging from 300 µA to 400 µA applied to sciatic nerve of a rat. CMAP responses are measured using an intramuscular EMG (imEMG) electrode in the biceps femoris. Pulse width and stimulus frequency are fixed at 100 µs and 2 Hz, respectively.

This series of measurements is repeated in a wild-type (Black 6) mouse with the recording channel gain adjusted to 50 (34 dB) in anticipation that the maximum CMAP response will be smaller in the mouse than in the rat. Figure 4.23 shows the stimulus evoked muscle response to stimulus pulses ranging from 50 µA to 1 mA (the full range of the stimulator). Each waveform represents the average of three consecutive CMAP responses. The CMAP responses are recorded at a higher resolution in the range where it is expected that most axons will be recruited and rapid changes in CMAP amplitude will occur (200 µA to 400 µA). The waveforms compiled in Figure 4.23 are synchronized by the stimulus artifact, which precedes the CMAP response by approximately 1 ms and is not shown. It makes sense that the delay between stimulus artifact and evocation of the muscle response would be shorter in the mouse than in the rat owing to the shorter distance along the nerve from the cuff electrode to the innervated muscle.

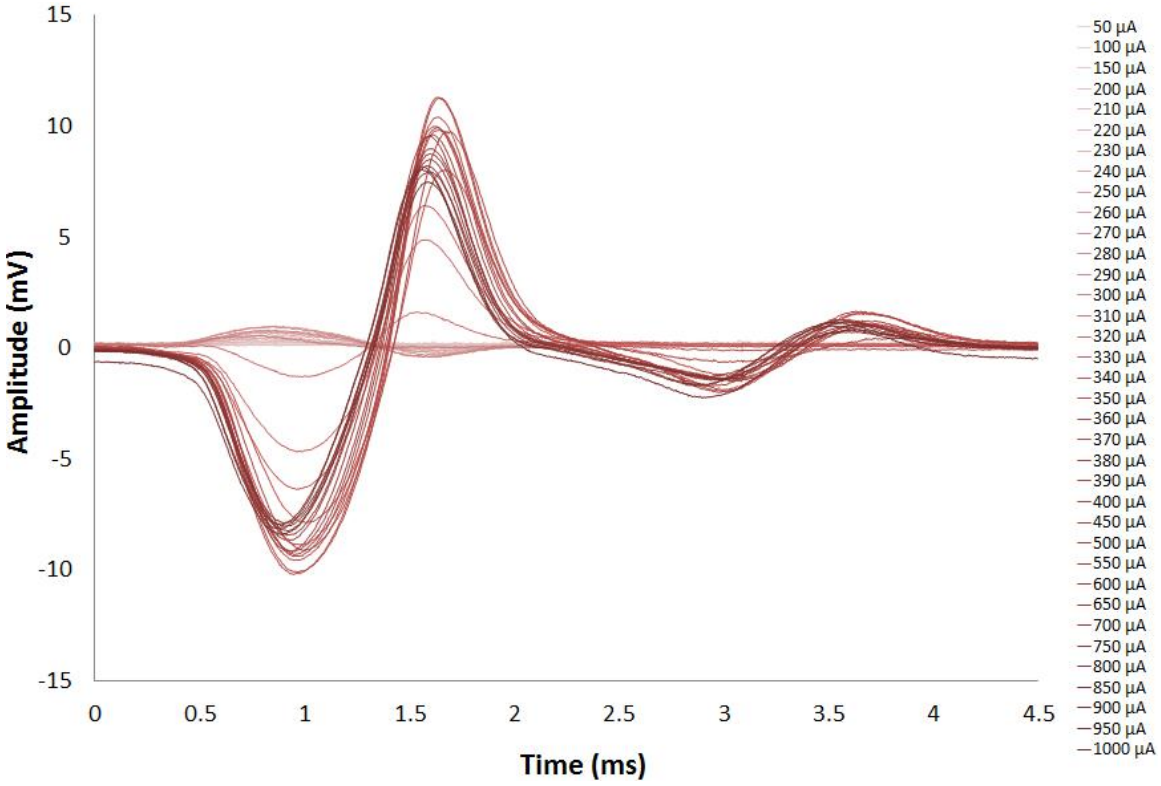

Figure 4.23 Measured compound motor action potential (CMAP) response to increasing stimulus amplitude applied to the sciatic nerve in a mouse. Each waveform represents the average of three consecutive responses measured from the biceps femoris muscle. Pulse width and stimulus frequency are fixed at 100 µs and 2 Hz, respectively.

The data shown in Figure 4.23 suggest that a maximum CMAP amplitude of approximately 20 mV_{pp} can be expected from this electrode configuration. The conclusion being that the low gain channel (34 dB) would be appropriate to measure this signal in a chronic experiment without exceeding the input voltage limitations of the ADC. One exciting thing to note about Figure 4.23 is a second, delayed waveform that can be observed starting around 2.5 ms at current amplitudes as low as 360 µA. Based on the characteristic delay and size, it is possible that this is an F-wave resulting from antidromic current reaching the motoneuron cell bodies in the spinal cord and causing a

small percentage of them to fire. This leads to a second, smaller CMAP, the delay of which can be used to measure NCV [185]. Since NCV is a common metric used for tracking neuromuscular and motoneuron diseases, the measured F-wave could be valuable in quantifying pathological changes in the nerve in future animal disease model studies [186, 187].

4.7 Chronic Recording and Stimulating of Bioelectric Activity in Rodents

The broad motivation for this project is to enable untethered collection of bioelectric activity in rodents. The more specific goal is to utilize this novel instrumentation in the study of neuromuscular and motoneuron disease mechanisms in mice. The acute, *in* vivo experiments of Section 4.6 indicate that the Bionode meets the desired performance criteria for study of normal and pathological activity of the neuromuscular system. The first chronic implantation of the Bionode is described in Section 4.7.2 and entails long-term EKG monitoring in a rat. Being both periodic and easily recognized, the EKG waveform is a good target for a first attempt at chronic data collection. This experiment serves three purposes: first, to evaluate the powering fidelity that might be expected from a freely behaving animal within the cavity resonator; second, to quantify the loss of data (BER) from the wireless data link operating within the cavity; and third, to demonstrate long-term, *in vivo* viability of the fully wireless and implantable system.

The chronic performance of the Bionode in mice is demonstrated here in three experiments. The first is a validation trial that tests the full functionality of the device in

a single implant. The second is an experiment comparing NAP activity in a CMT type 2D disease model to a wild-type control. The third is an experiment comparing CMAP responses to pulse trains in an ALS disease model compared to a wild-type control. The procedures for each of these experiments are covered in Section 4.7.1. Results of the validation experiment are discussed in Sections 4.7.3 and 4.7.4 while preliminary data from the disease models and their controls are presented in Section 4.7.5. These experiments represent only a small subset of possible chronic applications for the Bionode in mice, but serve to highlight a couple of experimental paradigms which are either enabled or improved by an untethered, batteryless implant.

4.7.1 Experimental Design and Methods

The first longitudinal experiment—a Bionode configured to measure two channels of EKG (Leads I and II configurations [188])—is performed in a female Long Evans rat obtained from Harlan Laboratories (Indianapolis, IN). The Bionode used in this experiment is not the final design iteration described in this chapter (see Section 4.1 for a description of the three Bionode iterations). The only important different to note for this experiment, though, is that the AFE operates in single supply mode and is identical to the AFE used in the Myonode (see Figure 3.5). This AFE is configured for a bandwidth of 1 Hz to 1 kHz and a gain of 60 dB.

The surgical procedures begin with the rat in the prone position. A 3 cm rostral-caudal incision is made on the side of the rat 0.5 cm left of midline. A subcutaneous pocket is created ventral to the initial incision that is large enough to accommodate the

implant, which is packaged in a 3D-printed capsule and coated with medical epoxy as shown in Figure 4.24. The implant is inserted into the pocket and oriented lengthwise such that the front coil lies fully in the transverse plane and the top coil lies fully in the sagittal plane, which are optimal for PTE in the magnetic field while the animal is walking normally on all fours and while rearing up on its hind limbs. Suture points on the implant are using to connect the device to the muscle surface and keep it oriented properly.

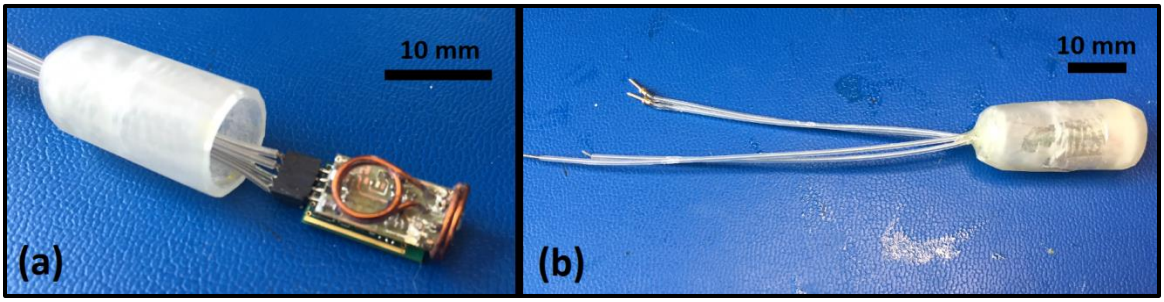

Figure 4.24 Bionode packaging for chronic implantation in rats. (a) Stacked power and core modules prior to encapsulation. (b) Closed capsule coated in medical epoxy and ready for implantation. Two pairs of electrodes are connected for lead I and lead II measurement of EKG.

The EKG is recorded by differential electrode pairs, which are routed to their target locations through subcutaneous tunneling to a second, lateral 0.5 cm incision close to the desired recording site. Once each lead reaches its target location it is sutured into place on the surface of proximate muscle. After each electrode has been anchored in place, both incision sites (the one over the device and the one over the electrode targets) are sutured shut. The efforts of Dr. John Jefferys, who performed the

surgery, should be acknowledged as well as those of Dan Pederson and Henry Mei, who periodically collected EKG data from the animal.

The Bionode is used in three different chronic mouse experiments. In all cases the configuration of the AFE channels is the same: one low gain (34 dB) channel for larger signals such as stimulus evoked CMAP and one high gain (60 dB) channel for smaller signals such as spontaneous imEMG or NAP. The goal of the first experiment is to stimulate and measure CMAP as well as record voluntary evoked EMG from the same mouse. This comprehensive test is performed in a 25 g, wild-type (Black 6) mouse and is intended to confirm that all of the device's functional blocks work correctly and concurrently once implanted. The surgical procedure for this and all subsequent chronic mouse experiments begins the same way: the animal is placed in the prone position and a 10 to 15 mm rostral-caudal incision is made beginning near the division of the vastus lateralis and the biceps femoris muscles and approximately 5 mm to the right of midline. Each implantation requires subcutaneous blunt dissection in the rostral direction until a pocket large enough to house the device is made. The device is inserted under the skin and anchored in place by a suture stitches through connective tissue on either side of the silicone adhesive-coated electrode pins. This stitch prevents the device from slipping backward towards the hind limb, which it is has a tendency to do without any anchoring. At this point the surgical technique will diverge depending on the number of electrodes and their respective targets.

For the purposes of the comprehensive validation test, the device is equipped with a peripheral nerve cuff electrode on the stimulating channel and an imEMG

electrode pair on each recording channel. This configuration is shown in Figure 4.17. The cuff electrode is slipped around the sciatic nerve and closed with a loose suture loop around the cuff circumference. Both imEMG electrodes are threaded through the biceps femoris muscle parallel to the muscle fibers. A second anchoring knot is made and the needle along with the excess wire is cleft from the electrode as described in Section 4.5.2. The incision is then sutured closed and the animal is placed in the cavity for initial data collection. The mouse is returned periodically to the cavity following implantation for data collection. Recording sessions in the cavity need not be very long in this study as the objective is successful collection of spontaneous EMG, which will occur any time the animal moves. The other objective of this study—successful provocation of CMAP responses from a fully implanted system—is done under anesthesia to reduce stress on the animal and improve data quality. A small coil (diameter = 7 mm) that is tuned to resonate at the same frequency as the cavity is used to wirelessly power the device at close proximities, which is possible when the animal is under anesthesia. This small coil is also used mid-surgery to confirm that the device is working properly prior to suturing the animal closed.

The second mouse experiment—and the first to integrate disease models—seeks to illustrate motor evoked potentials in the sciatic nerve of a healthy mouse as well as those present in a mouse carrying a genetic mutation of the *GARS* gene, which encodes for glycyl-tRNA synthetase. Mutations of the *GARS* gene are associated with phenotypes of CMT type 2D and are known to affect the properties of the peripheral nerves [189, 190], but questions still remain regarding the electrophysiological signature of this

disease. The target signals in this study are voluntary peripheral NAPs and possible aberrant nerve activity associated with visible tremors in the disease model. The Bionode's electrode configuration for this study is comprised of a single recording cuff electrode connected to the high gain channel. The surgical procedures are identical to the wild-type validation experiment except that no electrodes are inserted into the muscle and the high gain recording channel terminates in a cuff electrode that is attached to the sciatic nerve.

The purpose of the third experiment is to record stimulus evoked CMAP in the Tg.SOD^{G93A}, which is a disease model for ALS. These CMAP responses will be evoked in two ways: first, with low frequency (1-2 Hz) supramaximal stimuli to observe changes in maximum CMAP, which should decrease over time based on prior evidence [23]. Second, with sequences of faster (3-50 Hz) repetitive nerve stimulation (RNS) to observe the percentage difference in peak-to-peak CMAP response from the first to the last pulse in a stimulus train (typically ten pulses) [18]. This change should be more significant in the disease model than a healthy control, especially as both get older. Both of these changes in stimulus evoked CMAP behavior have been previously observed in the Tg.SOD^{G93A} model, so this experiment will serve to corroborate these findings while leveraging significant gains in efficiency and data resolution on account of the Bionode substituting for instrumentation of established protocols. For example, the procedure used to collect CMAP responses to RNS involves anesthetizing the animal, inserting transcutaneous needle electrodes for nerve stimulation, and affixing an EMG cuff to the

surface of the hind limb. This setup is complex and repetitively invasive, which means that the measurements are typically taken only once every few weeks in a single animal.

This experiment is intended to show how the Bionode can patently simplify the procedure for measuring stimulus evoked CMAP responses over time, which would have at least the immediate benefit of allowing changes in CMAP behavior to be observed at much higher temporal resolution. The surgical procedure for this experiment is nearly identical to that of the first validation experiment except that the high gain channel which is used previously for collection of spontaneous EMG is not used. A peripheral nerve cuff connected to the Bionode's stimulator is fastened to the sciatic nerve and an imEMG electrode from the low gain AFE is anchored inside the biceps femoris muscle as described in Section 4.5.2. For simplicity CMAP responses will be measured while the animal is awake and freely behaving within the resonant cavity. If for any reason this presents a significant issue, the mouse can, alternatively, be anesthetized briefly while the stimulus protocol and CMAP collection are carried out. Under these circumstances the device can be powered wireless using the same small, precisely tuned coil used for CMAP collection in the first chronic mouse experiment.

Data collection for each chronic mouse experiment is performed inside the resonant cavity. This testing environment is adapted for mouse work by introducing a motorized wheel, which is built with the assistance of Curtis Slaughbaugh, a student in the Center for Implantable Devices at Purdue University. In this way data can be collected either from the animal freely behaving in the open space within the cavity or during forced exercise inside the wheel. The wheel itself is placed strategically within

the cavity such that it resides within the strongest part of the magnetic field [71]. This considerably de-risks the WPT link by ensuring that the animal can always be placed and made to behave in an optimal position for power transfer. The wheel itself should incite cyclic behavior in the peripheral nerves and muscles of the hind limb, which can be useful in verifying and comparing measured data. The cavity's resonant mode and performance are highly sensitive to electrically conductive materials, so care is taken to ensure that all parts of the motorized wheel that reside within the cavity are made from plastic. Figure 4.25 shows the motorized wheel within the cavity; its drive shaft passes into the WPT environment through a 9.5 mm hole. The shaft is driven by a DC motor (McMaster-Carr, 6409K17) that allows up to 25 rpm and 20 in·lbs of torque at 12 V. The supply voltage is regulated by a DC power supply on the bench top.

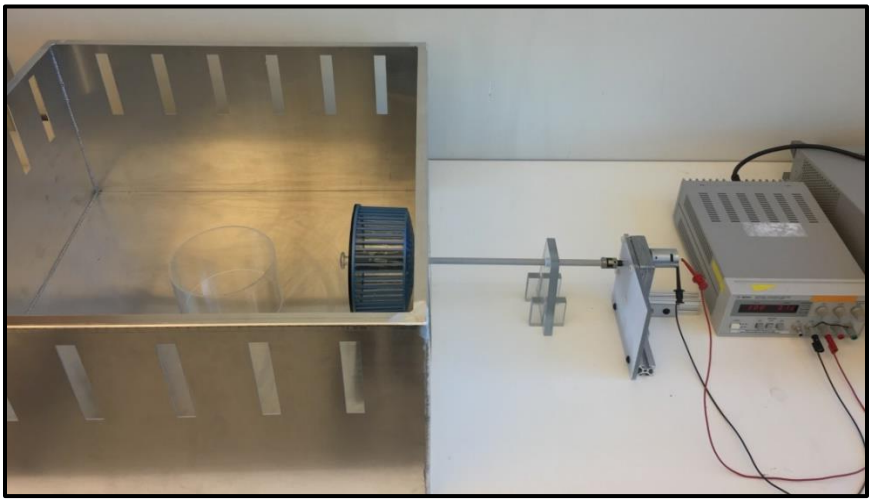

Figure 4.25 Resonant cavity WPT environment equipped with mouse wheel for controlled, cyclic behavior located where peak power transfer efficiency (PTE) is expected within the cavity.

During each recording session the animal is placed in the desired space—either the wheel or the open field—and then a lid is secured to the top of the cavity. In addition to routing data packets and instructions, the base station provides up to 4 W of power at the appropriate frequency (340 to 350 MHz) to the resonant cavity. The base station is placed outside of the cavity and communicates via Wi-Fi with a nearby computer running the GUI. Figure 4.26 captures the full testing setup and demarcates each of these system elements.

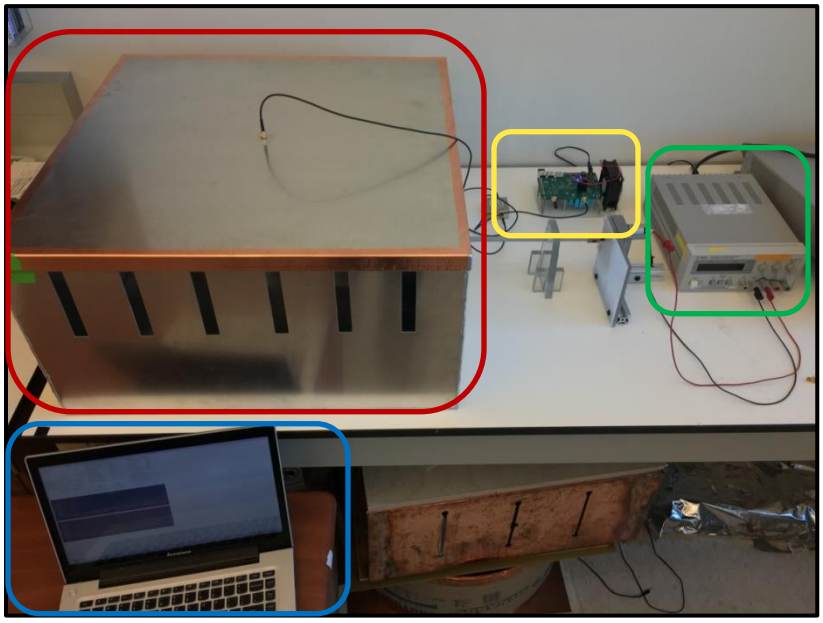

Figure 4.26 Comprehensive testing environment for fully wireless data collection from freely behaving animals including the resonant cavity (red), base station (yellow), power supply for mouse wheel operation (green), and a computer running the software user interface (blue).

4.7.2 Longitudinal EKG Measurement

Data collection from the Bionode implanted in the rat and configured for EKG measurement is performed in the resonant cavity as described in [71]. Following implantation and animal recovery, the rat is placed in the cavity for initial (day 0) data collection. Data is collected periodically over the course of 79 days in order to confirm continued device operation and to tack the quality of the EKG over time. Figure 4.27 shows a sampling of EKG measured over time from post-surgical days 0, 7, 43, and 79. In each instance the data is sampled at 2.5 kHz. The signal strength is quantified by the peak-to-peak amplitude of the EKG signal average over 30 heartbeats during each recording session. On day 0 the measured signal strength is 0.95 ± 0.045 mV. A decrease in the signal strength is observed on day 7 from a measured peak-to-peak EKG amplitude of 0.72 ± 0.041 mV. However, signal strength remains steady through day 43 (0.69 ± 0.069 mV) and day 79 (0.73 ± 0.089 mV). This signal degradation is likely due to formation of scar tissue around the electrodes contacts in combination with the relatively small (10 MΩ) input impedance of the now obsolete AFE used in this experiment. The unwanted voltage division of the recorded signal will likely improve greatly in subsequent chronic implantations where the final AFE (see Figure 4.5), which has an input impedance of 100 GΩ, is used.

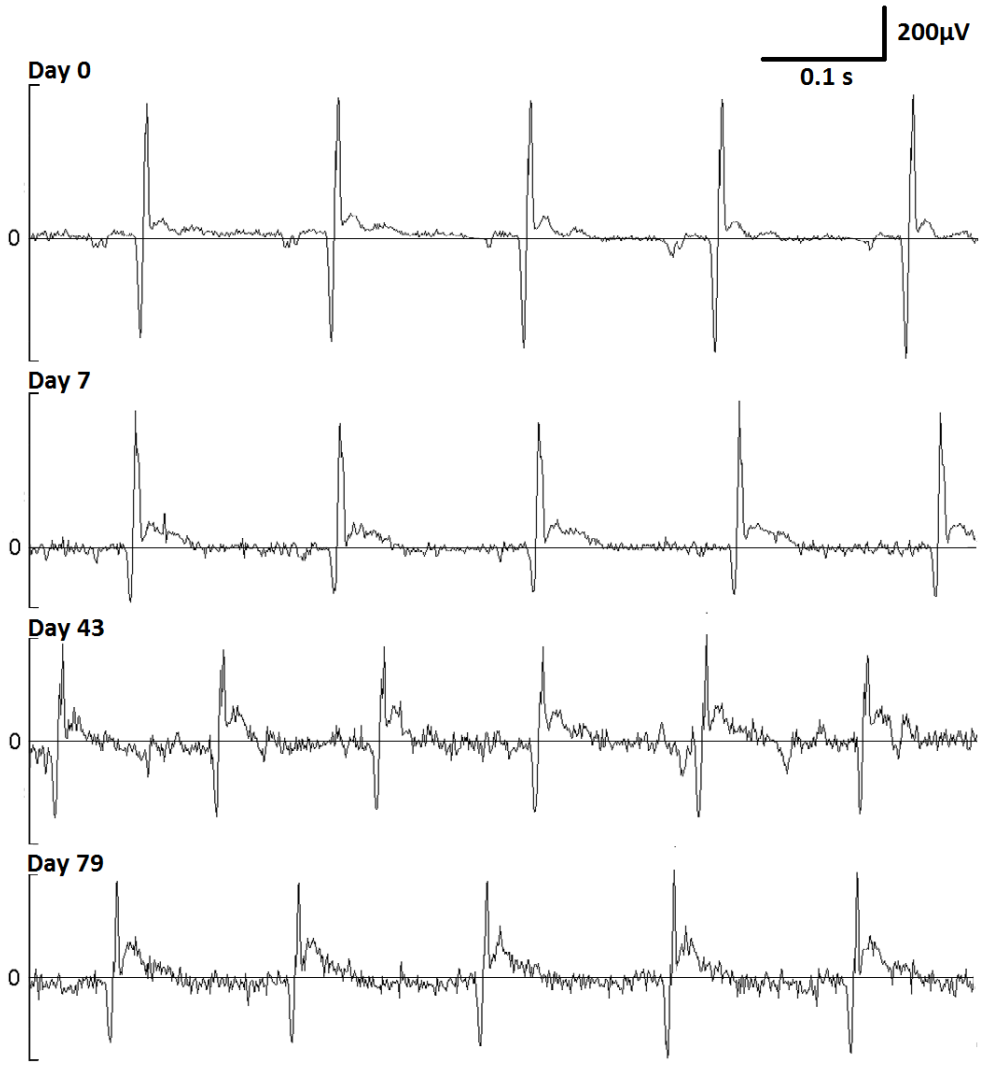

Figure 4.27 EKG collected longitudinally by a Bionode implanted in a rat.

The data collected in this experiment allows for an applied quantification of BER which offers a more realistic estimation of the Bionode's wireless performance as compared to bench top measurements where the transmitting and receiving antennas may be stationary and very close to one another. The BER is calculated by the percentage of data packets lost out of total data packets sent within a recording session.

A recording session is defined here as any period of data collection from a freely behaving animal within the resonant cavity lasting longer than 30 minutes. This measurement is performed over the course of nine recording sessions ranging from day – to day 64 post-implantation. The minimum and maximum BERs observed across the nine recording sessions were, respectively, 0.07% (measured on day 5) and 1.07% (measured on day 23). The combined recording time of these nine sessions is 39 hours, over which the total BER is 0.38%.

This experiment also allows powering fidelity to be quantified from a freely behaving animal within the WPT environment. If the monitoring period is long enough (a few hours), the ratio between the total time the device is on and total monitoring session time will represent the applied powering fidelity, which accounts for normal animal behaviors such as walking, resting, eating, drinking, and grooming. This offers a more practical and objective metric than peak PTE, which is how the quality of WPT links are often reported. The applied powering fidelity measured from the rat in the cavity over eight recording sessions—each last at least half an hour—for a total monitoring time of 35.5 hours is over 93% [71].

The outcomes of the chronic rat experiment are useful for understanding and setting expectations for the long-term performance of the full system. In this way they help to guide the experimental setup for the chronic mouse studies. For example, the calculated powering fidelity of 93% is likely sufficient for metrics like RMS or peak-to-peak amplitude of voluntary evoked EMG from normal ambulation. However, more sensitive measurements such as CMAP responses to stimulus pulse trains might require

a more consistent WPT link if only because this will greatly simplify data parsing. This observation led to the development of the mouse wheel (see Figure 4.25). This structure keeps the animal in a portion of the cavity where the magnetic field strength is strongest and the implanted device has the best chance for continuous, uninterrupted data acquisition.

4.7.3 Stimulus Evoked CMAP

The ability to generate chronic, stimulus evoked CMAP is demonstrated in a wild-type mouse during the first chronic mouse experiment with the Bionode. All stimulus pulse widths are 100 µs in duration and are evoked at a rate of 1 Hz. By convention, data from the cathodic stimulating phases are used when reporting CMAP responses [181]. To minimize the amount of time the animal is anesthetized, the stimulus amplitude is increased until an incipient CMAP response is observed. In this experiment to first observable CMAP occurs at 300 µA. The presumed maximum CMAP is then evoked immediately thereafter by setting the current amplitude to the upper limit of 1 mA. Figures 4.28(a) and 4.28(b) show superimposed threshold CMAPs and maximum CMAPs, respectively, measured in a wild-type mouse seven days post-surgery. Each CMAP is detected and synchronized by the stimulus artifact, which can be observed preceding the beginning of the CMAP by approximately 1 ms. The data shown in Figure 4.28 represent the first reported CMAPs evoked and measured in mice by a fully implantable recording device

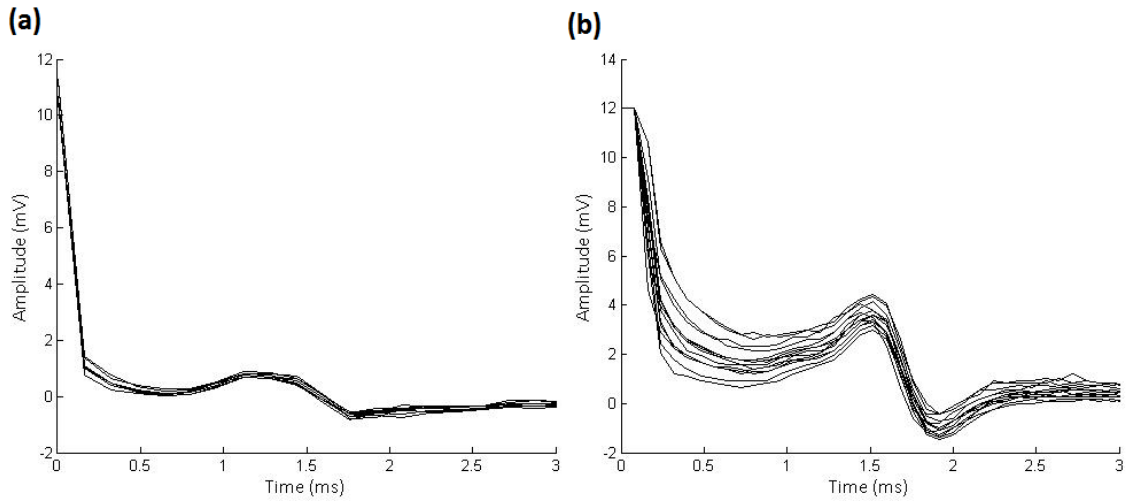

Figure 4.28 Series of (a) incipient and (b) maximum CMAP measured from Bionode implanted in wild-type mouse on Day 7 post-surgery.

4.7.4 Voluntary Evoked EMG

In the course of the validation experiment, voluntary evoked EMG is measured periodically from the wild-type mouse while it is freely behaving in the open field of the resonant cavity (see Figure 4.25). Figure 4.29 plots representative data from days 0, 2, and 5 post-surgery. This is already a marked improvement over the longevity of the electrode interface used on the Myonode, which failed within 48 hours of implantation. While the timespan is relatively short, this series of data is a promising indication for the long-term viability of the packaging and electrode schemes.

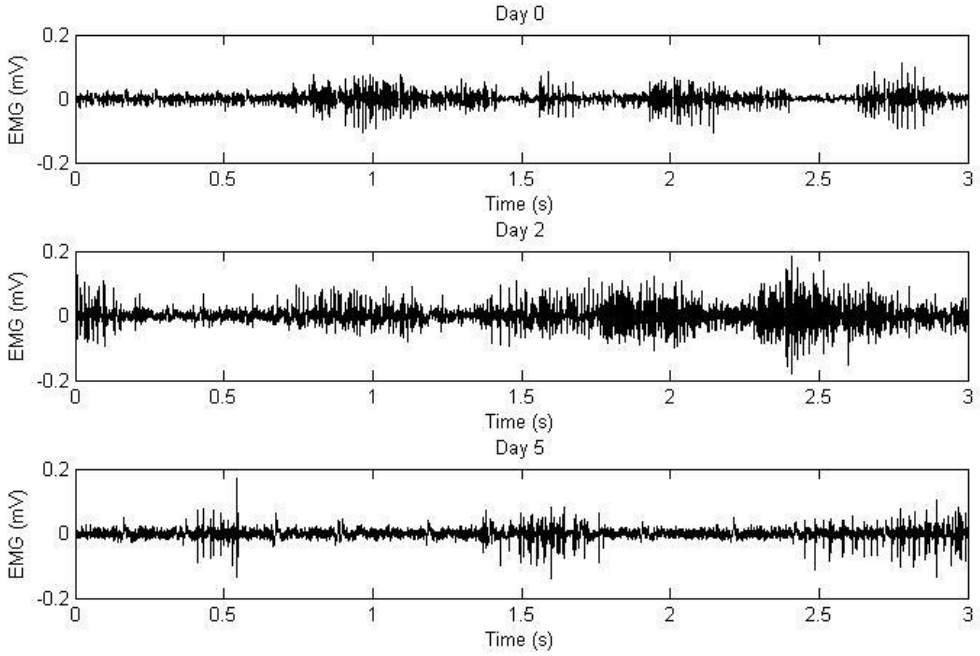

Figure 4.29 Samples of voluntary evoked EMG collected from a freely behaving wild-type mouse using the fully wireless Bionode system.

The intended course of the validation study is to collect voluntary evoked EMG as well as threshold and maximum CMAPs (like those shown in Figure 4.28) for as long as possible. However, beginning on day 9 the device becomes ostensibly detuned and ceases to operate in the cavity. Performance while powered with the small coil for stationary experiments is also considerably degraded to the point that only faint contractions are observed in response to purportedly large stimuli. This seems to suggest that the microelectronics are intact but some change has occurred in either the coils or the matching network to significantly drop the PTE to the point that the stimulator's voltage headroom is far below where it should be. Nevertheless the device is left implanted for a total of two weeks so that behavioral monitoring could continue

and complete healing of the incision wound can occur. This allows for some inferences to be made about how well the animal fares with the device as it is positioned and whether or not chronic implantation of the Bionode in such a small specimen is realistic.

It seems that the device is generally tolerated; the mouse is observed eating and grooming shortly after surgery and its gait is only marginally affected by the cuff around the sciatic nerve: an effect which becomes less noticeable over time. Figure 4.30(a) depicts the Bionode next to the animal subject prior to implantation. Figures 4.30(b) and 4.29(c) depict the animal subject from the top and the side after the device has been implanted for two weeks. Full wound closure and healing is achieved and the device is still positioned above the hip. These are both promising results since two potentially catastrophic events that can occur are that the mouse chews its stitches and they fall out prior to wound closure and that the device slips backwards until it rests on top of the hind limb flexor muscles. The latter scenario causes impairment of hind limb motion and puts hazardous stresses on the electrode leads as they undergo sharp bending between the electrode interface on the Bionode and their target nerve or muscle. One caveat should be noted here and that is that this implantation is performed in a fairly large (25 g) mouse. It remains to be seen how well smaller mice tolerate the implant.

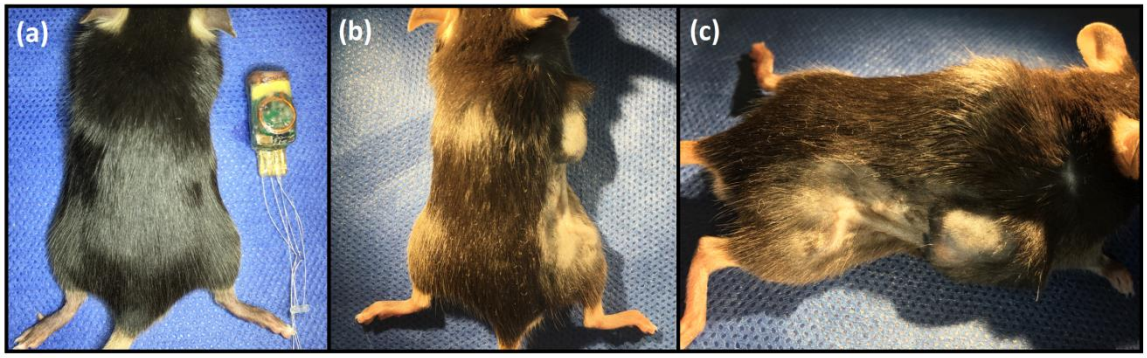

Figure 4.30 (a) Bionode device next to mouse immediately prior to implantation (day 0). (b) Top view of mouse 2 weeks after device implantation (day 14). (c) Side view of mouse two weeks after implantation.

The device is explanted after two weeks so that the point of failure can be determined. Careful dissection results in confirmed integrity and continuity of the electrode leads. The crimped terminals of the recording and stimulating electrodes as well as the entire electrode interface on the Bionode are inspected for displacement, breaches, or breakage. The electrode interface is still fully intact following explantation, which is yet another promising outcome of the experiment. The source of the failure is discovered to be the epoxy around the putty insert which encases the impedance matching circuit. This particular segment of epoxy is applied during the second deposition phase as described in Section 4.5.1, and is spongy to the touch following removal from the animal. When set properly the epoxy should be firm, so the likely explanation is that it did not set properly and allowed fluid to leak into the cleft that houses the impedance matching circuitry. This conclusion is reinforced by the detection of liquid and unset epoxy beneath the putty insert. For this reason care is taken on all

future assemblies to be sure that the second epoxy deposition phase which forms the barrier around the putty insert is properly set.

4.7.5 Ongoing Study in CMT and ALS Disease Models

The experiments for evaluating voluntary evoked nerve activity in the CMT type 2D disease model and stimulus evoked CMAP from the hereditary ALS disease model are ongoing. However, some preliminary findings and data are discussed here. Figure 4.31 illustrates recurrent bursts of sciatic nerve activity resulting from forced walking inside the wheel shown in Figure 4.25. These data are collected from a GARS^{C201R} mouse: a model for CMT Type 2D. There is no clear precedent within the literature for collecting and quantifying voluntary peripheral nerve activity in awake and behaving mice. These data comprise the first reported voluntary NAP to be collected by a fully implantable measurement system.

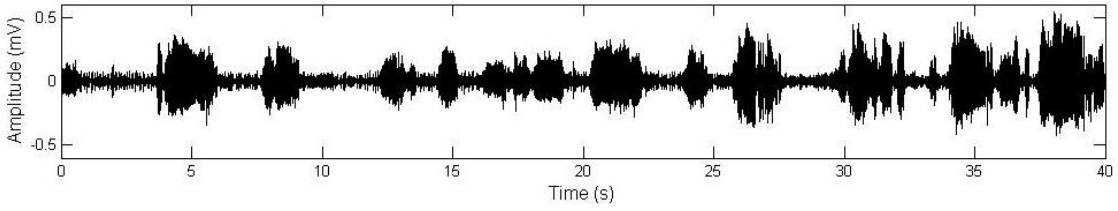

Figure 4.31 Voluntary nerve action potentials (NAPs) collected from an awake and behaving mouse while performing forced walking within a wheel.

This new instrumentation and methodology may be used to track changes in amplitude and frequency composition of the data shown in Figure 4.31 over time.

Additionally, they can be used to test the effects of pharmacological agents on nerve activity. For example, sodium channel blockers introduced into the extracellular environment around the nerve might disparately impact nerve behavior in the CMT Type 2D disease model compared to its control, which might implicate sodium channel deficiencies as playing a role in the disease mechanism. This is just one of many potential experimental protocols which would be easy to carry out once the Bionode is implanted and stabilized in its environment.

Another early result of the $GARS^{C201R}$ mouse study is the observation of intermittent, low-amplitude potentials which occur while the animal is at rest. Three examples of such activity as well as the baseline signal measured while the animal is under anesthesia are compiled in Figure 4.32. The sampling rate and ADC resolution used while collecting these data are 2.5 kHz and 8-bit, respectively. It may be that this activity is the result of nerve injury or irritation by the cuff electrode. However, one of the established phenotypes of this model is a visible tremor in the hind limb and tail. Another explanation for the observed spontaneous nerve activity might be that it correlates with this tremor. If this is the case, then these data are the first of their kind measured from this model. However, more instances of this activity will need to be recorded in the disease model and an absence of comparable activity in the wild-type control will need to be proven before other possible explanations can be ruled out.

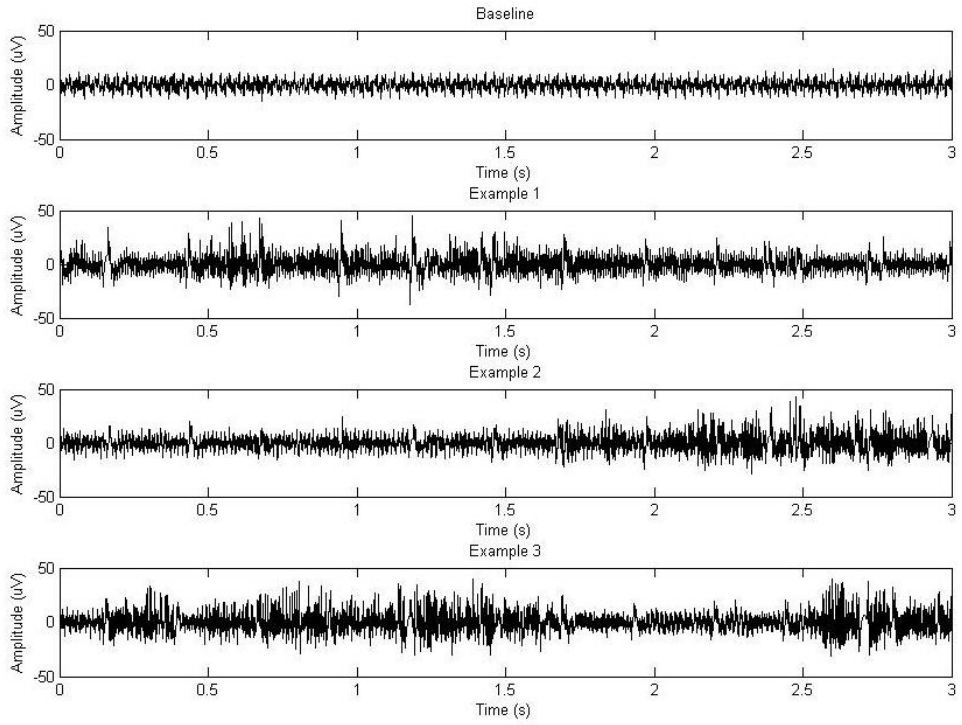

Figure 4.32 Sciatic nerve activity recorded from a disease model for CMT type 2D during stationary periods within the open field of the resonant cavity. Baseline data represents nerve activity while the animal is anesthetized. Examples 1, 2, and 3 represent intermittent, low-level potentials measured while the animal is at rest.

The ability to both elicit stimuli and record the response allows the Bionode to collected stimulus evoked CMAP from awake and freely behaving animals. The change in amplitude of the CMAP response to a fixed stimuli over time can indicate changes in muscle mass (resulting from growth or atrophy) or impairments of somatic signal transduction. Figure 4.33(a) illustrates a series of CMAPs recorded from an awake and freely behaving Tg.SOD^{G93A} mouse the day after implantation of the Bionode using a stimulus pulse width of 100 µs. The threshold current needed to elicit a CMAP is 450 µA

and the CMAP amplitude plateaus near 700 µA. This gives the minimum and supramaximal conditions for this pulse width, which can be tracked over time.

In order to confirm that the observed response is a CMAP and not an artifact, the pulse width is doubled to 200 µs and the current amplitude is gradually increased once again. Figure 4.33(b) plots the result of this second sweep. In this instance the threshold current needed to elicit a CMAP is 400 µA and the CMAP amplitude plateaus near 650 µA. The consistent and appropriate duration of the muscle response in both cases (approximately 2 ms) as well as the observation that the stimulus intensity needed to trigger a measurable response is smaller when the stimulus duration is longer (which is consistent with the known behavior of strength-duration curves for excitable tissues) suggest that the implanted instrumentation is effectively collecting the signal of interest.

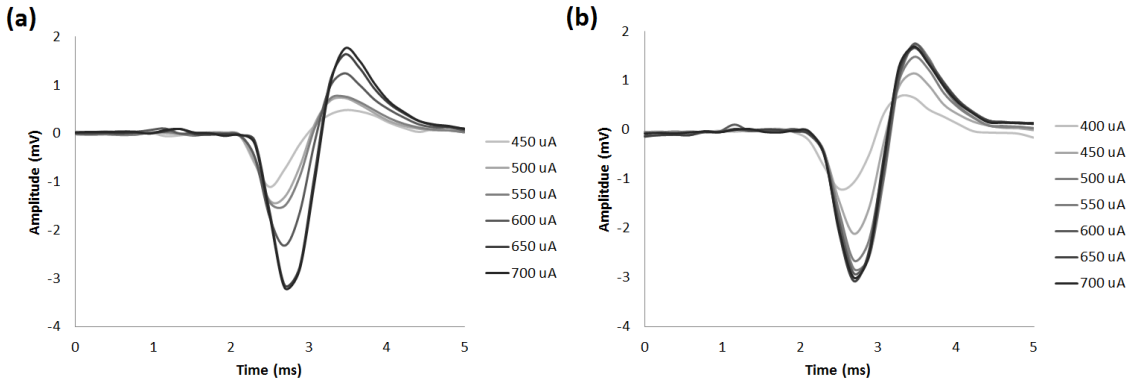

Figure 4.33 Evoked compound muscle action potential (CMAP) measured from the biceps femoris of a Tg.SOD^{G93A} mouse in response to a stimulus pulse with a duration of (a) 100 µs and (b) 200 µs. All waveforms shown are averages of ten successive CMAPs recorded at each level of stimulus intensity.

Another measurement of interest in the Tg.SOD^{G93A} mouse is the trend in stimulus evoked CMAP amplitude in response to higher frequency (3 to 50 Hz) stimulus pulse trains. Figure 4.34 plots the average amplitude of successive CMAPs resulting from RNS at 20 Hz. These data are collected the day after surgery using a pulse width of 100 μs and a resting period of at least 10 seconds between subsequent pulse trains. This creates an RNS response signature which can be used to detect deficits of the neuromuscular junction or the muscles themselves over time [18, 191].

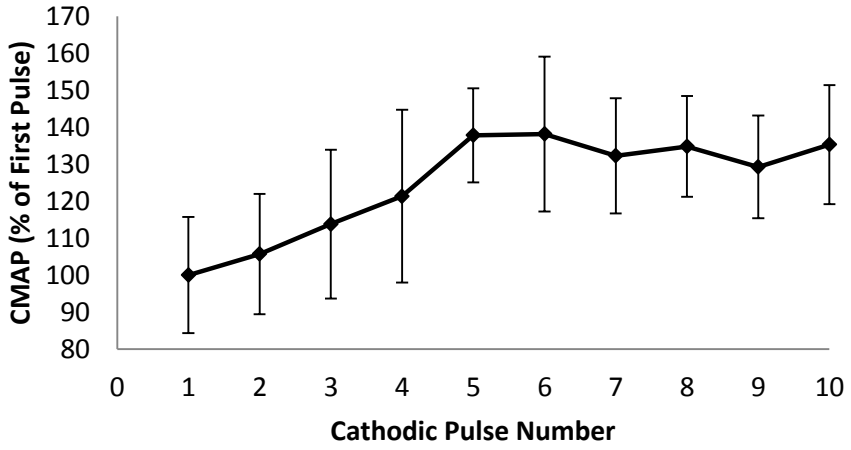

Figure 4.34 Peak-to-peak compound muscle action potential (CMAP) response to repetitive nerve stimulation (RNS) measured as a percentage of the amplitude of the first pulse in a 20 Hz pulse train. The stimulus pulse train uses supramaximal conditions Error bars at each pulse number reflect standard deviation (n = 7).

4.8 Conclusion

The Bionode represents the state-of-the-art in fully wireless and implantable biosensors for mice. Its capabilities far exceed those of any battery operated system and,

furthermore, allow anesthesia and tethering to be removed entirely from experimental protocols for long-term bioelectric data collection. This offers significant gains in efficiency as well as data resolution and consistency compared to many established, long-term electrophysiology protocols for mice. The fully implantable recording device developed in this work is able to collect two crucial target signals useful in studying neuromuscular disease progression–CMAP and voluntary nerve activity—that have never before been measured in a mouse by a fully wireless system.

The Bionode follows the same design principle as the Myonode—that is, all the microelectronic elements integrated on the Bionode's power and core modules are commercially available. This offers flexibility and consistency in the finished product (not to mention faster turnaround on design iterations) which would have been impracticable had the systems been designed all or partially in CMOS technology. Despite the added volume and power consumption that come with compiling individually packaged and standalone ICs, the Bionode maintains a form factor that is tolerable for subcutaneous implantation in mice and effectively powered by the resonant cavity WPT environment.

The demonstrated performance of each of the Bionode's functionalities while implanted in freely behaving mice supports its capacity to serve as an implement for finding new electrophysiological information about neuromuscular disease mechanisms. Two possible applications for this novel instrumentation are presently underway, which examine bioelectric markers of CMT and ALS. However, this system can be feasibly adapted for dozens of interesting electrophysiological studies. This work has resulted in

the collection of CMAP waveforms as well as voluntary muscle and nerve activity from devices implanted chronically in mice, but other useful metrics such as NCV, single fiber EMG, and CNAPs could certainly be targeted as well through appropriate AFE configuration paired with clever electrode design and placement.

An added benefit of having two recording channels is the capability to measure both the input to and output from muscles, which can degenerate for a variety of reasons in different neuromuscular disease models. This pairing of measurements might paint a more complete picture of disease progression by, as an example, allowing the user to identify which part of the neuromuscular system is affected first (nerve, neuromuscular junction, or muscle) and then monitor the temporal changes in each location relative to one another. This is yet another nod to the appreciable adaptability of the device, which implies that this work only scratches the surface of possible utilizations for longitudinal electrophysiology or behavioral monitoring in rodents.

CHAPTER 5. CONCLUSION

This work describes the development of a fully wireless and implantable device capable of recording both spontaneous and stimulus evoked bioelectric activity in mice. These efforts are driven by a need for improved instrumentation to study the electrophysiological mechanism by which neuromuscular and motoneuron diseases manifest and progress in mouse models. The finished device, which is termed the Bionode, improves on current technologies outlined in Table 1.1 by offering more capabilities and better performance in a comparably small volume (less than 1 cm^3). Moreover, the Bionode is designed for compatibility with a resonant cavity, which is the largest (by volume) reported WPT environment for rodents.

One of the early efforts of this work explores the feasibility of far field RF power transfer to bioelectric sensors embedded in tissue. The theoretical and numerical analyses of the power link budget between an electromagnetic field source and a receiving antenna inside mammalian tissue show conclusively that this WPT strategy is unsuitable for continuous operation of bioelectric sensors. This type of WPT link is more suitable for passive systems or those with much lower average power consumption that can leverage trickle charging and power cycling.

The Myonode—the precursor to the Bionode—serves to establish and debug build procedures, optimize the implant's functional protocol, and fine-tune the AFE topology and configuration. The Myonode is limited by only a single channel of recording, but is able to collect voluntary evoked EMG from mice, including some interesting disease-related aberrant muscle activity. The Myonode is also replicated and powered in an array for the purpose of relaying EMG for myoelectric-controlled prostheses. This offers some improvements to the versatility of wireless neural interfaces for upper-limb amputees.

The design procedures for both the Myonode and Bionode are predicated on the assumption that CMOS design and fabrication are not suitable for the development phase of new instrumentation. This is especially true considering the evolution of the WPT strategy in parallel with the evolution of the implantable device, which brings with it a handful of unanticipated issues. The dozen PCB design iterations used in this work is the best evidence in support of the decision to avoid an ASIC implementation until the system's topology is solidified. The use of only commercially available ICs and passives to build the Bionode did greatly improve yield and reliability compared to the CMOS tape-out described in Chapter 3. The end result is a batteryless implant which is capable of one channel of stimulating, two channels of recording, thermal sensing, and bidirectional telemetry. It is possible at this point to consider the benefits of condensing large blocks of this system on CMOS in order to further miniaturize and improve the efficiency of the end product.

A few limitations of the Bionode should be noted. First, owing to its volume and mass, there is a limitation on the size of the mouse in which the device can be implanted. An estimate of this limitation can be inferred from the reported device volume to minimum mouse size reported in Table 1.1.Being approximately 1 cm^3, the Bionode may be theoretically placed in animals as small as about 16 g. This does preclude the study of some neuromuscular diseases with prominent musclular atrophy or reduced body mass, but it should be suitable for most adult mice without such severe degenerative phenotypes. Second, the rate of data lost from fully wireless powering and communication will never be better than what one can expected from a tethered setup. The combination of powering and data fidelity—both of which are less than 100%—means that some data will invariably be lost when using the Bionode in an animal within the WPT environment. This should not pose a serious problem unless extremely rare, transient behaviors are the target. This particular scenario has been anticipated and partially addressed by the construction of a smaller testing environment (mouse wheel) placed in the optimal position within the cavity and close to the base station antenna.

One of the things that makes this device such a powerful tool is the fact that it addresses with very little compromise the limitations of tethered headstages, wireless headstages, and battery powered implants all at the same time. The Bionode has been used to collect both voluntary and stimulus evoked bioelectric signals in freely behaving animals. It is the first fully implantable system to collect voluntary nerve activity and CMAP in mice and the first one capable of recording its own evoked potentials. Also, on account of it dual, high-bandwidth recording channels, it is the only implantable system

that can record both the input and the output of muscles, which might allow it to pinpoint important pathological information like disease origin and clocked, directional progression.

This project's criteria for success should be revisited at this point. Recall that the main objective is to create novel instrumentation for chronic electrophysiology that is 1) small enough to be fully implanted in a mouse, 2) given sufficient functionality to be used in a variety of electrophysiological experiments, 3) able to function in the living environment once implanted, and 4) compatible with a WPT environment that enables the continuous collection of bioelectric activity from freely behaving mice. The chronic animal experiments described in Chapter 4 serve as the final indication that each of these criteria has been fulfilled. Furthermore, the applications of this novel instrumentation to the study of neuromuscular and motoneuron diseases underscores its immediate utility within the scientific community and newly supported capabilities for future experiments.

LIST OF REFERENCES

LIST OF REFERENCES

[1] A. E. H. Emery, "Population frequencies of inherited neuromuscular diseases—A world survey," *Neuromuscular Disorders,* vol. 1, pp. 19-29, 1991.

[2] R. Abresch, N. Seyden, and M. Wineinger, "Quality of life. Issues for persons with neuromuscular diseases," *Physical Medicine and Rehabilitation Clinics of North America,* vol. 9, pp. 233-248, 1998.

[3] C. M. McDonald, R. T. Abresch, G. T. Carter, W. M. J. Fowler, E. R. Johnson, D. D. Kilmer*, et al.*, "Profiles of Neuromuscular Diseases: Duchenne Muscular Dystrophy," *American Journal of Physical Medicine & Rehabilitation,* vol. 74, p. S93, 1995.

[4] A. E. H. Emery, "The muscular dystrophies," *The Lancet,* vol. 359, pp. 687-695, 2002.

[5] G. Kuhlenbäumer, F. Stögbauer, E. B. Ringelstein, and P. Young, *Hereditary Peripheral Neuropathies*: Steinkopff, 2005.

[6] T. Rogers, D. Chandler, D. Angelicheva, P. Thomas, B. Youl, I. Tournev*, et al.*, "A Novel Locus for Autosomal Recessive Peripheral Neuropathy in the EGR2 Region on 10q23," *The American Journal of Human Genetics,* vol. 67, pp. 664-671, 2000.

[7] L. E. Warner, C. A. Garcia, and J. R. Lupski, "Hereditary peripheral neuropathies: clinical forms, genetics, and molecular mechanisms," *Annu Rev Med,* vol. 50, pp. 263-75, 1999.

[8] G. Kuhlenbaumer, P. Young, G. Hunermund, B. Ringelstein, and F. Stogbauer, "Clinical features and molecular genetics of hereditary peripheral neuropathies," *J Neurol,* vol. 249, pp. 1629-50, Dec 2002.

[9] H. Skre, "Genetic and clinical aspects of Charcot-Marie-Tooth's disease," *Clinical Genetics,* vol. 6, pp. 98-118, 1974.

[10] S. Zuchner, "Peripheral neuropathies: whole genome sequencing identifies causal variants in CMT," *Nat Rev Neurol,* vol. 6, pp. 424-5, Aug 2010.

[11] H. Chial, "Rare genetic disorders: Learning about genetic disease through gene mapping, SNPs, and microarray data," *Nature Education,* vol. 1, 2008.

[12] K. M. Dipple and E. R. McCabe, "Phenotypes of patients with "simple" Mendelian disorders are complex traits: thresholds, modifiers, and systems dynamics," *Am J Hum Genet,* vol. 66, pp. 1729-35, Jun 2000.

[13] J. Won, J. R. Charette, V. M. Philip, T. M. Stearns, W. Zhang, J. K. Naggert*, et al.*, "Genetic modifier loci of mouse Mfrprd6 identified by quantitative trait locus analysis," *Experimental Eye Research,* vol. 118, pp. 30-35, 2014.

[14] Y. J. Li, W. K. Scott, D. J. Hedges, F. Zhang, P. C. Gaskell, M. A. Nance*, et al.*, "Age at onset in two common neurodegenerative diseases is genetically controlled," *American Journal of Human Genetics,* vol. 70, pp. 985-993, 2002.

[15] J. Colomer, R. Gooding, D. Angelicheva, R. H. King, E. Guillen-Navarro, Y. Parman*, et al.*, "Clinical spectrum of CMT4C disease in patients homozygous for the p.Arg1109X mutation in SH3TC2," *Neuromuscul Disord,* vol. 16, pp. 449-53, Jul 2006.

[16] K. Sivakumar, T. Kyriakides, I. Puls, G. A. Nicholson, B. Funalot, A. Antonellis*, et al.*, "Phenotypic spectrum of disorders associated with glycyl-tRNA synthetase mutations," *Brain,* vol. 128, pp. 2304-14, Oct 2005.

[17] T. Chung, K. Prasad, and T. E. Lloyd, "Peripheral neuropathy: clinical and electrophysiological considerations," *Neuroimaging Clin N Am,* vol. 24, pp. 49-65, Feb 2014.

[18] K. Mills, "Specialised electromyography and nerve conduction studies," *Journal of Neurology, Neurosurgery & Psychiatry,* vol. 76, pp. 36-40, 2005.

[19] B. U. Kleine, D. F. Stegeman, H. J. Schelhaas, and M. J. Zwarts, "Firing pattern of fasciculations in ALS: evidence for axonal and neuronal origin," *Neurology,* vol. 70, pp. 353-9, Jan 29 2008.

[20] M. C. Kiernan, S. Vucic, B. C. Cheah, M. R. Turner, A. Eisen, O. Hardiman*, et al.*, "Amyotrophic lateral sclerosis," *The Lancet,* vol. 377, pp. 942-955, 2011.

[21] E. Arnaud, J. Zenker, A. S. de Preux Charles, C. Stendel, A. Roos, J. J. Médard*, et al.*, "SH3TC2/KIAA1985 protein is required for proper myelination and the integrity of the node of Ranvier in the peripheral nervous system," *Proc Natl Acad Sci USA,* vol. 106, pp. 17528-33, Oct 2009.

[22] Y. Tanaka and N. Hirokawa, "Mouse models of Charcot-Marie-Tooth disease," *Trends in Genetics,* vol. 18, pp. S39-S44, Dec 2002.

[23] T. Akay, "Long-term measurement of muscle denervation and locomotor behavior in individual wild-type and ALS model mice," *Journal of Neurophysiology,* vol. 111, pp. 694-703, Feb 2014.

[24] V. M. Tysseling, L. Janes, R. Imhoff, K. A. Quinlan, B. Lookabaugh, S. Ramalingam*, et al.*, "Design and evaluation of a chronic EMG multichannel detection system for long-term recordings of hindlimb muscles in behaving mice," *J Electromyogr Kinesiol,* vol. 23, pp. 531-9, Jun 2013.

[25] R. E. Millard and R. K. Shepherd, "A fully implantable stimulator for use in small laboratory animals," *Journal of Neuroscience Methods,* vol. 166, pp. 168-177, Nov 2007.

[26] R. de Haas, R. Struikmans, G. van der Plasse, L. van Kerkhof, J. H. Brakkee, M. J. H. Kas*, et al.*, "Wireless implantable micro-stimulation device for high frequency bilateral deep brain stimulation in freely moving mice," *Journal of Neuroscience Methods,* vol. 209, pp. 113-119, Jul 2012.

[27] Triangle BioSystems International, "Wirelessly Programmable Dual Channel Neural Stimulation System," 2016.

[28] Triangle BioSystems International, "5 Channel Wireless Neural Recording System," 2016.
[29] Data Sciences International, "Physiotel™ HD Enabling New Research Technologies," 2015.
[30] BIOPAC Systems, Inc., "EPOCH-MSE-SYS Product Sheet," 2015.
[31] Millar, "Mouse Biopotential (ECG, EMG, EEG) Telemeter," 2016.
[32] C. Knight, J. Davidson, and S. Behrens, "Energy Options for Wireless Sensor Nodes," *Sensors,* vol. 8, pp. 8037-8066, 2008.
[33] E. Y. Chow, C.-L. Yang, Y. Ouyang, A. L. Chlebowski, P. P. Irazoqui, and W. J. Chappell, "Wireless Powering and the Study of RF Propagation Through Ocular Tissue for Development of Implantable Sensors," *IEEE Transactions on Antennas and Propagation,* vol. 59, pp. 2379-2387, 2011.
[34] B. Noureddine, M. Mehenni, and K. Smain, "Attenuation in Transferred RF Power to a Biomedical Implant due to the Absorption of Biological Tissue," *World Academy of Science, Engineering and Technology,* vol. 10, pp. 165-168, 2005.
[35] R. A. Bercich, D. R. Duffy, and P. P. Irazoqui, "Far-Field RF Powering of Implantable Devices: Safety Considerations," *Biomedical Engineering, IEEE Transactions on,* vol. 60, pp. 2107-2112, 2013.
[36] P. Li, J. C. Principe, and R. Bashirullah, "A wireless power interface for rechargeable battery operated neural recording implants," *Conf Proc IEEE Eng Med Biol Soc,* vol. 1, pp. 6253-6, 2006.
[37] J. A. Potkay, "Long term, implantable blood pressure monitoring systems," *Biomed Microdevices,* vol. 10, pp. 379-92, Jun 2008.
[38] C. Belhadj-Yahya, "Energy Options for Wireless Sensors," *2010 IEEE International Energy Conference and Exhibition*, 2010, pp. 564-569.
[39] J. I. Agbinya, *Wireless Power Transfer*: River Publishers, 2012.
[40] D. M. Pozar, *Microwave and RF Design of Wireless Systems*, 2001.
[41] W. C. Brown, "The History of Power Transmission by Radio Waves," *Microwave Theory and Techniques, IEEE Transactions on,* vol. 32, pp. 1230-1242, 1984.
[42] M. Catrysse, B. Hermans, and R. Puers, "An inductive power system with integrated bi-directional data-transmission," *Sensors and Actuators A: Physical,* vol. 115, pp. 221-229, 2004.
[43] N. Tesla, A. Marinčić, and M. N. Tesle, *Colorado Springs Notes, 1899-1900* vol. 3: Nolit Beograd, Yugoslavia, 1978.
[44] J. F. Schenck, "Safety of strong, static magnetic fields," *Journal of magnetic resonance imaging,* vol. 12, pp. 2-19, 2000.
[45] L. D. Abrams, W. A. Hudson, and R. Lightwood, "A Surgical Approach to the Management of Heart-Block Using an Inductive Coupled Artificial Cardiac Pacemaker," *The Lancet,* vol. 275, pp. 1372-1374, Jun 1960.
[46] G. E. Loeb, "Cochlear prosthetics," *Annu Rev Neurosci,* vol. 13, pp. 357-71, 1990.
[47] H. McDermott, "An advanced multiple channel cochlear implant," *IEEE Trans Biomed Eng,* vol. 36, pp. 789-97, Jul 1989.

[48] N. Chaimanonart and D. J. Young, "A wireless batteryless in vivo EKG and core body temperature sensing microsystem with 60 Hz suppression technique for untethered genetically engineered mice real-time monitoring," *Annual International Conference of the IEEE Engineering in Medicine and Biology Society* 2009, pp. 4872-4875.

[49] P. Irazoqui-Pastor, I. Mody, and J. W. Judy, "*In-Vivo* EEG Recordings Using a Wireless Implantable Neural Transceiver," *Neural Engineering, 2003. Conference Proceedings. First International IEEE EMBS Conference on,* 2003.

[50] P. F. Pasquina, M. Evangelista, A. J. Carvalho, J. Lockhart, S. Griffin, G. Nanos*, et al.*, "First-in-man demonstration of a fully implanted myoelectric sensors system to control an advanced electromechanical prosthetic hand," *Journal of Neuroscience Methods,* vol. 244, pp. 85-93, Apr 2015.

[51] W. J. Heetderks, "RF powering of millimeter- and submillimeter-sized neural prosthetic implants," *Biomedical Engineering, IEEE Transactions on,* vol. 35, pp. 323-327, 1988.

[52] W. H. Ko, S. P. Liang, and C. D. Fung, "Design of radio-frequency powered coils for implant instruments," *Med Biol Eng Comput,* vol. 15, pp. 634-40, Nov 1977.

[53] M. Soma, D. C. Galbraith, and R. L. White, "Radio-Frequency Coils in Implantable Devices: Misalignment Analysis and Design Procedure," *IEEE Transactions on Biomedical Engineering,* vol. 34, pp. 276-282, 1987.

[54] J. Uei-Ming and M. Ghovanloo, "Design and Optimization of Printed Spiral Coils for Efficient Transcutaneous Inductive Power Transmission," *Biomedical Circuits and Systems, IEEE Transactions on,* vol. 1, pp. 193-202, 2007.

[55] R. N. Simons, F. A. Miranda, J. D. Wilson, and R. E. Simons, "Wearable Wireless Telemetry System for Implantable Bio-MEMS Sensors," *Engineering in Medicine and Biology Society, 2006. EMBS '06. 28th Annual International Conference of the IEEE*, 2006, pp. 6245-6248.

[56] J. E. Degenford, M. D. Sirkis, and W. H. Steier, "The Reflecting Beam Waveguide," *Microwave Theory and Techniques, IEEE Transactions on,* vol. 12, pp. 445-453, 1964.

[57] G. Goubau and F. Schwering, "On the guided propagation of electromagnetic wave beams," *Antennas and Propagation, IRE Transactions on,* vol. 9, pp. 248-256, 1961.

[58] R. H. George, "Solid State Microwave Power Rectifiers," Raytheon Co. Burlington Mass Microwave and Power Tube Division1965.

[59] T. Le, K. Mayaram, and T. Fiez, "Efficient Far-Field Radio Frequency Energy Harvesting for Passively Powered Sensor Networks," *Solid-State Circuits, IEEE Journal of,* vol. 43, pp. 1287-1302, 2008.

[60] S. Mandal and R. Sarpeshkar, "Low-Power CMOS Rectifier Design for RFID Applications," *Circuits and Systems I: Regular Papers, IEEE Transactions on,* vol. 54, pp. 1177-1188, 2007.

[61] W. C. Brown, "The microwave powered helicopter," *J. Microwave Power,* vol. 1, 1966.

[62] J. Landt, "The history of RFID," *Potentials, IEEE,* vol. 24, pp. 8-11, 2005.

[63] E. Y. Chow, B. Beier, Y. Ouyang, W. J. Chappell, and P. P. Irazoqui, "High Frequency Transcutaneous Transmission using Stents Configured as a Dipole Radiator for Cardiovascular Implantable Devices," *Microwave Symposium Digest, IEEE MTT-S International,* pp. 1317-1320, 2009.

[64] E. Y. Chow, C.-L. Yang, A. Chlebowski, S. Moon, W. J. Chappell, and P. P. Irazoqui, "Implantable Wireless Telemetry Boards for *In Vivo* Transocular Transmission," *IEEE Transactions on Microwave Theory and Techniques,* vol. 56, pp. 3200-3208, 2008.

[65] E. Y. Chow, A. Kahn, and P. P. Irazoqui, "High Data-Rate 6.7 GHz Wireless ASIC Transmitter for Neural Prostheses," *Engineering in Medicine and Biology Society, 2007. EMBS 2007. 29th Annual International Conference of the IEEE*, 2007, pp. 6580-6583.

[66] S. Radiom, M. Baghaei-Nejad, G. Vandenbosch, Z. Li-Rong, and G. Gielen, "Far-field RF powering system for RFID and implantable devices with monolithically integrated on-chip antenna," *Radio Frequency Integrated Circuits Symposium (RFIC), 2010 IEEE*, 2010, pp. 113-116.

[67] O. Jonah and S. V. Georgakopoulos, "Wireless powering of biomedical device via magnetic resonance," *Wireless and Microwave Technology Conference (WAMICON), 2012 IEEE 13th Annual*, 2012, pp. 1-6.

[68] X. Rui-Feng, K. P. Basappa, C. Hyouk-Kyu, Z. Yuanjin, and J. Minkyu, "High-efficiency transcutaneous wireless energy transfer for biomedical applications," *Defense Science Research Conference and Expo (DSR), 2011*, 2011, pp. 1-4.

[69] Z. Fei, L. Xiaoyu, S. A. Hackworth, R. J. Sclabassi, and S. Mingui, "In vitro and in vivo studies on wireless powering of medical sensors and implantable devices," *Life Science Systems and Applications Workshop*, 2009, pp. 84-87.

[70] H. Mei, Y. Huang, K. Thackston, and P. P. Irazoqui, "Optimal Wireless Power Transfer to Systems in an Enclosed Resonant Cavity," *IEEE Antennas and Wireless Propagation Letters,* 2015.

[71] H. Mei, Thackston, K. A., Bercich, R. A., Jefferys, J. G. R., Irazoqui, P. P., "Cavity Resonator Wireless Power Transfer System for Freely-Moving Animal Experiments," *IEEE Transactions on Biomedical Engineering,* 2015. Submitted.

[72] M. Ortiz-Catalan, B. Håkansson, and R. Brånemark, "An osseointegrated human-machine gateway for long-term sensory feedback and motor control of artificial limbs," *Science Translational Medicine,* vol. 6, 2014.

[73] G. E. Loeb, "Taking control of prosthetic arms," *JAMA,* vol. 301, pp. 670-1, Feb 2009.

[74] K. A. Raichle, M. A. Hanley, I. Molton, N. J. Kadel, K. Campbell, E. Phelps*, et al.*, "Prosthesis use in persons with lower- and upper-limb amputation," *J Rehabil Res Dev,* vol. 45, pp. 961-72, 2008.

[75] J. Martin, "Focus on upper extremity: future of upper-limb design: clinical perspectives of the DARPA RP09 program," *American Academy of Orthotists and Prosthetists Academy TODAY,* vol. 4, 2008.

[76] J. Kuniholm, "Open Arms," *Spectrum, IEEE,* vol. 46, pp. 36-41, 2009.
[77] T. Williams, "Control of powered upper extremity prostheses," in *Functional Restoration of Adults and Children with Upper Extremity Amputation*, R. H. Meier and D. J. Atkins, Eds., ed New York (NY): Demos Medical Publishing, Inc, 2004, pp. 207-24.
[78] A. M. Simon, B. A. Lock, and K. A. Stubblefield, "Patient training for functional use of pattern recognition–controlled prostheses," *Journal of Prosthetics and Orthotics,* vol. 24, p. 56, 2012.
[79] L. H. Smith, T. A. Kuiken, and L. J. Hargrove, "Real-time simultaneous and proportional myoelectric control using intramuscular EMG," *Journal of Neural Engineering,* vol. 11, 2014.
[80] E. Scheme and K. Englehart, "Electromyogram pattern recognition for control of powered upper-limb prostheses: state of the art and challenges for clinical use," *Journal of Rehabilitation Research and Development,* vol. 48, pp. 643-59, 2011.
[81] S. Leowinata, B. Hudgins, and P. A. Parker, "A multifunction myoelectric control strategy using an array of electrodes," *16th Annu. Congr. the International Society Electrophysiology and Kinesiology*, Montreal, Canada, 1998.
[82] L. J. Hargrove, K. Englehart, and B. Hudgins, "A comparison of surface and intramuscular myoelectric signal classification," *IEEE Trans Biomed Eng,* vol. 54, pp. 847-53, May 2007.
[83] S. Micera, P. M. Rossini, J. Rigosa, L. Citi, J. Carpaneto, S. Raspopovic*, et al.*, "Decoding of grasping information from neural signals recorded using peripheral intrafascicular interfaces," *J Neuroeng Rehabil,* vol. 8, p. 53, 2011.
[84] T. A. Kuiken, G. Li, B. A. Lock, R. D. Lipschutz, L. A. Miller, K. A. Stubblefield*, et al.*, "Targeted muscle reinnervation for real-time myoelectric control of multifunction artificial arms," *JAMA,* vol. 301, pp. 619-28, Feb 2009.
[85] J. E. Cheesborough, L. H. Smith, T. A. Kuiken, and G. A. Dumanian, "Targeted muscle reinnervation and advanced prosthetic arms," *Seminars in plastic surgery,* vol. 29, pp. 62-72, 2015.
[86] T. Kuiken, K. Turner, N. Soltys, and G. Dumanian, "First clinical fitting of an individual after bilateral TMR with intuitive pattern recognition control," *Myoelectric Controls Symposium*, 2014.
[87] D. McDonnall, S. Hiatt, C. Smith, and K. S. Guillory, "Implantable multichannel wireless electromyography for prosthesis control," *Annual International Conference of the IEEE Engineering in Medicine and Biology Society*, 2012, pp. 1350-1353.
[88] S. Lewis, M. Russold, M. Hahn, and O. C. Aszmann, "Fully Implantable Multichannel EMG Measurement System: First Results," in *Replace, Repair, Restore, Relieve–Bridging Clinical and Engineering Solutions in Neurorehabilitation*, ed: Springer, 2014, pp. 51-59.
[89] D. R. Merrill, J. Lockhart, P. R. Troyk, R. F. Weir, and D. L. Hankin, "Development of an implantable myoelectric sensor for advanced prosthesis control," *Artificial organs,* vol. 35, pp. 249-252, 2011.

[90] G. Vandevoorde and R. Puers, "Wireless energy transfer for stand-alone systems: a comparison between low and high power applicability," *Sensors and Actuators A: Physical,* vol. 92, pp. 305-311, Aug 2001.

[91] T. A. Kuiken, "Rehabilitation of the Targeted Muscle Reinnervation Patient," in *Targeted Muscle Reinnervation A Neural Interface for Artificial Limbs*, ed: Taylor & Francis, 2013, pp. 67-76.

[92] T. A. Kuiken, D. S. Childress, and W. Zev Rymer, "The hyper-reinnervation of rat skeletal muscle," *Brain Research,* vol. 676, pp. 113-123, Apr 1995.

[93] H. Kang, L. Tian, and W. Thompson, "Terminal Schwann cells guide the reinnervation of muscle after nerve injury," *J Neurocytol,* vol. 32, pp. 975-85, 2003 Jun-Sep 2003.

[94] T. Kuiken, "Targeted reinnervation for improved prosthetic function," *Phys Med Rehabil Clin N Am,* vol. 17, pp. 1-13, Feb 2006.

[95] T. A. Kuiken, G. A. Dumanian, R. D. Lipschutz, L. A. Miller, and K. A. Stubblefield, "The use of targeted muscle reinnervation for improved myoelectric prosthesis control in a bilateral shoulder disarticulation amputee," *Prosthet Orthot Int,* vol. 28, pp. 245-53, Dec 2004.

[96] G. E. Loeb and C. Gans, *Electromyography for experimentalists*. Chicago: University of Chicago Press, 1986.

[97] G. E. Loeb, R. A. Peck, W. H. Moore, and K. Hood, "BION™ system for distributed neural prosthetic interfaces," *Medical Engineering & Physics,* vol. 23, pp. 9-18, Jan 2001.

[98] T. Cameron, T. L. Liinamaa, G. E. Loeb, and F. J. Richmond, "Long-term biocompatibility of a miniature stimulator implanted in feline hind limb muscles," *IEEE Trans Biomed Eng,* vol. 45, pp. 1024-35, Aug 1998.

[99] T. L. Fitzpatrick, T. L. Liinamaa, I. E. Brown, T. Cameron, and F. J. Richmond, "A novel method to identify migration of small implantable devices," *J Long Term Eff Med Implants,* vol. 6, pp. 157-68, 1996.

[100] L. J. Hargrove and B. A. Lock, "Future Research Directions," in *Targeted Muscle Reinnervation A Neural Interface for Artificial Limbs*, ed: Taylor & Francis, 2013, pp. 165-184.

[101] T. A. Kuiken, L. A. Miller, R. D. Lipschutz, B. A. Lock, K. Stubblefield, P. D. Marasco*, et al.*, "Targeted reinnervation for enhanced prosthetic arm function in a woman with a proximal amputation: a case study," *The Lancet,* vol. 369, pp. 371-380, 2007.

[102] K. Deisseroth, "Optogenetics," *Nature methods,* vol. 8, pp. 26-29, 2011.

[103] K. L. Montgomery, A. J. Yeh, J. S. Ho, V. Tsao, S. M. Iyer, L. Grosenick*, et al.*, "Wirelessly powered, fully internal optogenetics for brain, spinal and peripheral circuits in mice," *Nature methods,* 2015.

[104] J. L. Volakis, *Antenna engineering handbook*, 4th ed. New York: McGraw-Hill, 2007.

[105] W. S. Cheung, F. H. Levien, and Microwave Training Institute (Mountain View Calif.), *Microwaves made simple : principles and applications*. Dedham, MA: Artech House, 1985.
[106] "Title 47 of the Code of Federal Regulations; Radio Frequency Devices " in *47 C.F.R. 15*, ed: Federal Communications Commission, 2014.
[107] J. C. Lin, "Safety standards for human exposure to radio frequency radiation and their biological rationale," *IEEE Microwave Magazine,* vol. 4, pp. 22-26, 2003.
[108] V. Anderson and K. Joyner, "Specific absorption rate levels measured in a phantom head exposed to radio frequency transmissions from analog hand-held mobile phones," *Bioelectromagnetics,* vol. 16, pp. 60-69, 1995.
[109] L. J. Challis, "Mechanisms for interaction between RF fields and biological tissue," *Bioelectromagnetics,* vol. 26, pp. S98-S106, 2005.
[110] M. L. Meltz, "Radiofrequency exposure and mammalian cell toxicity, genotoxicity, and transformation," *Bioelectromagnetics,* vol. 24, pp. S196-S213, 2003.
[111] W. C. Dewey, L. E. Hopwood, S. A. Sapareto, and L. E. Gerweck, "Cellular responses to combinations of hyperthermia and radiation," *Radiology,* vol. 123, pp. 463-474, 1977.
[112] T. M. Seese, H. Harasaki, G. M. Saidel, and C. R. Davies, "Characterization of tissue morphology, angiogenesis, and temperature in the adaptive response of muscle tissue to chronic heating," *Laboratory investigation; a journal of technical methods and pathology,* vol. 78, pp. 1553-1562, 1998.
[113] P. S. Ruggera, D. M. Witters, G. von Maltzahn, and H. I. Bassen, "In vitro assessment of tissue heating near metallic medical implants by exposure to pulsed radio frequency diathermy," *Physics in Medicine,* vol. 48, pp. 2919-2928, 2003.
[114] T. Fujii and Y. Ibata, "Effects of heating on electrical activities of guinea pig olfactory cortical slices," *European Journal of Physiology,* pp. 257-260, 1982.
[115] C. Gabriel, "Compilation of the dielectric properties of body tissues at RF and microwave frequencies," Texas (USA)1996.
[116] J. S. Seybold, *Introduction to RF Propagation*: John Wiley & Sons, Inc., 2005.
[117] J. Heikkinen and M. Kivikoski, "Performance and Efficiency of Planar Rectennas for Short-Range Wireless Power Transfer at 2.45GHz," *Microwave and Optical Technology Letters,* vol. 31, pp. 86-90, 2001.
[118] G. Andia Vera, A. Georgiadis, A. Collado, and S. Via, "Design of a 2.45 GHz rectenna for electromagnetic (EM) energy scavenging," *Radio and Wireless Symposium*, 2010, pp. 61-64.
[119] E. Y. Chow, C.-L. Yang, A. Chlebowski, W. J. Chappell, and P. P. Irazoqui, "Miniature Antenna for RF Telemetry through Ocular Tissue," *Microwave Symposium Digest, 2008 IEEE MTTS-S International,* pp. 1309-1312, 2009.
[120] G. Breed, "Basic principles of electrically small antennas," *High Frequency Electronics,* 2007.
[121] D. B. Miron, *Small antenna design*. Burlington, MA: Newnes/Elsevier, 2006.

[122] G. N. Rao and J. Edmondson, "Tissue reaction to an implantable identification device in mice," *Toxicologic Pathology,* vol. 18, pp. 412-416, 1990.

[123] K. Sato, K. Sugibayashi, and Y. Morimoto, "Species differences in percutaneous absorption of nicorandil," *Journal of Pharmaceutical Sciences,* vol. 80, pp. 104-107, 1991.

[124] C. Chestek, P. Samsukha, M. Tabib-Azar, R. Harrison, H. Chiel, and S. Garverick, "Wireless multi-channel sensor for neurodynamic studies," *Sensors, 2004. Proceedings of IEEE*, 2004, pp. 915-918 vol.2.

[125] R. Harrison, P. Watkins, R. Kier, R. Lovejoy, D. Black, R. Normann*, et al.*, "A Low-Power Integrated Circuit for a Wireless 100-Electrode Neural Recording System," *Solid-State Circuits Conference, 2006. ISSCC 2006. Digest of Technical Papers. IEEE International*, 2006, pp. 2258-2267.

[126] T. A. Szuts, V. Fadeyev, S. Kachiguine, A. Sher, M. V. Grivich, M. Agrochao*, et al.*, "A wireless multi-channel neural amplifier for freely moving animals," *Nat Neurosci,* vol. 14, pp. 263-269, Feb 2011.

[127] D. Fan, D. Rich, T. Holtzman, P. Ruther, J. W. Dalley, A. Lopez*, et al.*, "A Wireless Multi-Channel Recording System for Freely Behaving Mice and Rats," *PLoS ONE,* vol. 6, p. e22033, 2011.

[128] D. Zhang, Y. Dong, M. Li, and H. Wang, "A Radio-Telemetry System for Navigation and Recording Neuronal Activity in Free-Roaming Rats," *Journal of Bionic Engineering,* vol. 9, pp. 402-410, Dec 2012.

[129] C. W. Chang and J. C. Chiou, "A wireless and batteryless microsystem with implantable grid electrode/3-dimensional probe array for ECoG and extracellular neural recording in rats," *Sensors (Basel),* vol. 13, pp. 4624-39, 2013.

[130] G. Charvet, M. Foerster, G. Chatalic, A. Michea, J. Porcherot, S. Bonnet*, et al.*, "A wireless 64-channel ECoG recording Electronic for implantable monitoring and BCI applications: WIMAGINE," *Engineering in Medicine and Biology Society (EMBC), 2012 Annual International Conference of the IEEE*, 2012, pp. 783-786.

[131] J. Parramon, P. Doguet, D. Marin, M. Verleyssen, R. Munoz, L. Leija*, et al.*, "ASIC-based batteryless implantable telemetry microsystem for recording purposes," *Conference Proceedings. 19th International Conference on IEEE/EMBS,* vol. 5, pp. 2225-2228, 1997.

[132] N. R. Prabhav, S. R. Devasahayam, and R. Ojha, "Implanted Myo-neural Interface for Upper Limb Prosthesis " *World Congress on Medical Physics and Biomedical Engineering,* vol. 25, pp. 584-587, 2009.

[133] D. M. Russell, D. McCormick, A. J. Taberner, S. C. Malpas, and D. M. Budgett, "A high bandwidth fully implantable mouse telemetry system for chronic ECG measurement," *Engineering in Medicine and Biology Society, EMBC, 2011 Annual International Conference of the IEEE*, 2011, pp. 7666-7669.

[134] I.-T. Hsieh, C. C.-H. Yang, C.-Y. Chen, G.-S. Lee, F.-J. Kao, K.-L. Kuo*, et al.*, "Uninterrupted wireless long-term recording of sleep patterns and autonomic function in freely moving rats," *Journal of Medical and Biological Engineering,* vol. 33, pp. 79-86, 2013.

[135] R. Berry, "The natural history of the house mouse," *Field studies,* vol. 3, pp. 219-262, 1970.

[136] T. Sumerling and S. Quant, "Measurement of the human anterior chest wall by ultrasound and estimates of chest wall thickness for use in determination of transuranic nuclides in the lung," *Radiation Protection Dosimetry,* vol. 3, pp. 203-210, 1982.

[137] R. McLean, M. Richards, C. Crandall, and J. Marinaro, "Ultrasound determinationof chest wall thickness: implications of needle thoracostomy," *American Journal of Emergency Medicine,* vol. 29, pp. 1173-1177, 2011.

[138] M. W. Dewhirst, B. L. Viglianti, M. Lora-Michiels, M. Hanson, and P. J. Hoopes, "Basic principles of thermal dosimetry and thermal thresholds for tissue damage from hyperthermia," *International Journal of Hyperthermia,* vol. 19, pp. 267-294, Jan 2003.

[139] M. C. Ziskin and J. Morrissey, "Thermal thresholds for teratogenicity, reproduction, and development," *International Journal of Hyperthermia,* vol. 27, pp. 374-387, Jun 2011.

[140] G. C. Rhoon, T. Samaras, P. S. Yarmolenko, M. W. Dewhirst, E. Neufeld, and N. Kuster, "CEM43°C thermal dose thresholds: a potential guide for magnetic resonance radiofrequency exposure levels?," *European Radiology,* vol. 23, pp. 2215-2227, 2013.

[141] G. E. Loeb, R. A. Peck, W. H. Moore, and K. Hood, "BION system for distributed neural prosthetic interfaces," *Medical engineering & physics,* vol. 23, pp. 9-18, 2001.

[142] R. F. Weir, P. R. Troyk, G. A. DeMichele, D. A. Kerns, J. F. Schorsch, and H. Maas, "Implantable Myoelectric Sensors (IMESs) for Intramuscular Electromyogram Recording," *Biomedical Engineering, IEEE Transactions on,* vol. 56, pp. 159-171, 2009.

[143] K. Khanafer and K. Vafai, "Synthesis of Mathematical Models Representing Bioheat Transport," *Advances in Numerical Heat Transfer, Vol 3,* vol. 3, pp. 1-28, 2009.

[144] A. Kurs, A. Karalis, R. Moffatt, J. D. Joannopoulos, P. Fisher, and M. Soljačić, "Wireless power transfer via strongly coupled magnetic resonances," *science,* vol. 317, pp. 83-86, 2007.

[145] J. S. Ho, A. J. Yeh, E. Neofytou, S. Kim, Y. Tanabe, B. Patlolla*, et al.*, "Wireless power transfer to deep-tissue microimplants," *Proceedings of the National Academy of Sciences,* May 2014.

[146] B. M. Badr, R. Somogyi-Gsizmazia, N. Dechev, and K. R. Delaney, "Power transfer via magnetic resonant coupling for implantable mice telemetry device," *IEEE Wireless Power Transfer Conference*, 2014, pp. 259-264.

[147] K. Eom, J. Jeong, T. Lee, J. Kim, J. Kim, S. Lee*, et al.*, "A wireless power transmission system for implantable devices in freely moving rodents," *Medical & Biological Engineering & Computing,* vol. 52, pp. 639-651, Aug 2014.

[148] E. G. Kilinc, G. Conus, C. Weber, B. Kawkabani, F. Maloberti, and C. Dehollain, "A System for Wireless Power Transfer of Micro-Systems In-Vivo Implantable in Freely Moving Animals," *IEEE Sensors Journal,* vol. 14, pp. 522-531, 2014.

[149] G. Kamen and D. A. Gabriel, *Essentials of electromyography*. Champaign, IL: Human Kinetics, 2010.

[150] S. Mallya and J. H. Nevin, "Design procedures for a fully differential folded-cascode CMOS operational amplifier," *IEEE Journal of Solid-State Circuits,* vol. 24, pp. 1737-1740, 1989.

[151] M. H. Zarifi, J. Frounchi, S. Farshchi, and J. Judy, "A low-power, low-noise neural-signal amplifier circuit in 90-nm CMOS," *Engineering in Medicine and Biology Society, 2008. EMBS 2008. 30th Annual International Conference of the IEEE*, 2008, pp. 2389-2392.

[152] W. Wattanapanitch, M. Fee, and R. Sarpeshkar, "An Energy-Efficient Micropower Neural Recording Amplifier," *IEEE Transactions on Biomedical Circuits and Systems,* vol. 1, pp. 136-147, 2007.

[153] C. Qian, J. Parramon, and E. Sanchez-Sinencio, "A Micropower Low-Noise Neural Recording Front-End Circuit for Epileptic Seizure Detection," *IEEE Journal of Solid-State Circuits,* vol. 46, pp. 1392-1405, 2011.

[154] B. Gosselin, "Recent advances in neural recording microsystems," *Sensors (Basel),* vol. 11, pp. 4572-97, 2011.

[155] F. Buchthal, C. Guld, and P. Rosenfalck, "Volume Conduction of the Spike of 'the Motor Unit Potential Investigated with a New Type of Multielectrode," *Acta Physiologica Scandinavica,* vol. 38, pp. 331-354, 1957.

[156] N. Dimitrova and G. Dimitrov, "Interpretation of EMG changes with fatigue: facts, pitfalls, and fallacies," *Journal of Electromyography and Kinesiology,* vol. 13, pp. 13-36, 2003.

[157] J. Enrique and T. E. Milner, "The effects of skinfold thickness on the selectivity of surface EMG," *Electroencephalography and Clinical Neurophysiology/Evoked Potentials Section,* vol. 93, pp. 91-99, 1994.

[158] I. Gath and E. Stålberg, "On the measurement of fibre density in human muscles," *Electroencephalography and clinical neurophysiology,* vol. 54, pp. 699-706, 1982.

[159] L. Lindstrom and I. Petersen, "Power spectrum analysis of EMG signals and its applications," *Progress in clinical neurophysiology,* vol. 10, pp. 1-51, 1983.

[160] A. P. Chandran, K. Najafi, and K. D. Wise, "A new DC baseline stabilization scheme for neural recording microprobes," *[Engineering in Medicine and Biology, 1999. 21st Annual Conference and the 1999 Annual Fall Meetring of the Biomedical Engineering Society BMES/EMBS Conference, 1999. Proceedings of the First Joint*, 1999, p. 386 vol. 1.

[161] P. Mohseni and K. Najafi, "A low power fully integrated bandpass operational amplifier for biomedical neural recording applications," *Engineering in Medicine and Biology, 2002. 24th Annual Conference and the Annual Fall Meeting of the Biomedical Engineering Society EMBS/BMES Conference, 2002. Proceedings of the Second Joint*, 2002, pp. 2111-2112 vol.3.

[162] K. I. Gawlik and M. Durbeej, "Skeletal muscle laminin and MDC1A: pathogenesis and treatment strategies," *Skeletal muscle,* vol. 1, p. 1, 2011.

[163] C. R. Heier and C. J. DiDonato, "ECG in neonate mice with spinal muscular atrophy allows assessment of drug efficacy," *Front Biosci (Elite Ed),* vol. 7, pp. 107-16, 2015.

[164] Texas Instruments, "INA333 Micro-Power (50µA), Zero-Drfit, Rail-to-Rail Out Instruemntation Amplifier," July 2008 [Revised Dec. 2015].

[165] J. Lee, Y. Lim, H. Ahn, J. Yu, and S. Lim, "Impedance-Matched Wireless Power Transfer Systems Using an Arbitrary Number of Coils With Flexible Coil Positioning," *IEEE Antennas and Wireless Propagation Letters,* vol. 13, pp. 1207-1210, 2014.

[166] J. Lee, Y.-S. Lim, W.-J. Yang, and S.-O. Lim, "Wireless power transfer system adaptive to change in coil separation," *IEEE Transactions on Antennas and Propagation,* vol. 62, pp. 889-897, 2014.

[167] T. Y. Chang, V. G. Yadav, S. De Leo, A. Mohedas, B. Rajalingam, C.-L. Chen*, et al.*, "Cell and Protein Compatibility of Parylene-C Surfaces," *Langmuir,* vol. 23, pp. 11718-11725, Nov 2007.

[168] D. Winter, *EMG interpretation*: Taylor & Francis, London, 1996.

[169] B. L. Patton, B. Wang, Y. S. Tarumi, K. L. Seburn, and R. W. Burgess, "A single point mutation in the LN domain of LAMA2 causes muscular dystrophy and peripheral amyelination," *Journal of Cell Science,* vol. 121, pp. 1593-604, May 15 2008.

[170] J. W. Sensinger, B. A. Lock, and T. A. Kuiken, "Adaptive Pattern Recognition of Myoelectric Signals: Exploration of Conceptual Framework and Practical Algorithms," *IEEE Transactions on Neural Systems and Rehabilitation Engineering,* vol. 17, pp. 270-278, 2009.

[171] E. F. Delagi and A. Perotto, *Anatomic guide for the electromyographer--the limbs*: Charles C. Thomas Publisher, 1980.

[172] D. Ha, T.-C. Lee, D. J. Webery, and W. J. Chappell, "Power distribution to multiple implanted sensor devices using a multiport bandpass filter (BPF) approach," presented at the IEEE MTT-S International Microwave Symposium (IMS), 2014.

[173] B. Hudgins, P. Parker, and R. N. Scott, "A new strategy for multifunction myoelectric control," *Biomedical Engineering, IEEE Transactions on,* vol. 40, pp. 82-94, 1993.

[174] K. Ziegler-Graham, E. J. MacKenzie, P. L. Ephraim, T. G. Travison, and R. Brookmeyer, "Estimating the Prevalence of Limb Loss in the United States: 2005 to 2050," *Archives of Physical Medicine and Rehabilitation,* vol. 89, pp. 422-429, Mar 2008.

[175] W. K. Daly, "Electrodes installed in roll-on suspension sleeves," *Myoelectric Controls/Powered Prosthetics Symposium*, 2002.

[176] L. J. Hargrove, A. J. Young, A. M. Simon, N. P. Fey, R. D. Lipschutz, S. B. Finucane*, et al.*, "Intuitive control of a powered prosthetic leg during ambulation: a randomized clinical trial," *JAMA,* vol. 313, pp. 2244-2252, 2015.

[177] L. J. Hargrove, A. M. Simon, A. J. Young, R. D. Lipschutz, S. B. Finucane, D. G. Smith*, et al.*, "Robotic leg control with EMG decoding in an amputee with nerve transfers," *New England Journal of Medicine,* vol. 369, pp. 1237-1242, 2013.

[178] O. Kannape and H. M. Herr, "Volitional control of ankle plantar flexion in a powered transtibial prosthesis during stair-ambulation," *International Conference of the IEEE Engineering in Medicine and Biology Society*, 2014, pp. 1662-1665.

[179] B. Qing and K. D. Wise, "Single-unit neural recording with active microelectrode arrays," *IEEE Transactions on Biomedical Engineering,* vol. 48, pp. 911-920, 2001.

[180] J. Simpson and M. Ghovanloo, "An Experimental Study of Voltage, Current, and Charge Controlled Stimulation Front-End Circuitry," *Circuits and Systems, 2007. ISCAS 2007. IEEE International Symposium on*, 2007, pp. 325-328.

[181] D. R. Merrill, M. Bikson, and J. G. Jefferys, "Electrical stimulation of excitable tissue: design of efficacious and safe protocols," *J Neurosci Methods,* vol. 141, pp. 171-98, Feb 15 2005.

[182] S. Reardon, "Electroceuticals spark interest," *Nature,* vol. 511, pp. 18-18, 2014.

[183] G. Sinha, "Charged by GSK investment, battery of electroceuticals advance," *Nature medicine,* vol. 19, pp. 654-654, 2013.

[184] K. G. Pearson, H. Acharya, and K. Fouad, "A new electrode configuration for recording electromyographic activity in behaving mice," *J Neurosci Methods,* vol. 148, pp. 36-42, Oct 15 2005.

[185] M. A. Fisher, "AAEM Minimonograph 13: H reflexes and F waves: physiology and clinical indications," *Muscle & nerve,* vol. 15, pp. 1223-1233, 1992.

[186] C. Panayiotopoulos and E. Chroni, "F-waves in clinical neurophysiology: a review, methodological issues and overall value in peripheral neuropathies," *Electroencephalography and Clinical Neurophysiology/Electromyography and Motor Control,* vol. 101, pp. 365-374, 1996.

[187] G. Weber, "Nerve conduction studies and their clinical applications," *Clinics in podiatric medicine and surgery,* vol. 7, pp. 151-178, 1990.

[188] L. P. Tilley and N. Burtnick, *ECG for the Small Animal Practitioner*: Teton NewMedia, 1999.

[189] F. Achilli, V. Bros-Facer, H. P. Williams, G. T. Banks, M. AlQatari, R. Chia*, et al.*, "An ENU-induced mutation in mouse glycyl-tRNA synthetase (GARS) causes peripheral sensory and motor phenotypes creating a model of Charcot-Marie-Tooth type 2D peripheral neuropathy," *Disease Models and Mechanisms,* vol. 2, pp. 359-373, 2009.

[190] K. L. Seburn, L. A. Nangle, G. A. Cox, P. Schimmel, and R. W. Burgess, "An active dominant mutation of glycyl-tRNA synthetase causes neuropathy in a Charcot-Marie-Tooth 2D mouse model," *Neuron,* vol. 51, pp. 715-726, 2006.

[191] K. Toyka, D. Brachman, A. Pestronk, and I. Kao, "Myasthenia gravis: passive transfer from man to mouse," *Science,* vol. 190, pp. 397-399, Oct 1975.

VITA

VITA

EDUCTATION

Ph.D. Purdue University, West Lafayette, IN, Biomedical Engineering. Expected Graduation: May 2016. Thesis Committee: P. P. Irazoqui (advisor), K. L. Seburn, B. S. Duerstock, and E. Culurciello

M.S. Purdue University, West Lafayette, IN, Biomedical Engineering. Graduation: Aug. 2011.Thesis Committee: P. P. Irazoqui (advisor), E. A. Nauman, J. E. Seipel, and T. A. Kuiken

B.S. Purdue University, West Lafayette, IN, Biomedical Engineering. Graduation: May 2010 (GPA: 3.85/4.0)

RESEARCH EXPERIENCE

Research Assistant in the Center for Implantable Devices (CID)
Purdue University, West Lafayette, IN (May. 2011—Present)

- Served as lead graduate student on the neuromuscular interfaces project, which produced a patent and a fully wireless myoelectric sensor array for upper-limb amputees using myoelectric prostheses.
- Designed analog circuits and implemented full system integration and testing of the Bionode, a fully wireless, implantable device for recording and stimulating bioelectric events resulting in a $1M award grant from the international GlaxoSmithKline Bioelectronics R&D Innovation Challenge competition.
- Led the layout of multiple mixed-signal circuit boards utilizing advanced PCB fabrication techniques.
- Integrated implantable device sub-elements from an interdisciplinary team; carried out meticulous testing, debugging, and assessment of implant performance.
- Tailored device and electrode design for longitudinal study of neurodegenerative disorders.
- Created a mammalian tissue model to investigate far-field wireless power transfer in the body.
- Wrote and carried out experimental protocols for acute and chronic animal work to validate device performance *in vivo*.

Charles C. Chappelle Research Fellow in the Center for Implantable Devices (CID)
Purdue University, West Lafayette, IN (May. 2010—May 2011)

- Documented the problem domain of prosthetic limb rejection and global availability.
- Built an electric-powered, four degree-of-freedom upper-limb prosthetic prototype.
- Completed extensive training with electrical lab equipment, machine shop tools, and medical/surgical instrumentation.

Senior Design Student Collaborator with Abbott Point-of-Care
Purdue University, West Lafayette, IN (Aug. 2009—Dec. 2009)

- Coordinated with a team to develop a companion device for Abbott's iSTAT® blood analyzer that isolates plasma from whole blood, resulting in a publication and preliminary patent.
- Maintained meticulous records of experimental procedures, results, and reference literature.
- Reported progress regularly to corporate partners through monthly conference calls.

Summer Undergraduate Research Fellow in the Brain-Computer Interfaces (BCI) Lab
Purdue University, West Lafayette, IN (May 2009—Aug. 2009)

- Made a model cardiovascular system to calibrate stent-mounted sensors.
- Explored a novel method for chronic measurement of blood oxygen saturation (Sp02) by building a miniature stent-mounted pulse oximeter.

TEACHING EXPERIENCE

Graduate Teaching Assistant in BME 301: Bioelectricity
Weldon School of Biomedical Engineering, Purdue University, West Lafayette, IN (Fall 2011, Fall 2012, and Fall 2015)

- Introductory course to neural anatomy, bioelectric signals, and modeling of bioelectric events that integrated hands-on circuit building and algorithm design in Python and numerical methods in MATLAB. Taught by Prof. Pedro Irazoqui and Prof. Eugenio Culurciello. Responsibilities included producing homework assignments and solutions, writing tutorials for working with Python and Raspberry Pi single-board computer (SBC), delivering select lectures, grading, and conducting office hours to aid individuals with assignments or exam preparation.

Graduate Teaching Assistant in BME 489: Senior Design Projects Lab
Weldon School of BME, Purdue University, West Lafayette, IN (Fall 2013 and Fall 2014)

- Capstone course for seniors in BME in which students on small teams quantitatively defined and solved a semester-long design project. Course emphasized practical and hands-on learning, experimental design, and design documentation. Taught by Prof. Pedro Irazoqui. Responsibilities included technical mentorship of individuals and teams, collaborative brainstorming with students, and evaluation of written and oral assignments.

Graduate Teaching Assistant in BME/ECE 528: Measurement and Stimulation of the Nervous System

Weldon School of BME, Purdue University, West Lafayette, IN (Spring 2015)

- Graduate-level course that covered the engineering challenges of recording and triggering bioelectric events while taking a close look at the interface between excitable tissue and electrodes or other hardware in the body. Enrollment was offered for both on-campus and distance learning students. Taught by Prof. Eugenio Culurciello. Responsibilities included regular correspondence with distance learning students, presentation of select lectures, and moderation of class forum for discussion and questions.

Teaching Assistant for nanoHUB-U online offering of Bioelectricity

Weldon School of BME, Purdue Univ., West Lafayette, IN (Spring 2014)

- Online course introducing neural anatomy, bioelectric signals, and modeling of bioelectric events. Taught by Prof. Pedro Irazoqui. Responsibilities included course beta-testing, production of all homework assignments, and delivering filmed recitation sessions detailing homework solutions.

Graduate Teaching Assistant in BME 295: Frontiers in Biomedical Engineering

Weldon School of BME, Purdue Univ., West Lafayette, IN (Fall 2011)

- Seminar course for new BME students aimed at improving written and oral communication skills, awareness of ethical issues, and professional dynamics in the scientific community while introducing cutting-edge areas of research within various branches of biomedical engineering. Responsibilities included course structure, lecture planning and delivery, grading, résumé review, and one-on-one soft skill mentoring to equip students with tools for networking, developing their career paths, and navigating the job search.

Director/Coach of the Purdue University Color Guard and Winter Guard

Purdue University Bands and Orchestras, West Lafayette, IN (Apr. 2010—Present)

- Team comprising 34 undergraduate students that performs with the Purdue Marching Band during the fall semester and competes as an indoor ensemble during the spring semester. Responsibilities include providing daily instruction on elements of technique and performance, along with constructive feedback; preparing written materials for public distribution; production design and choreography; organizing travel logistics; personally mentoring students; and developing team's core philosophy and artistic direction.

Tutor for Student Athletes

Purdue Intercollegiate Athletics, West Lafayette, IN (Jan. 2007—Jan. 2009)

- One-on-one scheduled tutoring sessions to help student athletes with homework or test preparation in engineering, science, and math courses. Responsibilities included preparing teaching materials and explaining technical material at an adaptable pace.

AWARDS, FELLOWSHIPS, AND HONORS

- Estus H. and Vashti L. Magoon Award for Excellence in Teaching in 2015
- Purdue Teaching Academy Graduate Teaching Award in 2015
- Member of nanoHUB-U course development team that received 2014 Excellence in Distance Learning Award
- Third place in 2011 NCIIA BMEStart competition for biomedical innovations
- Charles C. Chappelle Graduate Fellowship in 2010-11
- Received B.S. degree with Academic Distinction (top 10% of graduating class)
- Best Poster Award at the 2009 Summer Undergraduate Research Fellowship (SURF) Symposium
- Member of Tau Beta Pi Engineering Honor Society
- Jenny Helms Award for leadership and academic excellence awarded by Purdue University Bands in 2008

PATENTS AND PUBLICATIONS

- **R. A. Bercich***, S. T. Lee*, D. J. Pederson, Z. Wang, M. Arafat, H. Mei, C. Quinkert, G. Albors, J. Somann, J. Jefferys, P. P. Irazoqui, "Bionode for Fully Wireless Recording and Stimulating of Bioelectric Events in Rodents within a Large Volume Cavity Resonator," IEEE Transactions on Biomedical Engineering. *In review.*
- **R. A. Bercich**, Z. Wang, H. Mei, L. H. Smith, K. L. Seburn, L. H. Hargrove, and P. P. Irazoqui, "Enhancing the Versatility of Wireless Biopotential Acquisition for Myoelectric Prosthetic Control," Journal of Neural Engineering. *In review.*
- H. Mei, K. A. Thackston, **R. A. Bercich**, J. G. R. Jefferys, and P. P. Irazoqui, "Cavity Resonator Wireless Power Transfer System for Freely-Moving Animal Experiments," IEEE Transactions on Biomedical Engineering. *In review*.
- P. Irazoqui, **R. Bercich**, H. S. Bhamra, J. Maeng, C. Meng, O. Gall, Y. Kim, J. Joseph, and W. Chappell. Wirelessly-Powered Implantable EMG Recording System. US Patent Number 13/955,808 filed on July 31, 2013.
- **R. Bercich**, D. Duffy, and P.P. Irazoqui, "Far Field RF Powering of Implantable Devices: Safety Considerations," IEEE Transactions on Biomedical Engineering 2013 doi: 10.1109/TBME.2013.2246787. IEEE Transactions on Biomedical Engineering: 60.8.
- **R. Bercich**, J. Bernhard, K. Larson, and J. Lindsey, "Hand-Held Plasma Isolation Device for Point-of-Care Testing" IEEE Transactions on Biomedical Engineering 2010 doi: 10.1109/TBME.2010.2095419. IEEE Transaction on Biomedical Engineering: 58.3

THESES

- **R. A. Bercich**, "Improving the Mechanistic Study of Neuromuscular Diseases through the Development of a Fully Wireless and Implantable Recording Device," Ph.D. thesis, Department of Biomedical Engineering, Purdue University, West Lafayette, IN, 2016.

- **R. A. Bercich**, "Robotic Arm for Testing and Demonstration of Targeted Muscle Reinnervation with Implications for Low-Cost Upper-Limb Prostheses," M. S. thesis, Department of Biomedical Engineering., Purdue University, West Lafayette, IN, 2011.

PRESENTATIONS AND ABSTRACTS

- D. J. Pederson, **R. A. Bercich**, and P. P. Irazoqui, "Emphasizing Application in Bioelectricity Course." 25th Annual Meeting of the Biomedical Engineering Society, Tampa, FL (October 7—10, 2015).
- K. L. Seburn, **R. A. Bercich**, Z. Wang, D. Pederson, H. Mei, and P. P. Irazoqui, "Miniature Wireless and Batteryless Device for Longitudinal Recording and Stimulating of Bioelectric Events in Small Animals." 45th Annual Meeting of the Society for Neuroscience, Chicago, IL (October 17—21, 2015).
- **R. A. Bercich**, "Improving the Mechanistic Study of Inherited Peripheral Neuropathies through Development of a Wireless Neuromuscular Recording Device." Biomedical Engineering Graduate Student Association Invited Presentation. University of Minnesota, St. Paul, MN. 7 Nov 2014.
- K. L. Seburn, **R. A. Bercich**, and P. P. Irazoqui, "Development of Miniaturized, Wirelessly Powered Neuromuscular Recording Devices for Use in Mice." 9th International Motoneuron Meeting, Halifax, Nova Scotia, Canada (June 15—19, 2014).
- **R. Bercich**, Z. Wang, K.L. Seburn, and P.P. Irazoqui, "Implantable Sensor for Longitudinal Recording of Spontaneous and Voluntary-Evoked EMG and NAP in Untethered Animals." 6th International IEEE/EMBS Conference on Neural Engineering (NER), San Diego, CA (Nov 6—8, 2013).
- **R. A. Bercich**, J. Joseph, O.Z. Gall, J. Maeng, Y.J. Kim, and P.P. Irazoqui, "Implantable Device for Intramuscular Myoelectric Signal Recording." 34th Annual International Conference of the IEEE Engineering in Medicine and Biology Society, San Diego, CA (Aug. 28 –Sep. 1, 2012).
- P. P. Irazoqui, and **R. A. Bercich**, "Myonode: Improving Robustness of Prosthetic Arm Control with an Innovative RF-Based Implantable EMG Recording System." International Workshop on Clinical Brain-Neural Machine Interface Systems. Houston Methodist Research Institute, Houston, TX. 26 Feb 2013.

SERVICE

Guest Speaker for Seniors Exploring Engineering (SEE)
Purdue University, West Lafayette, IN (Oct. 2012)

- Event hosted by the Women in Engineering Program (WIEP) geared toward women in their senior year of high school who were interested in engineering. Responsibilities included delivering a talk and answering participants' questions.

Lab Staff Volunteer for Exciting Discoveries for Girls in Engineering (EDGE) Camp
Purdue University, West Lafayette, IN (Aug. 2011)

- Volunteered at a camp hosted by the Women in Engineering Program (WIEP) that is offered to freshmen and sophomores in high school. Event included hands-on lab sessions where students developed and tested their own hypotheses related to cell culture growth in various mediums. Responsibilities included organizing and running lab sessions and encouraging participants' independent exploration.

PUBLICATIONS

PUBLICATIONS

1. **R. A. Bercich***, S. T. Lee*, D. J. Pederson, Z. Wang, M. Arafat, H. Mei, C. Quinkert, G. Albors, J. Somann, J. Jefferys, P. P. Irazoqui, "Bionode for Fully Wireless Recording and Stimulating of Bioelectric Events in Rodents within a Large Volume Cavity Resonator," IEEE Transactions on Biomedical Engineering. *In review.*
2. **R. A. Bercich**, Z. Wang, H. Mei, L. H. Smith, K. L. Seburn, L. H. Hargrove, and P. P. Irazoqui, "Enhancing the Versatility of Wireless Biopotential Acquisition for Myoelectric Prosthetic Control," Journal of Neural Engineering. *In revision.*
3. H. Mei, K. A. Thackston, **R. A. Bercich**, J. G. R. Jefferys, and P. P. Irazoqui, "Cavity Resonator Wireless Power Transfer System for Freely Moving Animal Experiments," IEEE Transactions on Biomedical Engineering. *In review.*
4. P. Irazoqui, **R. Bercich**, H. S. Bhamra, J. Maeng, C. Meng, O. Gall, Y. Kim, J. Joseph, and W. Chappell. "Wirelessly-Powered Implantable EMG Recording System." US Patent Number 13/955,808 filed on July 31, 2013.
5. **R. Bercich**, D. Duffy, and P.P. Irazoqui, "Far Field RF Powering of Implantable Devices: Safety Considerations," IEEE Transactions on Biomedical Engineering 2013 doi: 10.1109/TBME.2013.2246787. IEEE Transactions on Biomedical Engineering: 60.8.